THE UNIVERSITY OF TOKYO

MASTER THESIS

Development of broadband anti-reflective structures at millimeter wavelengths for a CMB polarization experiment

Author:
Ryota TAKAKU

Supervisor:
Prof. Kazuhisa MITSUDA

January 6, 2020

THE UNIVERSITY OF TOKYO

Abstract

Master thesis

Development of broadband anti-reflective structures at millimeter wavelengths for a CMB polarization experiment

by Ryota TAKAKU

The measurement of the cosmic microwave background (CMB) has advanced our understanding of the universe. The strong scientific motivations in the measurement of CMB polarization is to test the cosmic inflation theory. The CMB has a perfect blackbody radiation while the foreground galactic emission has a different spectral nature from the CMB. A broadband multi-chronic measurement allows us to distinguish the CMB from the foreground emissions.

LiteBIRD, Lite(Light) satellite for the studies of B-mode polarization and Inflation from cosmic background Radiation Detection, is a satelite mission to detect signatures of primordial gravitational waves in the form of primordial B-mode polarization of the CMB. LiteBIRD will cover the frequency band between 34 GHz and 440 GHz in the 3 telescopes (LFT, MFT, and HFT), and LFT is developed by JAXA which will cover the frequency band between 34 GHz and 161 GHz. In order to minimize the systematic uncertainty, we use sapphire-based rotating achromatic half-wave plate (AHWP) to modurate CMB polarization in LFT. It is placed at the top of the optics, whose aperture diameter is 450 mm. A sapphire is particularly attractive in CMB polarization experiments because of a high index of refraction of $n \sim 3$, low-loss at millimeter-wave and a high thermal conductivity at cryogenic temperature. However, the high refractive index results about 50 % of reflectance in one optical element. This is a significant reduction of the throughput in LFT, and we need a broadband anti-reflection (AR) coating on the surface of AHWP.

One can achieve a broadband AR by employing sub-wavelength structures (SWS), also known as moth-eye structures. SWS method is not limited by the availability of the dielectric material since we simply manipulate the material itself. Also, this method is not subjected to a differential thermal shrinkage. Thus, it is more reliable for use at the cryogenic temperature.

In this thesis, we explore the fabrication of SWS using a laser machining and develop the method how to machine SWS which can achieve >90% between 34 and 161 GHz. This is the widest band AR coverage that is achieved at millimeter wavelengths and possibly at any other wavelengths. We optimize the SWS shape to maximize the broadband coverage using Rigorous couple wave analysis (RCWA) method. By adding the parameter of curvature α, we discovered that the shape with $\alpha > 1.0$ named bell shape can cover a broader frequency band than the shape with $\alpha < 1.0$ named Mt.Fuji shape. We developed the fabrication method to realize a bell shape in a practical time with ultra-short pulsed laser ablation. The transmittance measurement was in agreement with the prediction: a transmittance of > 90% was obtained in 40-161 GHz. The fabrication time over a diameter of 34.5 mm was 11.5 h, and we expect that it will take 2.5 months to fabricate on a surface of a 450 mm diameter. It is drastically shorter time than our past estimates which were $\sim$4 years.

Acknowledgements

Acknowledgement: This work is supported by the New Energy and Industrial Technology Development Organization (NEDO) project "Development of advanced laser processing with intelligence based on high-brightness and high efficiency laser technologies", Council for Science, Technology and Innovation(CSTI), Cross-ministerial Strategic Innovation Promotion Program (SIP), JSPS KAKENHI Grant Number JP17H01125, JP15H05441, JP15H05891, JP17K14272, and JSPS Core-to-Core Program, A. Advanced Research Networks.

Contents

List of Figures

List of Tables

Chapter 1

Standard cosmology and beyond

The ancient universe was high temperature and high density state. This theory is called the Big Bang theory. This is supported by cosmic microwave background radiation (CMB) observations. However, the Big Bang theory contains a few unexplainable problems. Today, the observational evidences suggest the existence of the cosmic inflation, which is the exponential expansion of the space before the Big Bang. To probe the cosmic inflation theory, we have to measure the primordial B-mode of CMB precisely. In this chapter, we describe the theory of Standard cosmology and the cosmic inflation theory.

1.1 Standard cosmology

A number of observations give us the knowledge of the universe. We impose the assumptions; the universe is spatially homogeneous and isotropic on large scales, which means that there are no preferred locations and directions in the universe [1]. This is called "cosmological principle", and it is observationally verified beyond $\sim$100 Mpc. And E. Hubble(1889-1953) discovered that the galaxies are moving away from us and also between them each other [10].

By assuming the cosmological principle, the metric of the universe can be written as

$$ds^2 = -c^2dt^2 + a(t)^2\left[\frac{dr^2}{1-Kr^2} + r^2(d\theta^2 + \sin^2\theta d\phi^2)\right] \tag{1.1}$$

where K is the curvature of the universe. The scale factor $a(t)$ explains the time dependency of the space. This metric is called 'Robertson-Walker metric'. Then the expansion rate of the universe in today is written as

$$H_0 = \frac{\dot{a}}{a}|_{t=t_0} = \dot{a}(t_0) \tag{1.2}$$

The subscript 0 means the value in today, and we define $a(t_0) = 1$. By using Eq. 1.1, we can solve the Einstein equation with the cosmological parameter Λ,

$$G_{\mu\nu} + \Lambda\delta_{\mu\nu} = \frac{8\pi G}{c^4}T_{\mu\nu} \tag{1.3}$$

where

$$T_{\mu\nu} = \begin{pmatrix} -\rho & 0 & 0 & 0 \\ 0 & P & 0 & 0 \\ 0 & 0 & P & 0 \\ 0 & 0 & 0 & P \end{pmatrix}. \tag{1.4}$$

In Eq. 1.4, ρ and P is the energy density and pressure of the universe respectively. The Einstein tensor G^{μ}_{ν} is written as

$$G_{\mu\nu} \equiv R_{\mu\nu} - \frac{1}{2} g_{\mu\nu} R, \tag{1.5}$$

where $R_{\mu\nu}$ and R is the ricci tensor and scalar, respectively. They can be solved as

$$R_{00} = -3\frac{\ddot{a}}{a}$$

$$R_{ij} = -\left[\frac{\ddot{a}}{a} + 2\frac{\dot{a}^2}{a^2} + 2\frac{K}{a}\right] g_{ij} \tag{1.6}$$

$$R = -6\left[\frac{\ddot{a}}{a} + \frac{\dot{a}^2}{a^2} + \frac{K}{a}\right]. \tag{1.7}$$

where $g_{\mu\nu}$ is the metric tensor

$$g_{\mu\nu} = \begin{pmatrix} -1 & 0 & 0 & 0 \\ 0 & 1 & 0 & 0 \\ 0 & 0 & 1 & 0 \\ 0 & 0 & 0 & 1 \end{pmatrix}. \tag{1.8}$$

The solution of Eq. 1.3 shows the expansion of the scale factor as a function of the time,

$$\left(\frac{\dot{a}}{a}\right)^2 = \frac{8\pi G}{3c^2}\rho - \frac{c^2 K}{a^2} + \frac{c^2 \Lambda}{3} \tag{1.9}$$

and

$$\frac{\ddot{a}}{a} = \frac{4\pi G}{3c^2}(\rho + 3P) + \frac{c^2 \Lambda}{3}. \tag{1.10}$$

In particular Eq. 1.9 is called Friedmann equation. With eliminating $\ddot{a}$ in Eq. 1.9 and Eq. 1.10, we obtain

$$\dot{\rho} = -(\rho + P)\frac{\dot{a^3}}{a^3}. \tag{1.11}$$

Thus, we can relate the expansion of the scale factor with the matter distribution. In cosmology there are three kinds of important density components: matter, radiation and dark energy. If we introduce $P = w\rho$ where w is the parameter that specifies the equation of state, Eq. 1.11 becomes

$$\frac{\dot{\rho}}{\rho} = -(1 + w)\frac{\dot{(a^3)}}{a^3}. \tag{1.12}$$

The parameter w for matter w_m, radiation w_R, and dark energy w_Λ is given by $w_m = 0$, $w_R = 1/3$, $w_{\Lambda 0}$, then

$$\rho_m \propto a^{-3}$$
$$\rho_R \propto a^{-4} \tag{1.13}$$
$$\rho_\Lambda = const.$$

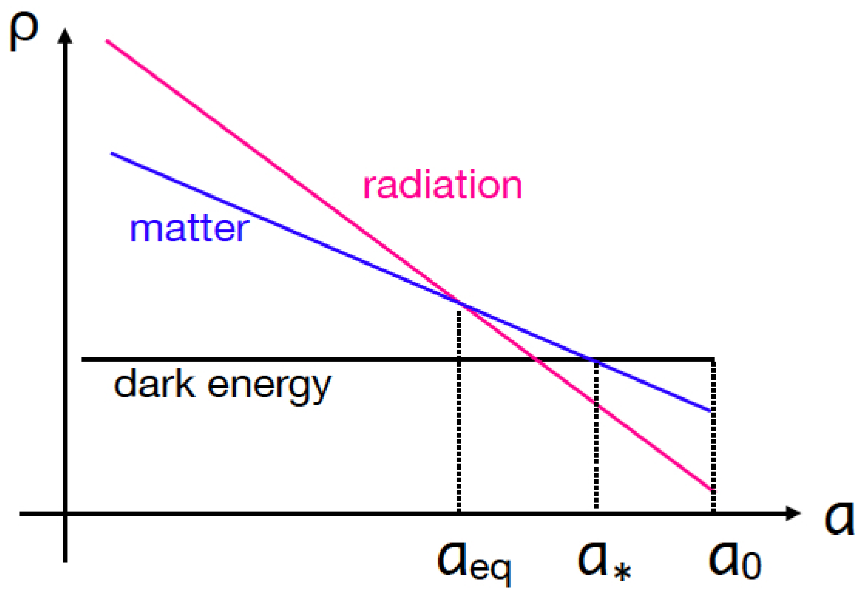

FIGURE 1.1: Evolution of the density components [1]

.

Since the dark energy, matter and radiation evolve as a^0, a^{-3} and a^{-4} respectively, matter or radiation dominates in the early universe depending on the scale factor as shown Fig. 1.1.

We introduce the density parameter Ω as

$$\Omega \equiv \frac{8\pi G\rho}{3c^2H^2} = \frac{\rho}{\rho_c} \tag{1.14}$$

where ρ_c is the critical density given by

$$\rho_c = \frac{3c^2H^2}{8\pi G} \tag{1.15}$$

and its present value is $\rho_{c0} = 1.045h^2 \times 10^4$ eV cm^{-3} [1]. Radiation Ω_R gives a negligible contribution to the energy density of the present universe. Among known particles the baryons have the energy density about 5% of the critical density. The dark matter has a significant density of the universe. Matter (baryons and dark matter) Ω_m accounts for 23% of the present energy density. The present universe is dominated by dark energy Ω_Λ, which amounts to about 67% of the critical density, and thus the universe is almost flat [4].

1.2 Big Bang theory

Our universe is expanding. Then G. Gamow suggested that the ancient universe is high density and high temperature status where particles interacted each other. And the light element is generated as the universe cooled with expansion. This is called "the Big Bang", and it is supported by CMB experiences [3, 11, 4]. CMB was discovered by A. Penzias and R. Wilson in 1964. And the first satelite mission to measure CMB which named COBE (Cosmic Background Explorer) was launched in 1989. COBE measured CMB in full sky, and showed that CMB is perfect black

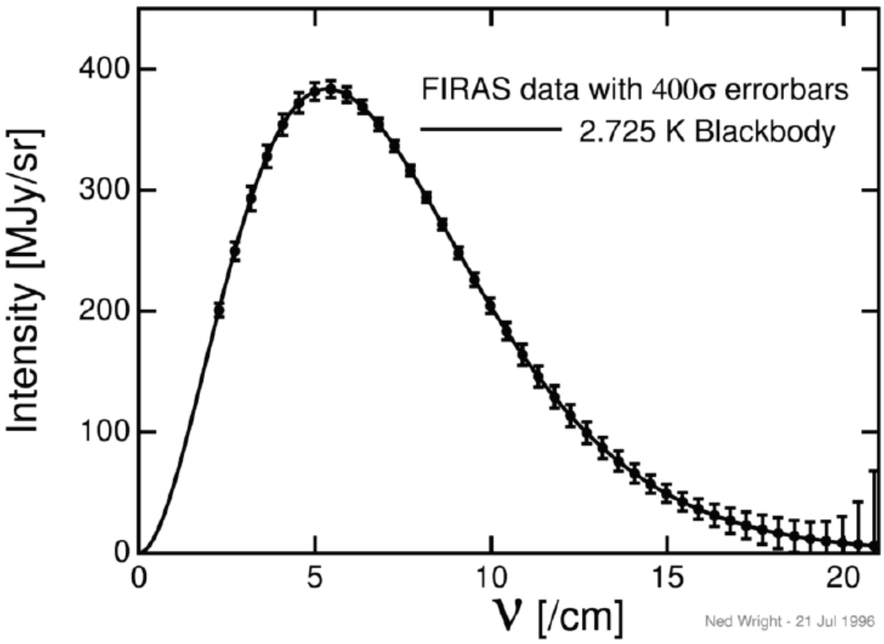

FIGURE 1.2: Black body radiation of CMB measured by COBE FIRAS [2]

body radiation with the temperature of 2.725 K as shown in Fig. 1.2. This is the evidence that the ancient universe was high temperature and high density and CMB interacted with electron each other. Actually there is a little fluctuation in CMB map and it is the key to understand the ancient cosmology status before the Big Bang.

1.3 Problems of Big Bang

Although the Big Bang theory is reliable by CMB observation, there are a few problems which cannot be solved by this theory. Here we introduce two problems of them.

- Horizon problem
  When you look in all directions in the sky, the average appearance is the same, even though the appearance of the galaxy structure is different. CMB is also the same intensity of 2.725 K in any direction. This suggests that at some point in the past, the universe we could see was a causal distance at the speed of light. However, CMB observations show that it is uniform beyond that range. For example, in the Big Bang universe, the causal distance at the time of recombination is 2 degrees in viewing angle.

- Flatness problem
  This is the problem that our universe is almost flat in geometrically. If a universe has higher density than our universe, it has a positive curvature and will eventually contract. On the other hand, if a universe has lower density than our universe it has a negative curvature and any structures will not be formed and will expand forever. CMB observation shows that our universe is extremely flat, and we cannot explain why our universe is such a flat curvature.

- The origin of structures
  Big bang theory cannot explain the origin of the structures. Because the big bang theory assumes that the universe is homogeneous and isotropic. Such a universe cannot form galaxies, galaxy clusters, and large-scale structures.
- Monopole problem
  This problem is that a monopole has not been discovered yet. The particle physicist A. Guth was challenging this problem from the particle physics.

1.4 Inflation theory

The theory to solve these problems is called “cosmic inflation theory”. The cosmic inflation theory is that the space of the ancient universe expanded exponentially. The cosmic nflation theory is suggested by A. Guth and K. Sato in 1981 [12, 13]. They thought that such a exponential expansion dilutes the concentration of the monopole. Since the space expansion speed can be beyond the light speed, it is possible to interact in 2 point where they are out of horizon today. The inflation rapidly stretches out quantum fluctuations in the early small universe. These fluctuations might become the seeds of the temperature fluctuations of CMB and the distribution of Mpc-order large-scale structures in the today’s universe. The curvature of the universe also becomes quite small due to exponential expansion. The model of inflation is that the exponential expansion is caused by the energy of the vacuum that is temporarily generated by a scalar field called "infraton".

1.5 Probe of inflationary universe

To show the cosmic inflation theory, We have to measure "primordial density fluctuation" and "primordial gravitational wave". The primordial density fluctuation is measured by COBE [3], WMAP [11], and Planck [4] well, however we have not observed the primordial gravitational wave yet. Although we do not have such a sensitive detector to detect the gravitational wave, it affects CMB particular polarization pattern called "B-mode". From measurement of CMB polarization, we can evaluate the gravitational wave indirectly. In this section, we describe how to probe the cosmic inflation theory.

1.5.1 Temperature fluctuation

COBE also measured the temperature fluctuation of CMB by DMR (Differential Microwave Radiometer). Fig. 1.3 shows the fluctuation map of CMB temperature in the full sky measured by COBE. In Fig. 1.3, red and blue area is higher and lower temperature than the averaged temperature, and the difference is the order of 10^{-5}. CMB temperature fluctuation affects the ancient matter fluctuation: high density in the lower temperature, and low density in the higher temperature. This is because a light from high density loses the energy as it crawls from the gravitational potential, and light from low density loses less energy than at high density. The temperature fluctuation is measured in more accurate by later satellite projects, WMAP (Wilkinson Microwave Anisotropy Probe) [11] with the resolution of 0.2 degrees and Planck with the resolution of 0.008 degrees [4]. This fluctuation results the formation of galaxies, galaxies clusters, and large-scale structures. In order to analyze the temperature fluctuation of CMB quantitatively, we use “power spectrum” as a statistic

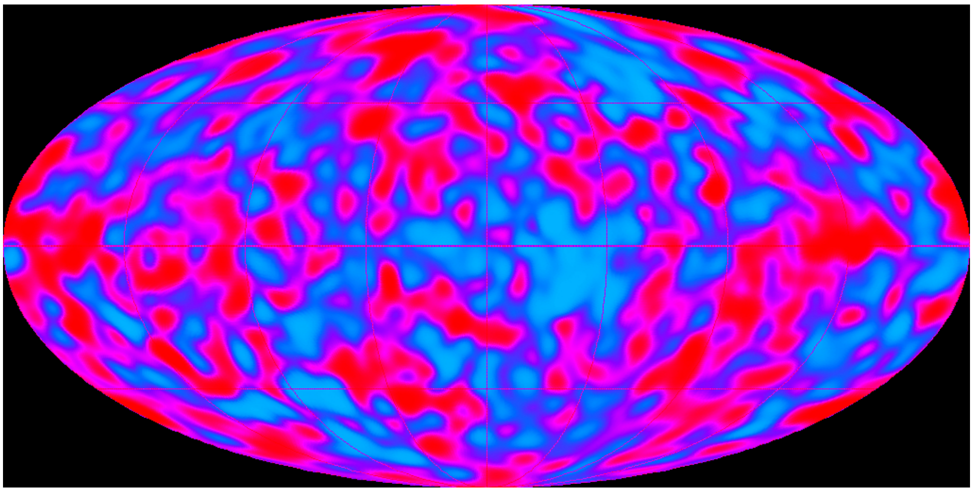

FIGURE 1.3: Full CMB sky masured by COBE [3]

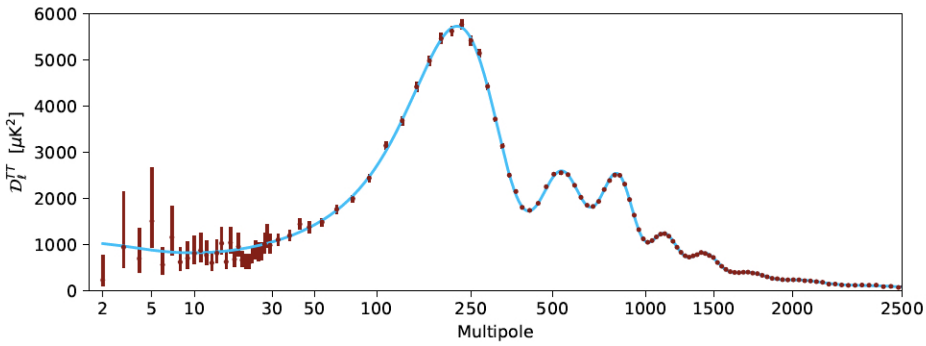

FIGURE 1.4: Planck CMB power spectrum [4]. The vertical axis ($D_\ell = C_\ell \ell(\ell+1)/2\pi\ \mu\mathrm{K}^2) is used conventionally.$

value. The temperature fluctuation is written as $\delta T/T(\theta,\phi)$ with defining the final scattering plane in the angular coordinates (θ, ϕ). Then, we extend the temperature fluctuation by using the spherical harmonics $Y_{\ell m}(\theta,\phi)$,

$$\frac{\delta T}{T}(\theta,\phi) = \sum_{\ell=2}^{\infty} \sum_{m=-\ell}^{\ell} a_{\ell m} Y_{\ell m}(\theta,\phi). \tag{1.16}$$

By using the coefficient $a_{\ell m}$ in Eq. 1.16, we define the power spectrum as

$$C_\ell \equiv \frac{1}{2\ell+1} \sum_{m=-\ell}^{\ell} |a_{\ell m}|^2. \tag{1.17}$$

In Eq. 1.17, the component of $\ell = 0$ is the monopole which means the average temperature of CMB, and $\ell = 1$ is the dipole in which the doppler effect from the movement of the solar system is dominant. Thus, we ignore these components. Fig. 1.4 shows the power spectrum measured by Planck. From the fitting to this data, we can understand the baryon density, the curvature of the universe, and the density parameters. The fitting results are summarized in Tab. 1.1.

TABLE 1.1: Part of the fitted parameters from Planck results [4].

Parameter	Value
H_0	67.36 ± 0.54
Ω_Λ	0.6847 ± 0.0073
Ω_m	0.3153 ± 0.0073
Age[Gyr]	13.797 ± 0.023

1.5.2 CMB polarization

We described the temperature fluctuation of CMB, and we also need the CMB polarization for measuring the primordial gravitational wave indirectly. CMB has the linear polarization due to the thomson scattering with free electron just before the recombination. In order to define this polarization, we use stokes parameter I, Q, U. I is the intensity of the electromagnetic wave, Q and U defines the direction of the polarization. We do not take account into V which defines the circular polarization. The stokes parameters are defined as

$$I = E_x^2 + E_y^2$$
$$Q = E_x^2 - E_y^2 \tag{1.18}$$
$$U = 2E_xE_y \tag{1.19}$$

Fig. 1.5 shows the image of stokes parameter Q and U. We have to note that Q and U depend on the definition of coordinate. For example, if we input $E_x' = \frac{1}{\sqrt{2}}(E_x + E_y)$, $E_y' = \frac{1}{\sqrt{2}}(E_x - E_y)$ into E_x and E_y, Q and U interchange each other. The stokes parameter with the coordinate rotating ϕ becomes

$$\begin{pmatrix} \tilde{Q} \\ \tilde{U} \end{pmatrix} = \begin{pmatrix} \cos 2\phi & \sin 2\phi \\ -\sin 2\phi & \cos 2\phi \end{pmatrix} \begin{pmatrix} Q \\ U \end{pmatrix} \tag{1.20}$$

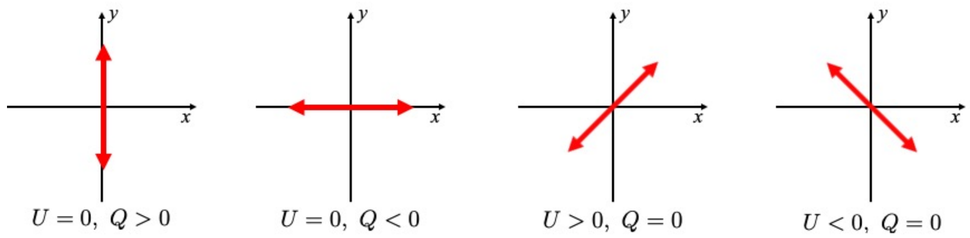

FIGURE 1.5: The image of stokes parameters

Since Q and U depend on the coordinate, we define E-mode and B-mode which do not depend on the coordinate. To define them, we consider the quantity $Q \pm iU$. This satisfies

$$\tilde{Q} \pm i\tilde{U} = \exp(-2\phi)(Q + iU) \tag{1.21}$$

for the coordinate transformation. Since stokes parameter has the spin 2, we can expand $Q \pm iU$ by using spin spherical harmonics $Y_{\ell m}$ to

$$Q \pm iU(\theta, \phi) = \sum_{\ell=2}^{\infty} \sum_{m=-\ell}^{\ell} a_{\ell m} \, Y_{\ell m}(\theta, \phi). \tag{1.22}$$

When we define the coefficient $a_{\ell m} \equiv -(E_{\ell m} \pm B_{\ell m})$, the definition of E-mode and B-mode is written as

$$\begin{aligned} E_{\ell m} &\equiv \frac{-(a_{\ell m} + a_{\ell m})}{2} \\ B_{\ell m} &\equiv \frac{i(a_{\ell m} - a_{\ell m})}{2}. \end{aligned} \tag{1.23}$$

By using Eq. 1.23, Eq. 1.22 becomes

$$Q \pm iU = \sum_{\ell=2}^{\infty} \sum_{m=-\ell}^{\ell} (E_{\ell m} \pm iB_{\ell m}) Y_{\ell m}(\theta, \phi) \tag{1.24}$$

and we can calculate the power spectrum of polarization as

$$\begin{aligned} C_\ell^{EE} &= \frac{1}{2\ell+1} \sum_{m=-\ell}^{\ell} |E_{\ell m}|^2 \\ C_\ell^{BB} &= \frac{1}{2\ell+1} \sum_{m=-\ell}^{\ell} |B_{\ell m}|^2. \end{aligned} \tag{1.25}$$

When we calculate the power spectrum of the temperature fluctuation, we have only one result which is measured around the earth. If we have another result which is measured in different place with us, the power spectrum should be different with us. However, these results should be equal statistically if we assume the cosmological principle because the universe is spatially homogeneous and isotropic in the cosmological principle. Then we consider the ensemble average $\langle C_\ell \rangle$ as a statistic expected value. This means that the power spectrum which we can measure is one of those distributed according to a certain probability distribution around the ensemble average. Thus, in the data analysis, we will infer the ensemble averaged curve which agrees with the measured power spectrum.

When we consider the relationship between cosmic inflation and CMB polarization, it is important that the temperature fluctuation from the primordial density fluctuation only generates E-mode, while one from the primordial gravitational wave generates both E-mode and B-mode. And we have to note that all polarization sources except the promordial density fluctuation produce almost equal amounts of both E-mode and B-mode on the full sky. Thus, we call the E-mode and B-mode from the primordial gravitational wave "primordial E-mode" and "primordial B-mode" as a distinction. CMB polarization is generated at the quadrupole in the last scattering plane. Fig. 1.6 shows the image how to generate the CMB polarization. Red and Blue arrows show the orthogonal components along the traveling directions, and the length of arrow shows the intensity of a light. Since the polarization is not generated at the observer's direction in the Thomson scattering, the direction of polarization from an observer is parallel to x axis. The primordial density fluctuation only generates a polarization perpendicular or parallel along the direction of a fluctuation. While the primordial gravitational wave generates + mode and $\times$ mode due to the space oscillation. Thus, the primordial gravitational wave generates the polarization which rotates 45 degrees from the direction of a fluctuation. Fig. 1.7 shows the image of each polarization.

Planck also observed the polarization of CMB and measured E-mode from the primordial density fluctuation precisely. However, Planck could not measure the primordial E-mode because its intensity is much lower than one from the primordial density fluctuation. The intensity of primordial B-mode is also so small that Planck could not detect it. Now, the measurement of B-mode from the primordial gravitational wave precisely is the key study to understand the cosmic inflation theory.

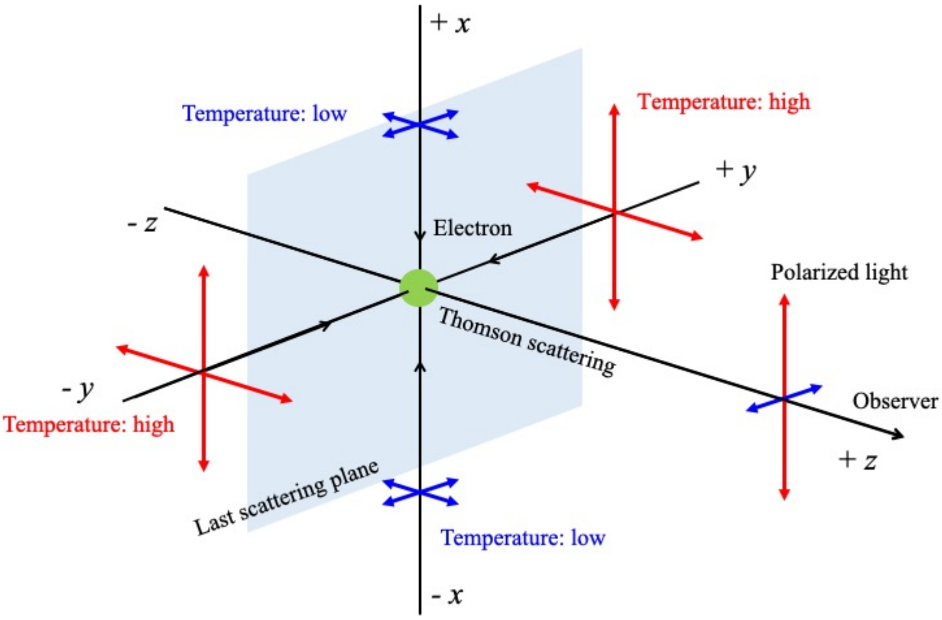

FIGURE 1.6: The principle of generating the CMB polarization. [5]

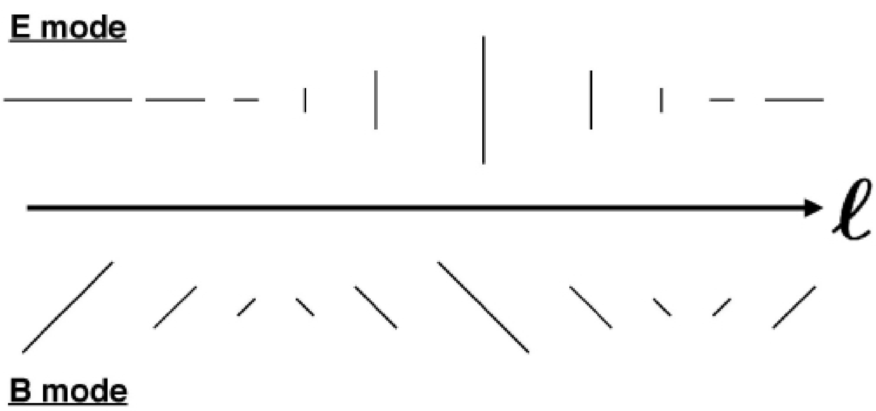

FIGURE 1.7: The image of the difference between E-mode and B-mode [5]

1.5.3 Tensor-to-scalar ratio

We introduce the important parameter in CMB polarization observation, tensor-to-scalar ratio r. Tensor-to-scalar ratio is the ratio between the amplitude of the scalar perturbation (primordial fluctuation) and the amplitude of the tensor perturbation (primordial gravitational wave) which is written as

$$r = \frac{A_{tensor}}{A_{scalar}}. \tag{1.26}$$

The amplitude of the primordial B-mode relates with A_{tensor}. By assuming the representative cosmic inflation model, the energy scale V in the cosmic inflation is written as

$$V^{1/4} \sim {\frac{r}{0.01}}^{1/4} \times 10^{16}\ \mathrm{GeV} \tag{1.27}$$

Since the intensity of primordial density fluctuation is measured well by CMB temperature fluctuation and CMB E-mode polarization, we can evaluate the cosmic inflation model by measuring the primordial B-mode. The limit of r is given as $r < 0.07$ from past observations [4], and as $r > 0.002$ from the representative inflation model.

Chapter 2

CMB experiment

There are many projects to measure CMB polarization all over the world. LiteBIRD, Lite(Light) satellite for the studies of B-mode polarization and Inflation from cosmic background Radiation Detection, is one of the satelite mission to detect primordial B-mode precisely to evaluate the cosmic inflation theory. LiteBIRD will be launched in late 2020s, and observe the CMB polarization in full sky in three years at L2 Lissajous orbit. LiteBIRD is selected as the strategic L-class mission by JAXA in 2019 May. This project is the only satellite to measure the CMB B-mode in 2020s, and thus it is one of the hot project in CMB experiments. In this chapter, we describe the overview of LiteBIRD and explain a part of the instruments related with our development.

2.1 Overview of LiteBIRD

LiteBIRD aims to detect the primordial B-mode for the test of the cosmic inflation. The image of LiteBIRD is shown as Fig. 2.1. The sience goal of LiteBIRD is to meausre the tensor-scalar ratio r with the accuracy of $\delta r < 0.001$ to narrow down the possible model of inflation [14].

LiteBIRD will measure CMB polarization between 34 and 448 GHz by 15 frequency bands in order to distinguish between CMB itself and foregrounds [15]. We will cover this frequency range by Low, Mid and High frequency telescopes (LFT, MHFT) and the coverage of these telescopes is summarized in Tab. 2.1 [6].

LFT is developed by JAXA, and MHFT are developed by Europe. In LFT, We use the crossed dragon telescope to minimize the effects from a multi-refection among refractive surfaces. We are planning to place a polarization modulator unit (PMU) at the top of LFT in order to reduce the systematic uncertainty [8].

We divide the requirement by statistical uncertainty, systematic uncertainty, and a margin. We reduce them $\delta r = 5.7 \times 10^{-4}$ [16].

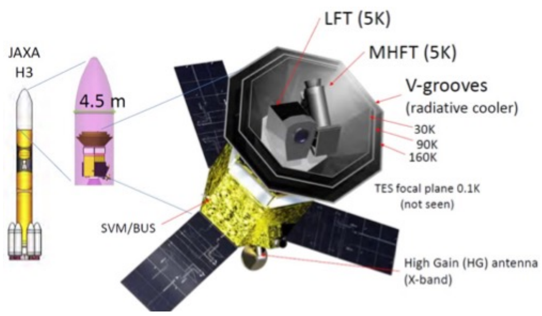

FIGURE 2.1: The image of LiteBIRD [6]

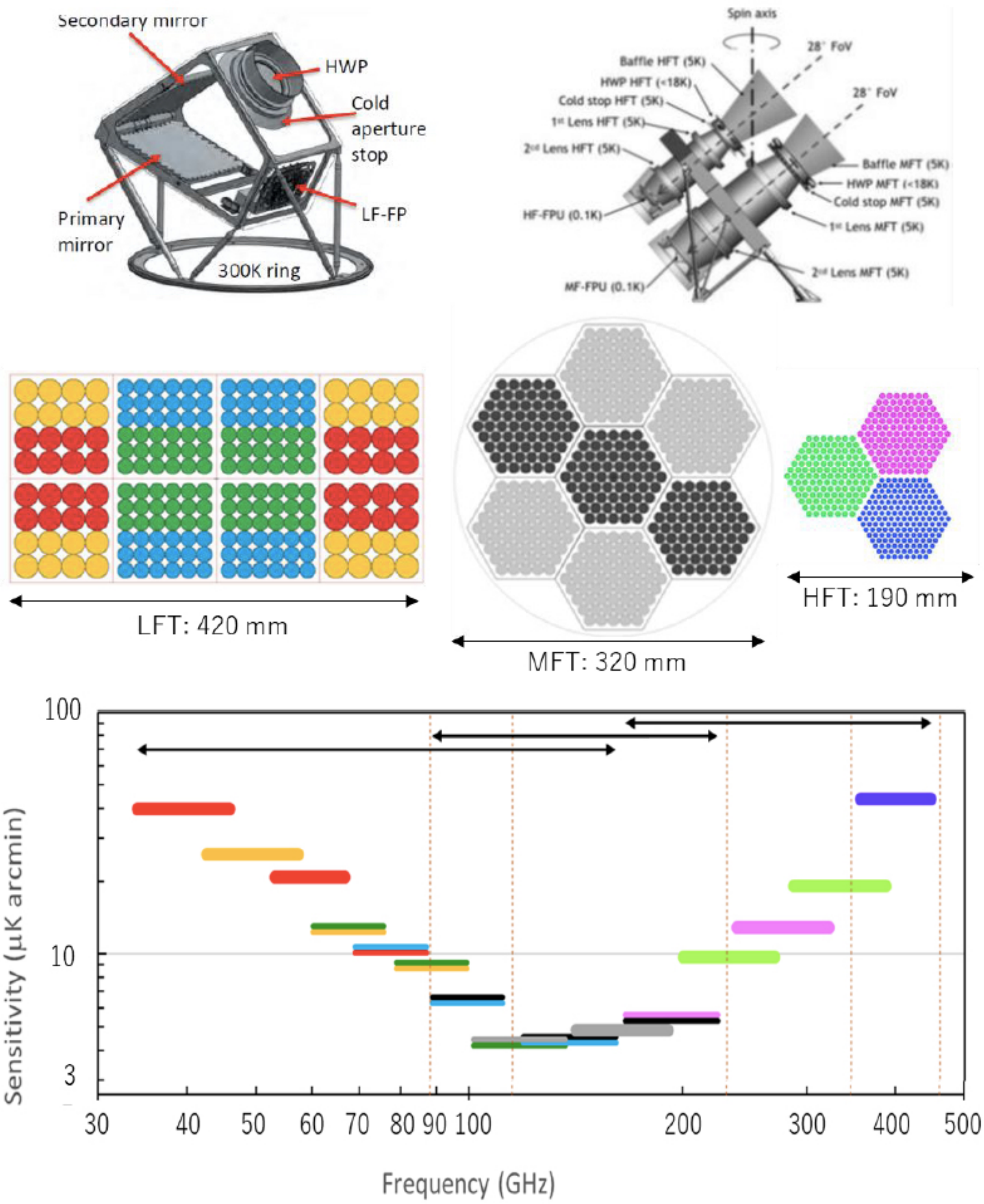

FIGURE 2.2: Top panel shows the designs of LFT (left) and MHFT (right). Middle panel shows the pixel distribution at focal plane in LFT (left), MFT (center), and HFT (right). The pixel diameter and center frequency for each color is following: red (23.6 mm, 40, 60, 78 GHz), orange (15.6 mm, 50, 68, 89 GHz), green (15.6 mm, 68, 89, 119 GHz), and light blue (15.6 mm, 78, 100, 140 GHz) in LFT, black (11.6 mm, 100, 140, 195 GHz) and light gray (11.6 mm, 119, 166 GHz) in MFT, and pink (6.6 mm, 195, 280 GHz), light green (6.6 mm, 235, 337 GHz), and blue (5.7 mm, 402 GHz) in HFT [6].

TABLE 2.1: LiteBIRD bandwidth in LFT, MFT and HFT.

Band [GHz]	Fraction	Initial frequency [GHz]	Ending frequency [GHz]
LFT			
40	0.30	34	46
50	0.30	43	58
60	0.30	53	67
68	0.30	60	76
78	0.30	69	87
89	0.30	79	99
100	0.30	89	112
119	0.30	101	137
140	0.30	119	161
MFT			
100	0.30	89	112
119	0.30	101	137
140	0.30	119	161
166	0.30	141	191
195	0.30	166	224
HFT			
195	0.30	166	224
235	0.30	200	270
280	0.30	228	322
338	0.30	287	389
402	0.23	356	448

2.2 The optical design of LFT

Fig. 2.3 shows the optical design [7]. This type of telescope is named a crossed Dragone (CD) telescope. CD telescope consists of two mirrors of an offset paraboloid and an offset hyperboloid [17]. The advantages of CD telescope are to obtain a wide field of view (FoV), the telecentricity over a large focal plane area, and the compactness in size [17]. The design optimization is developed by S. Kashima and H. Imada [17, 7]. LFT consists of HWP, an Aperture stop, a primary and a secondary mirror, 20 K spillover, 2 K filter, a lenslet, and a detector. We are planning to put the polarization modulator unit based on a continuous rotating half-wave plate (HWP) [8].

2.3 Polarization modulator unit

A polarization modulator unit (PMU) is the important instrument for minimizing the systematic uncertainty. It consists of rotation mechanism and multi-layer AHWP. Fig. 2.4 shows the image of the PMU [8]. We employ a bearing using the superconducting magnetic bearing (SMB) in order to minimize the heat dissipation from the friction by contact-less bearing. We achieve the fully contact free rotation by employing the synchronous motor to drive the rotor. The rotation frequency is about 1 Hz in order to avoid the $1/f$ noise. We monitor the angular position of the HWP by optical encoder in order to remodulate the signal.

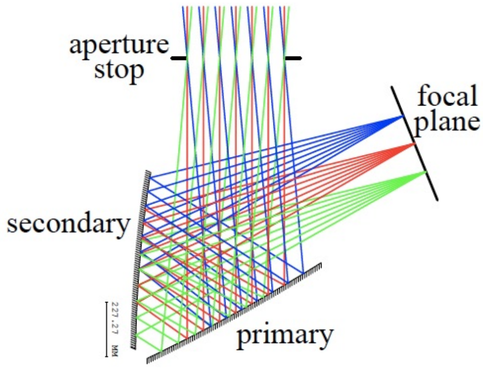

FIGURE 2.3: the optical design and its properties as a function of the incident direction [7]

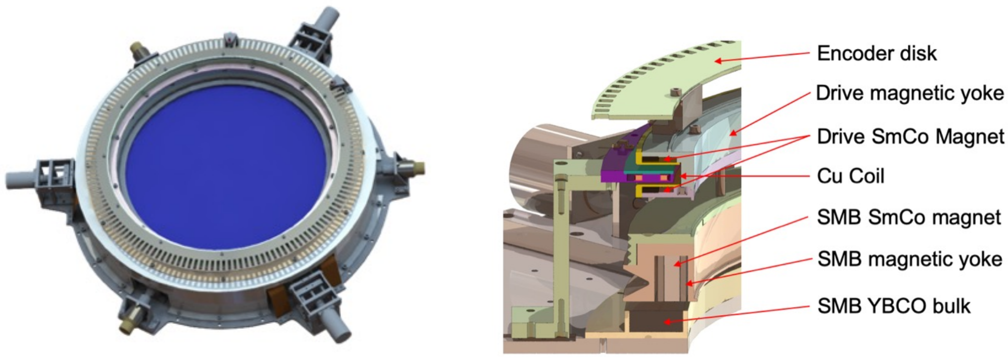

FIGURE 2.4: The CAD drawing of the PMU system [8].

2.3.1 The principle of HWP

It needs a birefringent material to become a HWP. Birefringence is the optical property of anisotropy in the different incident polarization angle. The retardance of waveplate is written as

$$\begin{aligned} \delta &= 2\pi\frac{\Delta n d}{\lambda} \\ \Delta n &= |n_o - n_e| \end{aligned} \tag{2.1}$$

where n_o and n_e is the refractive index of the ordinary and extraordinary ray respectively, and d is the thickness of the waveplate. We use the single HWP for the specific frequency by adjusting the thickness in order to be $\delta = \pi$. If the incident polarization angle has the angle from the optic axis θ, the transmitted signal has the angle of $-\theta$. Thus, the difference between incident and transmitted polarization angle is 2θ.

2.3.2 Rotational half-wave plate

The value of 2θ is important for the modulation of CMB in case of the rotating HWP. Fig. 2.5 shows the process of the modulation by continuous rotating HWP from 0 degrees to 90 degrees. The incident polarization angle is fixed and on the upper raw in the table. The second raw shows the image of rotational HWP. The bold line shows the optic axis of HWP. If there is the difference between the incident

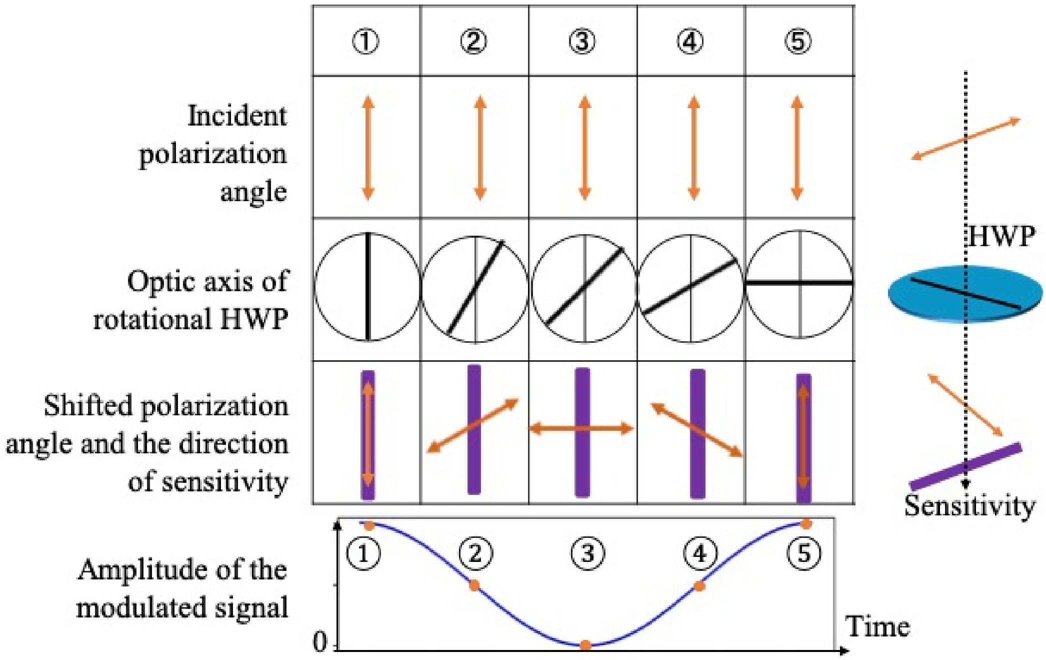

FIGURE 2.5: The process of the modulation by rotating HWP. The top row shows the incident polarization angle, and second row shows the optic axis of rotational HWP. Bold line in the HWP shows the optic axis of the HWP, and the thin line shows the incident polarization angle as a reference. The purple line in the third raw shows the direction of sensitivity. The bottom panel shows the amplitude of the modulated signal.

polarization axis and the optic axis, the transmitted signal has the angle as twice as the incident polarization angle. If we rotate the HWP from 0 degrees to 90 degrees, the modulated signal has oscillated in 360 degrees. The frequency of the modulated signal depends on the rotation speed of the HWP ω. Thus, the frequency of the modulated signal becomes 4ω. This has 2 advantages. One is to detect the signal at the frequency with low effect of $1/f$ noise because the modulated signal has a frequency above the $1/f$ knee frequency. The other is that we can reduce the type of sensitivity from two orthogonal direction to the one direction. This enable us to reduce the systematic errors [18].

2.3.3 The strategy of modulation in broadband frequency for LFT

We cover the frequency between 34 and 161 GHz in LFT, however the single AHWP cannot cover such a broadband. Therefore we apply multi-layer achromatic HWP (AHWP) with stacking specific relative optic angles [19, 20, 21, 22, 23]. We use the multi-layer AHWP at a temperature of 20 K in order to reduce the thermal emission. Then we select the material of HWP as an A-cut sapphire. An A-cut sapphire has high refractive index of $n_o = 3.047$, $n_e = 3.361$ [24] at cryogenic temperature and thus achieving a thin thickness for a less curved lens, low loss $\tan\delta \sim 5 \times 10^{-5}$ at cryogenic temperature[25], and high thermal conductivity of 20 kW/mK (22K) [26]. Thus, we select an A-cut sapphire for a material of HWP.

2.4 Transmittance for LFT sensitivity

Although an A-cut sapphire is a useful optical element for millimeter wave experiments, it has high reflectance due to high refractive index of ~ 3.4. Without any anti-reflectiion (AR) coating, the averaged transmittance is 50%, thus it affects the sensitivity directly as shown in Fig. 2.6 [27]. The left panel in Fig. 2.6 also shows the result when the sensitivity calculation without reflectance is divided by the sensitivity at other numbers of reflectance. From right panel of Fig. 2.6, the sensitivity without any AR coating is 2 times lower than the sensitivity with transmittance of 100%. Fig. 2.7 shows the sensitivity calculation as a function of transmittance of HWP for each frequency band. The dashed line in Fig. 2.7 shows the sensitivity which comes from Sugai et al. [6]. This is the tentative goal sensitivity to achieve the requirement of LiteBIRD. From Fig. 2.7, we should develop the broadband anti-reflection (AR) coating at least > 90% transmittance for the sensitivity improvement.

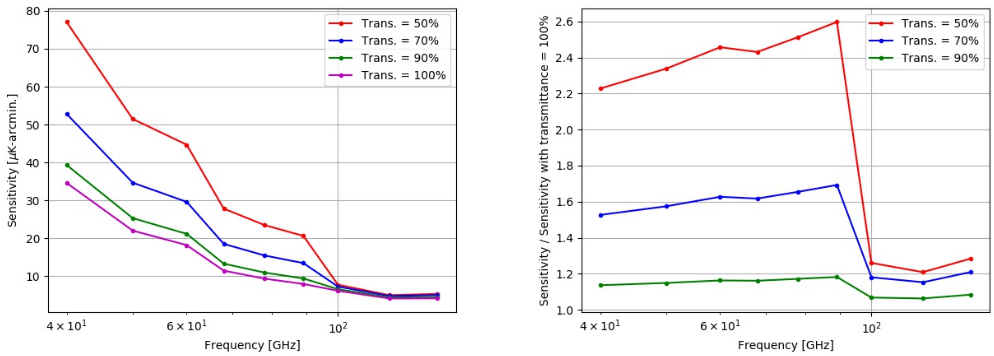

FIGURE 2.6: Left panel shows the sensitivity calculation with different reflectance. Right panel shows the ratio between the sensitivity without reflection and with transmittance of 0.5, 0.7, and 0.9.

2.5 Broadband anti-reflective structures

We can achieve the broadband modulation efficiency by stacking the HWP with specific relative optic axis. Since there is 50% reflection on the multi-layer HWP, we need to broadband anti-reflection (AR) coating on both sides of HWP. We have two directions to achieve broadband AR; multi-layer coatings and the stepped or tapered subwavelength structures (SWS). In both cases, the index of the refraction is gradually shifted from one side of the medium to the other at the boundary. It is not practical that we gather the a number of materials in order to achieve > 90% transmittance with low loss tangent and same shrinkage with an A-cut sapphire. Therefore, we explore the latter method, SWS, also known as moth-eye structures. This idea comes from the biomimetics. A moth has a multi-eye, and its surface consists of small pyramidal structures as shown in Fig. 2.8 [9]. It helps to gather a light in the dark and to hide from predators. Since they can reduce the reflection much, it is applied in not only industry [28] but also other studies between a radio wave and THz bandwidth [29, 30]. As contrast to the multi-layer coating method, the SWS based AR method is not limited by the availability of the dielectric material since we simply manipulate the material itself. This method is not also subjected to a differential thermal shrinkage. Thus, it is more reliable for use at the cryogenic temperature.

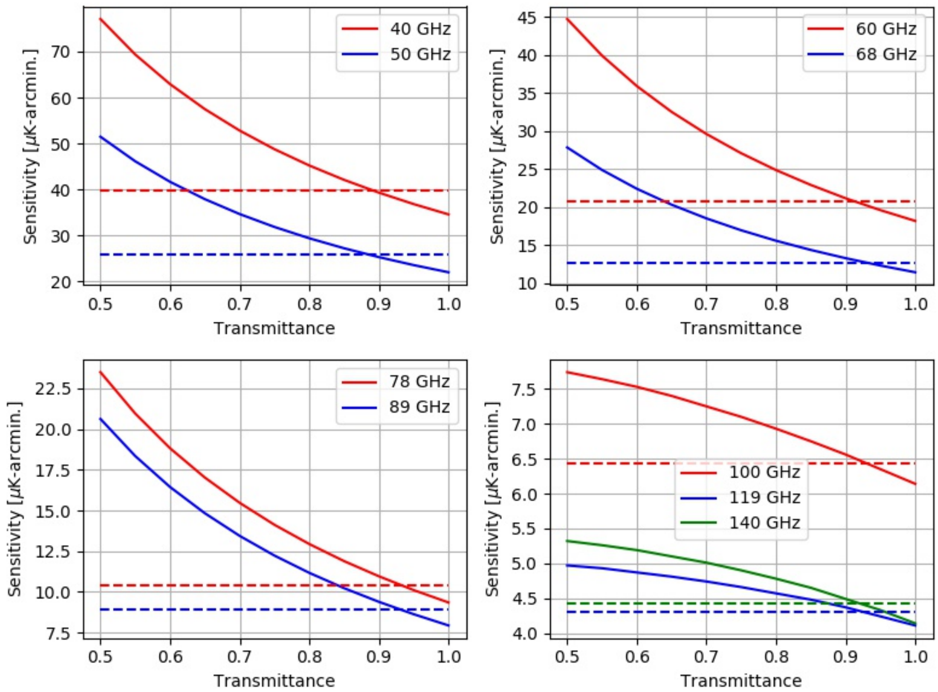

FIGURE 2.7: Sensitivity calculation as a function of transmittance of HWP for each frequency band. We divide 9 frequency bands by 4 subplots. Dashed line shows the sensitivity comes from Sugai et al. [6]

There are a variety of methods to make this SWS, including dicing, etching, and laser machining. There are pros and cons in its choice of the machining method. The working example using a dicing is demonstrated by Datta et al. [31]. This method is optimal for a limited bandwidth due to the advantage of making a step structure. On the other hand, there is a limitation in the depth and the availability of the blade thickness. The etching has an advantage particularly for a silicon. There is an example of using this method for Infrared filter [32]. This method has less degree of freedom to control its shape when the targeted SWS has a complex structural shape. In this thesis, we address the fabrication of SWS using a laser machining. This method has been explored by the past studies and there is a working proof to be explored further [33, 34, 35].

2.6 Purpose of this thesis

The cosmic inflation theory can solve the problems in the Big Bang theory. To evaluate the inflation theory, it is important to measure the CMB primordial B-mode precisely. LiteBIRD aims to achieve the tensor-to-scalar ratio with accuracy of $\delta < 0.001$ to narrow down the possible model of inflation. Since we need the high sensitivity for this science goal, we use rotating AHWP to reduce the systematic uncertainty in LFT. We are developing sapphire multi-layer AHWP to cover broadband frequency and it also needs us to develop the broadband anti-reflective structures to cover between 34 and 161 GHz. Since this is a challenging topics, we aim to achieve above 90% transmittance between 34 and 161 GHz as a first step. The specific numerical goals may change as we are currently studying to determine specifications.

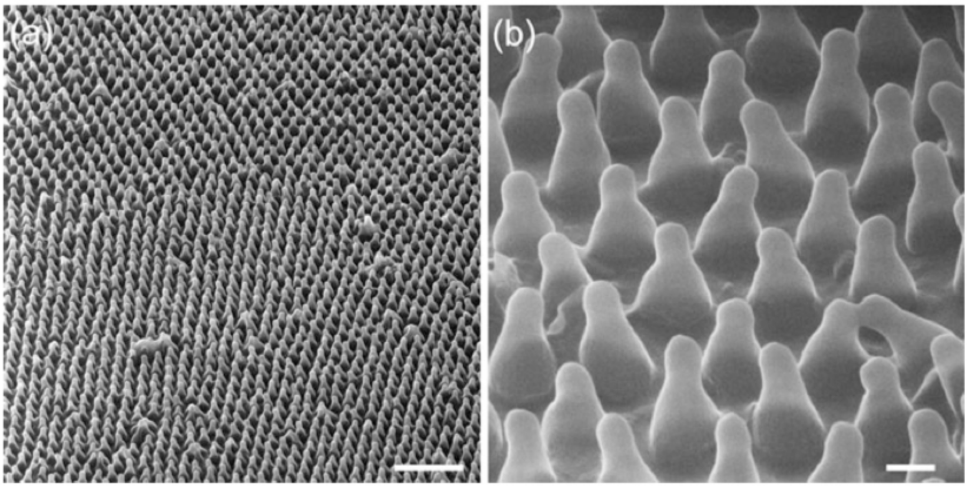

FIGURE 2.8: Scanning helium ion microscope images of natural moth-eye structures found on the transparent wing of the Cephonodes hylas (scale bars: (a) 1 mm, (b) 100 nm) [9]

We developed this study by following steps: We designed the optimal shape by regorous couple wave analysis(RCWA) based calculation described in chapter 3. We developed the method to fabricate the structures according to the simulation by laser ablation in small area for a demonstration. We described the fabrication method and fabricated sample in chapter 4. After we confirmed the optical performance described in chapter 5, we can extend that to cover over a large area. We also showed the discussions about the optical performance in chapter 6.

Chapter 3

Design of SWS

In this chapter, we explain the optimization of the geometrical parameter of SWS by the simulation. Our goal is to achieve over 90% transmittance between 34 and 161 GHz for the LFT in LiteBIRD. First, we explain the rough approximation of the transmittance named effective medium theory (EMT). Since EMT gives the effective refractive index of the periodic structures, we can treat the transmittance by multi-layer coating including the effective refractive index of SWS. Then we apply the rigorous coupled wave analysis (RCWA) method for more accurate calculation than EMT. We also show the Klopfenstein index profile which describes the optimal taper of the index along the depth with the selective bandwidth.

3.1 Multi-layer coating

A multi-layer coating approximation for the SWS is described as below. Transmittance and reflectance is calculated by Maxwell's equation. Fig. 3.1 shows the image of multi-layer coating and the definition of the parameters. The incident vector is defined to be parallel to xz-plane. There are two types of polarization, p-polarization and s-polarization. In the case of p-polarization, the electric field is parallel to the incident plane, while s-polarization is perpendicular to the incident plane. The angle of refraction at i-th layer is calculated by Snell's. law,

$$n_i \sin\theta_i = n_{i+1} \sin\theta_{i+1}, \tag{3.1}$$

where n_i is the refractive index of i-th layer and θ is the incident angle. For the transmittance and reflectance calculation, we use the transpose matrix as following equation

$$M_i = \begin{pmatrix} \cos k_{iz}d_i & \pm\frac{i}{\Gamma_i}\sin k_{iz}d_i \\ \pm i\Gamma_i \sin k_{iz}d_i & \cos k_{iz}d_i \end{pmatrix}, \tag{3.2}$$

where

$$\Gamma_i(\mathrm{p-polarization}) = \frac{n_i}{\cos\theta_i}\sqrt{\frac{\epsilon_0}{\mu_0}} \tag{3.3}$$

$$\tag{3.4}$$

$$\Gamma_i(\mathrm{s-polarization}) = n_i\cos\theta_i\sqrt{\frac{\epsilon_0}{\mu_0}}. \tag{3.5}$$

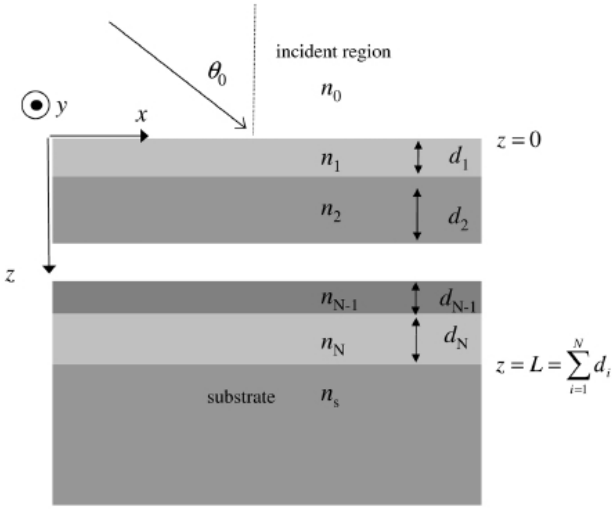

FIGURE 3.1: the image of the multi layer coating and the definition of the parameters.

In Eq. 3.5, k_i and d_i is the wave number and the thickness at i th layer respectively. Then, the total transpose matrix is written as

$$M = M_0 M_1 M_2 \cdots M_N = \prod_{i=0}^{N} M_i. \tag{3.6}$$

This equation leads to the transmittance and reflectance equations,

$$R_P = \left| \frac{-\Gamma_0 M_{11} - \Gamma_0 \Gamma_s M_{12} + M_{21} + \Gamma_s M_{22}}{\Gamma_0 M_{11} + \Gamma_0 \Gamma_s M_{12} + M_{21} + \Gamma_s M_{22}} \right|^2 \tag{3.7}$$

$$T_P = \left| \frac{2\Gamma_s}{\Gamma_0 M_{11} + \Gamma_0 \Gamma_s M_{12} + M_{21} + \Gamma_s M_{22}} \right|^2 \frac{n_0 \cos\theta_s}{n_s \cos\theta_0} \tag{3.8}$$

$$\tag{3.9}$$

for p-polarization with Γ of Eq. 3.5, and

$$R_S = \left| \frac{\Gamma_0 M_{11} - \Gamma_0 \Gamma_s M_{12} + M_{21} - \Gamma_s M_{22}}{\Gamma_0 M_{11} - \Gamma_0 \Gamma_s M_{12} - M_{21} + \Gamma_s M_{22}} \right|^2 \tag{3.10}$$

$$T_S = \left| \frac{2\Gamma_0}{\Gamma_0 M_{11} - \Gamma_0 \Gamma_s M_{12} - M_{21} + \Gamma_s M_{22}} \right|^2 \frac{n_s \cos\theta_0}{n_0 \cos\theta_s} \tag{3.11}$$

for s-polarization with Γ of Eq. 3.4. The subscript 's' means the parameter of the substrate. The detail derivation is written in the Appendix. Eq. 3.8-3.11 give the transmittance and reflectance for the material with tapered refractive index such as SWS.

3.2 Klopfenstein index profile

In this section, we introduce the optimal index taper as a reference. Klopfenstein [36] describes the theory of the impedance profile which can reduce the reflectance in the selective frequency band. This can be converted from impedance to refractive index.

Therefore, we can estimate the optimal index profile which can cover LiteBIRD LFT band between 34 and 161 GHz.

The Klopfenstein index profile is given as

$$\begin{aligned}\ln(n(z)) &= \frac{1}{2}\ln(n_0 n_{sub}) + \frac{\rho_0}{\cosh(A)}\left\{A^2\phi(2z/h, A) + U\left(x - \frac{h}{2}\right) + U\left(z + \frac{h}{2}\right)\right\}\\ &= \ln(n_{sub}), \quad z > h/2,\\ &= \ln(n_0), \quad z < -h/2,\end{aligned} \tag{3.12}$$

where U is the Heviside step function:

$$\begin{aligned}U(z) &\equiv 0, \quad z < 0,\\ U(z) &\equiv 1, \quad z \geq 0.\end{aligned} \tag{3.13}$$

In Eq. 3.12, ϕ is

$$\phi(z, A) = -\phi(-z, A) = \int_0^z \frac{I_1(A\sqrt{1-y^2})}{A\sqrt{1-y^2}}dy, \tag{3.14}$$

where I_1 is the first order of the first kind of modified Bessel function, and h is the height of the structure. The initial value of the reflection coefficient ρ_0 is

$$\rho_0 = \frac{1}{2}\ln(n_s/n_0). \tag{3.15}$$

The parameter A determines the maximum magnitude of reflection coefficient in the selective band which consists of all frequencies such that $2\pi/\lambda h \geq A$. Fig. 3.2 shows the index profile which shows a relation between the refractive index and the height of total layers with a parameter A of 2.45, 3.45, and 4.45. From top panel of Fig. 3.2, we can calculate the transmittance which is based on multi-layer coating. Basically when A increases, the amplitude of transmittance becomes higher with narrower bandwidth. Therefore, A = 3.45 is the middle parameter of the amplitude with wider coverage.

3.3 Bräuer's effective medium theory

Bräuer et al.[37] proposed the fundamental approximation of the effective refractive index for the 2-dimensional grating structure by using the method named effective medium theory (EMT). We can assume a part of the structures the uniform material with tapered refractive index as a function of the depth. Therefore, we can calculate the approximate optical performance by using Eq. 3.8-3.11. Here we introduce the brief explanation about 0th ordered EMT and extend it to the 2nd ordered EMT.

The image of 2-dimensional grating structures is illustrated in Fig. 3.3. Note that these gratings are symmetric structures in x and y directions. By using the geometrical parameters such as the width of structures w and pitch of gratings p, we define the relative layer thickness as

$$f = w/p. \tag{3.16}$$

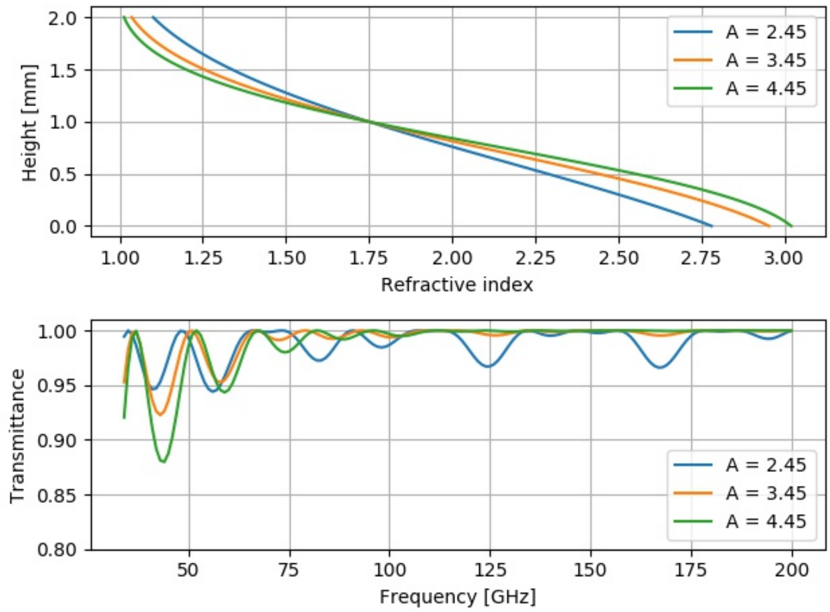

FIGURE 3.2: Upper panel is the index profile which shows a relation between the refractive index and the height of total layers with a parameter A of 2.45, 3.45, and 4.45. Lower panel shows the transmittance calculation which corresponds to the Klopfenstein index profile with the thickness of 1.0 mm. The reflective index is set as 3.06 and no loss tangent.

Square of f, f^2 is equal to the occupancy of a material in a grating. Then 0th ordered EMT can be written as

$$\tilde{n} = \left(1 - f^2\right) n_1 + f^2 n_2, \tag{3.17}$$

where n_1, n_2 are the refractive index of incident, and structures respectively. While Eq. 3.17 means the weighted average of refractive index of two materials, this is only rough approximation; in particular, for a given relative layer thickness f the effective index becomes too large for a large refractive index [37]. From the 2nd ordered EMT follwing as

$$\epsilon_{\parallel}^{(2)} = \epsilon_{\parallel}^{(0)} \left[1 + \frac{\pi^2}{3}\left(\frac{p}{\lambda}\right)^2 f^2 (1-f)^2 \frac{(\epsilon_2 - \epsilon_1)^2}{\epsilon_0 \epsilon_{\parallel}^0}\right] \tag{3.18}$$

$$\epsilon^{(2)} = \epsilon^{(0)} \left[1 + \frac{\pi^2}{3}\left(\frac{p}{\lambda}\right)^2 f^2 (1-f)^2 \times (\epsilon_2 - \epsilon_1)^2 \frac{\epsilon_{\parallel}^{(0)}}{\epsilon_0} \left(\frac{\epsilon^{(0)}}{\epsilon_1 \epsilon_2}\right)^2\right] \tag{3.19}$$

$$\hat{\epsilon}_{2-D}^{(2)} = (1-f)\epsilon_1 + f\epsilon^{(2)} \tag{3.20}$$

$$1/\check{\epsilon}_{2-D}^{(2)} = (1-f)/\epsilon_1 + f/\epsilon_{\parallel}^{(2)} \tag{3.21}$$

We obtain the more accurate approximation

$$n_{2-D}^{(2)} = (\bar{n} + 2\hat{n}_{2-D}^{(2)} + 2\check{n}_{2-D}^{(2)})/5. \tag{3.22}$$

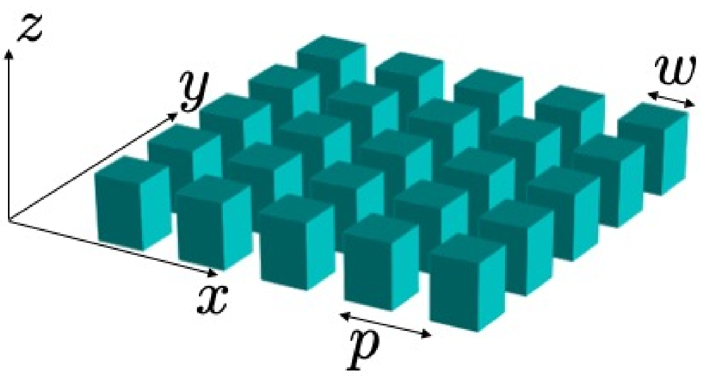

FIGURE 3.3: Image of the 2-dimensional grating structure. Here we set the geometrical parameters; width of a pillar (w) and pitch of gratings (p)

3.4 Simulation based on RCWA method

For the calculation for periodic array of pyramidal structures, Rigorous couple wave analysis (RCWA method) gives the high accuracy. In the RCWA, we assume that a structure repeats periodically in x and y infinitely. Then we slice the periodical structure into hundreds of thin layers in z direction, that is the vertical direction. We calculate the permittivity distribution in each layer and which the Fourier transformation is applied to. We solve the Maxwell's equation with a boundary condition of each layer in the Fourier space. The detail calculation is described by Moharam et al. [38].

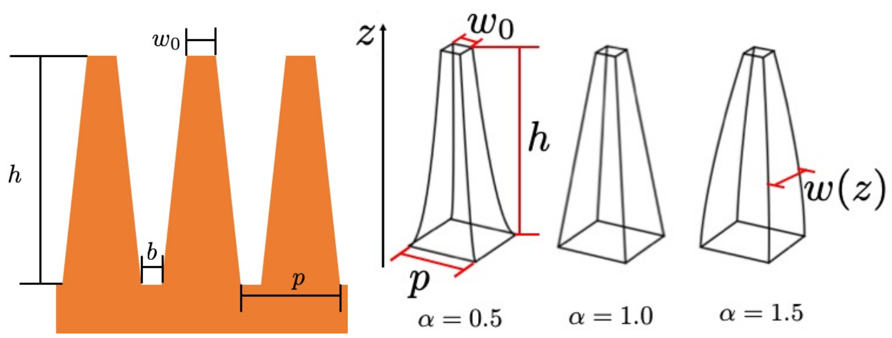

FIGURE 3.4: Geometrical parameters of a pyramidal structure. Left picture shows the cross section of pyramidal structures. We define 4 parameters, top width of the structure w_0, periodic width p, groove width b, and the height of the structure h. Right picture shows the structure shape with new geometrical parameter α. The structure width $w(z)$ is the function of the structure width with height. Left one is the outline with $\alpha = 0.5$ (Mt. Fuji shape), the center is $\alpha = 1.0$ (pyramidal shape), right is $\alpha = 1.5$ (bell shape).

We model one unit of an SWS as shown in left side of Fig. 3.4. The simplest structural model can be described by the three parameters, pitch p, top-width w_0, and height h. In order to match the index profile with Klopfenstein, we define the structure width as

$$w(z) = w_0 + (p - w_0)\left\{1 - (z/h)^\alpha\right\}. \tag{3.23}$$

with a parameter of α. Fig. 3.4 also shows the example of the three representative α values. $\alpha = 1.0$ shows a straight pyramidal shape, $\alpha = 0.5$ is a concave, "Mt. Fuji" shape and $\alpha = 1.5$ is a convex, bell shape. Firstly, we constrain the parameters except α. The groove width b become to be negligiblly small in case of the laser ablation. At the highest frequency limit of ν_c >163 GHz, the corresponding $\lambda_c <$ 1.836 mm. Assuming an extra-ordinary index of sapphire as $n \simeq 3.4$, the pitch $p < \lambda_c/n = 0.54$ mm is chosen.

Then we optimize the set of parameters, (h, w_0) with fixing the pitch as 0.54 mm and α of 1.0. We compute the transmittance over the broadband for various combination of the height and the top-width using electromagnetic wave simulator named "DiffractMOD", which is based on RCWA method [39]. The top panel of Fig. 3.5 shows the typical transmittance given the SWS parameters. The higher the SWS the better the transmittance is at the lower frequency. In order to evaluate the broadband performance, we define the figure-of-merit in this optimization as the averaged transmittance between 34 and 161 GHz. The bottom panel of Fig. 3.5 shows the averaged transmittance for various parameters. The result shows that the top-width has a broad optimal around $0.1 \sim 0.2$ mm depending on the SWS height. In case of the height, it is limited by the fabrication capability although it is desired for the SWS height to be as tall as possible for a broadband optimization. As a result, we define the required SWS designed as $h > 2.0$ mm and $w_0 = 0.15$ mm. The top of

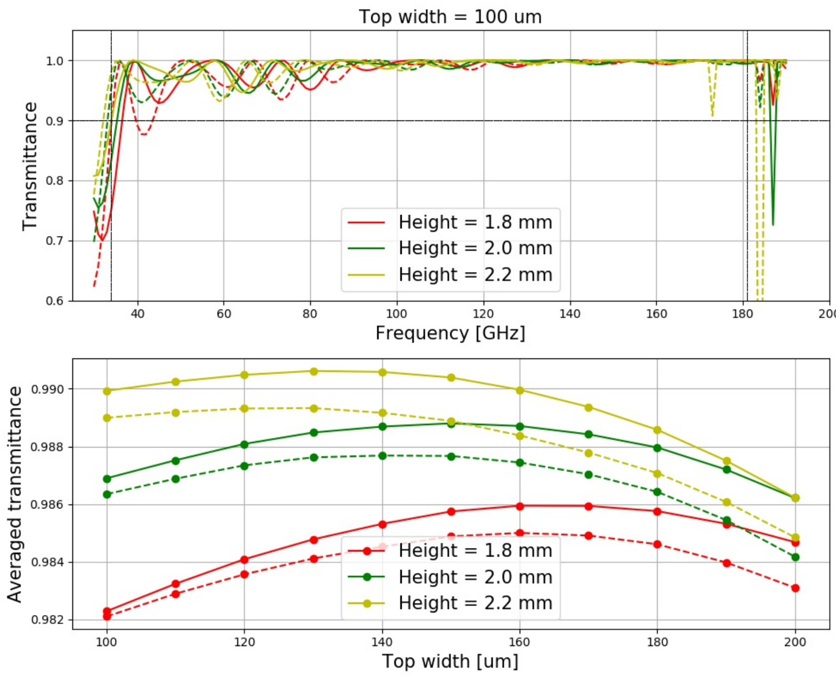

FIGURE 3.5: Top panel shows one of the estimations using DiffractMOD for the parameters of the h and w_0. We put such structures both sides on the flat plate which thickness is 3.0 mm. This plot shows the case $w_0 = 100$ ¯m and 3 lines of $h = 1.8,\ 2.0,\ 2.2$ mm. The birefringent refractive index is set as $n_o, n_e = 3.047, 3.361$. Bottom panel shows the averaged transmittance of each parameters between 34 and 161 GHz.

Figure 3.6 shows the index profiles along the z axis for α value, 0.5, 1.0, and 1.5 computed based on the second order EMT [37]. We also overplot a Klophenstein profile as a comparison with $A = 3.45$. The comparison indicates that the Klophenstein profile is closely match to the case of $\alpha = 1.5$.

The bottom of Fig. 3.6 shows the transmittance for three different α values, 0.5, 1, and 1.5. It is clear that $\alpha = 1.5$ is preferable in a broadband usage. In a quality, when α becomes smaller than 1.0, the shape will approach a pillar with a width of w_0, and it behaves as a single layer AR coating. When α becomes larger than 1.0, the shape will become fatter with keeping the bell shape. Since a bell shape keeps the smooth index profile, it achieves high transmittance in broadband frequencies.

Therefore, our SWS design is to aim the following parameters as $p < 0.54$ mm, $w_0 = 0.15$ mm, $h > 2.0$ mm, and $\alpha \sim 1.5$. Note that we can further optimize the parameter in details but we did not pursue beyond this point. This is largely due to the fact that the exact machined SWS shape using a laser machining comes out to be not exactly the same as we design.

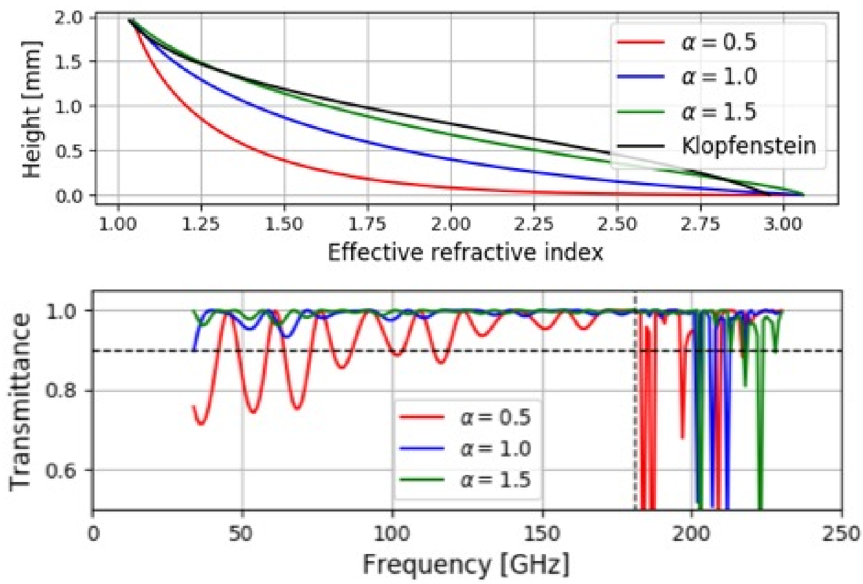

FIGURE 3.6: Top panel shows the effective refractive index by using second order EMT. Black curve shows the Klopfenstein index profile with $A = 3.45$. Bottom panel shows the transmittance calculation by RCWA method for α dependence.Red, blue, green line is the transmittance when the $\alpha = 0.5, 1.0, 1.5$ respectively. We can see the spikes at higher frequencies because of the diffraction effect.

Chapter 4

Fabrication of SWS

In the previous chapter, we describe that we need to fabricate the structure at least over 2.0 mm with the pitch of under 0.54 mm, and also achieve $\alpha \sim 1.5$. However, we had following problems with respect to fabricating SWS;

- Difficulty to make over 2 mm structures.
- Difficulty to make the structure with $\alpha > 1.0$.
- Break in structure due to high power laser machining
- Speed of fabrication to cover over a diameter of 450 mm in a practical time.

Our recent developments improve these problems. In this chapter, we describe the improvement in terms of the laser machining system itself and the scan strategy. In the later section, we summarize the fabrication results and the processing times for covering each fabrication area, and expect the processing time over a diameter of 450 mm.

4.1 Overview of fabricated samples

Tab. 4.1 shows the summary of fabricated samples we will introduce later. There are 6 samples with the fabricated date. First demonstration sample, called ELAS sapphire3, was fabricated by the laser company ELAS in Lithuania. Actually we have two directions for the satelite project, one is to make the real size by ourselves, the other is to request to make the real size SWS to a company. ELAS sapphire 3 is aiming for the second way. The transmittance measurement was done by T. Matsumura and I predicted the transmittance by RCWA and compared with the measurement. All samples except ELAS sapphire3 were fabricated, measured, and predicted by R.Takaku. The second two samples, called Minimaster 8 and 9, were made by Minimaster which is our first laser machine. These samples are made by same scan strategy. This is because we plan to eventually use the sapphire as a part of the Pancharatnam multi-stacked achromatic HWP. As a result, we intend to demonstrate the two sapphire plates which is located as an interface between the sapphire substrate and vacuum. The sample named Takaku3 test4 is applied the new scan strategy to make bell shape by Minimaster. We cannot measure the transmittance because the fabricated area is only 1.6 mm $\times$ 1.6 mm. The samples made by Pharos, higher power laser machine than Minimaster, is called Pharos 8 and 9. These samples are also made by same scan strategy. The difference specification of these lasers is shown in Sec. 4.2. The improvement of scan strategy is described in Sec. 4.3. And the shape measurement of these 6 samples is shown in Sec. 4.4.

TABLE 4.1: Summary of our samples

Date	Used laser name	Sample name	Scan strategy
2018/03	ELAS laser	ELAS sapphire 3	Linear scan strategy
Fabricated by ELAS, Measured by T.Matsumura, predicted by R.Takaku			
Good agreement with the prediction, however the shape is Mt.Fuji.			
2018/05	Minimaster	Minimaster 8 and 9	spiral scan strategy
Fabricated, Measured, and Predicted by R.Takaku			
Discrepancy between measurement and prediction, and fabrication time of $\sim$3 days			
2018/09	Minimaster	Takaku3 test4	new scan strategy
Fabricated, Measured, and Predicted by R.Takaku			
Bell shape and successfully reduce the processing time even though it is impractical			
Cannot measure the transmittance due to the fabrication structure number of 3×3			
2019/01	Pharos	Pharos 8 and 9	new scan strategy
Fabricated, Measured, and Predicted by R.Takaku			
Bell shape and successfully reduce the processing time drastically.			

4.2 Laser machines

For the demonstratin, we used a 3 W nano-second pulsed laser called as "Minimaster" , at Kavli IPMU. Its specification is shown in Tab. 4.2. This laser machining system is come from ELAS, a laser company in Lithuania. Minimaster includes a laser itself, an UV-galvano system and a small xyz-stage. Galvano system consists of two mirrors and a $f\theta$ lens. We control the laser orbit by the two mirrors, it enable us to be fast scanning the laser. The laser is focused by the $f\theta$ lens with the same focus distance in a diameter of 70 mm. We cannot control the position of the sample stage automatically except z-stage.

TABLE 4.2: The specifications of laser machining system

Laser name	Minimaster	Pharos
Location	Kavli IPMU	Hongo campus
Wavelength	355 nm	1030 nm
Pulse duration	< 35 ns	290 fs
Averaged power	3 W	15 W
Repetition rate	20 kHz	75 kHz
Pulse energy	150 μJ	200 μJ
Peak power	4.3 kW	1.0 GW
Galvano system spesifications		
Working range	d = 70 mm	d = 70 mm
Spot size	7 μm	15.5 μm
Rayleigh length	0.43 mm	0.73 mm
Max speed of scanning	12 m/s	12 m/s

Since Minimaster has low power, long pulse duration, and low repetition rate, we update the laser from Minimaster to "Pharos" (Pharos-15W-1MHz/OSOUT500). Pharos is bought by Gomokami-Yumoto laboratory from Lithuania. We combine it with an IR-galvano system and a xyz-stage (Sigma, OSMS20-35) in order to construct a laser machining system. Its specification is also shown in Tab. 4.2. The most different parameters of Pharos with Minimaster are the wavelength, the averaged power,

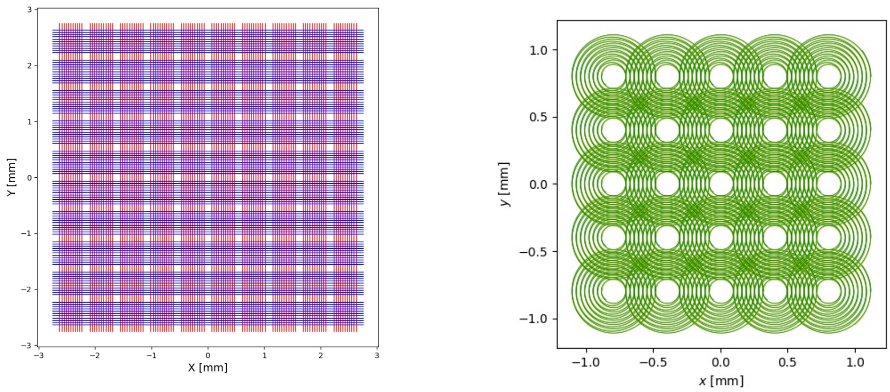

FIGURE 4.1: Outline of linear and spiral scan strategies. Linear scan strategy consists of orthogonal lines, while spiral scan strategy consists of 4 spirals for each structures.

the pulse duration, and the repetition rate. The pulse duration of Pharos is 290 fs, much shorter than that of Minimaster. This results much higher peak power, and the ablation becomes non-thermal processing. We are also able to scan the laser faster than Minimaster by high repetition rate and high averaged power. Pulse energy E_p is calculated by $E_p = P_{ave}/f$, and Peak power P_p is calculated by $P_P = E_p/t$, where the P_{ave} is the averaged power, f is the repetition rate, and t is the pulse duration. The spot size of Minimaster and Pharos are measured directly by a CCD camera. Then the rayleigh length is calculated by

$$z_R = M\frac{\pi w^2}{\lambda}, \tag{4.1}$$

where w is the radius of beam west at the focus position and λ is the laser wavelength. M is the factor to evaluate the beam shape. $M = 1$ means the perfect Gaussian beam.

We use a xy-stage in order to cover a large area which is described in Chapter 6. Since the range of linear stage is small, we use it for only the demonstration for the large area fabrication in the future.

4.3 Scan strategy

4.3.1 Previous scan strategy

There were linear and spiral scan strategy to make structures. The outlines of these strategies are depicted in Fig. 4.1. The similar point of these strategies is that we scan such a particular pattern many times with skipping the part of the top. The difference between two scan strategies is that the shape of fabricated structure is pyramidal shape by liner scan while conical shape by spiral scan. Fig. 4.2 shows geometrical parameters of linear and spiral scan strategies. Basically there are 3 parameters for linear scan strategy; line length ℓ_l, line width ℓ_w, and line space ℓ_s. Then line number n_l becomes $\ell_w/\ell_s + 1$. The line width ℓ_w is limited by the designed structure pitch. The order and direction of scanning are also controllable parameters, but typically we fix them in order to reduce the processing time. First we scan all vertical lines from the -Y direction to the + Y direction, and the scanning direction of

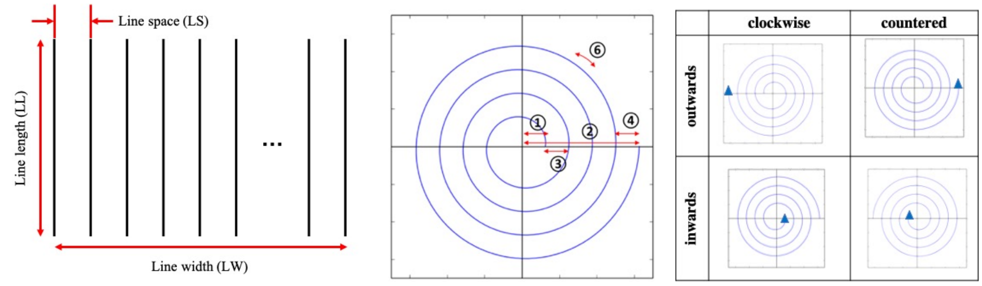

FIGURE 4.2: Geometrical parameters of linear and spiral scan strategies.

lines alternates between plus and minus. The horizontal lines are as same as vertical lines.

For the spiral scan strategy, the parameters are inner radius r_i, starting and ending pitch which corresponds to the line space in the line scan strategy, and the direction how to depict the spiral(clockwise or counter clockwise, inwards or outwards). For the spiral scan strategy, the inner radius r_i is determined how we remain the top width w_o structure. In order to remain the top of the structures, the outer radius r_o is determined by $r_o = p - r_i$ where p is the designed pitch. It is more complicated to find the optimal parameter combination in spiral scan strategy than in linear scan strategy because one parameter depends on adjacent structures.

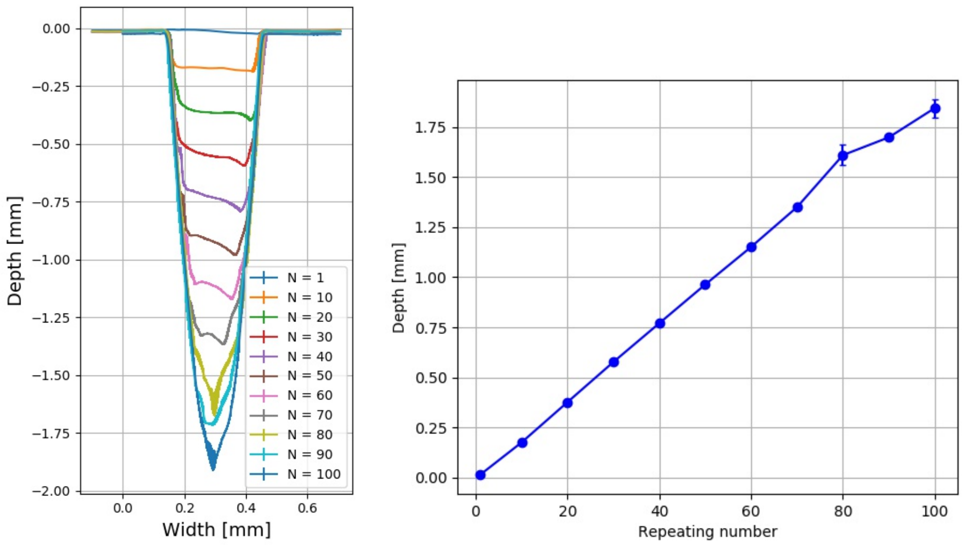

FIGURE 4.3: Left panel shows the cross section made by a linear scan strategy as a function of repeating number from N = 1 to 100. Right panel shows the groove depth as a function of the repeating number.

There are a few problems to use these scan strategies for structure machining. Fig. 4.3 shows cross sections of grooves made by line scan strategy and the depth dependence on the repeating number N. In this fabrication, we fix the scan parameter as $\ell_l = 3.0$ mm, $\ell_w = 0.306$ mm, $\ell_s = 0.009$ mm. The scan speed is also fixed as 20 mm/s during the machining. The result seems that the shape of cross sections has been already determined before the ablation. The shape is also MT. Fuji shape which means $\alpha < 1.0$. The angle of structure slope is called as "Flank angle θ_{fl}" by. V.

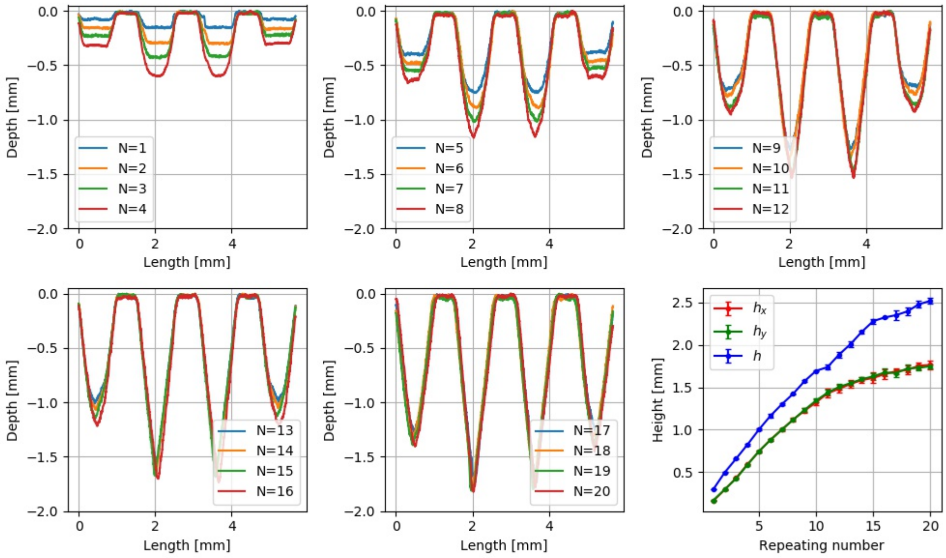

FIGURE 4.4: 6 subplots show the cross section of structures made by spiral scan strategy as a function of repeating number from N = 1 to N = 20, and structure height in x and y direction, and total height from the corner to the top.

Schütz et al.[33] and it determined as Eq. 4.2.

$$\theta_{fl} = \tan^{-1} \frac{2h}{(p - w_0)^2}. \tag{4.2}$$

The flank angle θ_{fl} should reach a particular angle which corresponds to the cross point of the threshold and the projected fluence determined as

$$\Phi_{pro} = \frac{4E_p}{\pi d_{pro}^2}. \tag{4.3}$$

This means that even if we repeats many times at top of the structure, there is no more interaction between laser and material. Thus, we waste the processing time, and we can only make the structures with $\alpha < 1.0$. There is the same problem in the spiral scan strategy. Fig. 4.4 shows the cross section of structures made by spiral scan strategy and its depth dependence on the repeating number N. In Fig. 4.4, we made 3 by 3 structures and cut it in the center. The definition of h_x and h_y is the height from top to the bottom in the x-side and y-side, while h_t is the height from top to corner. The reason why h_t is higher than h_x and h_y is that The laser scans 2 times at the corner compared with the side. The result also shows that the there is a limit height that we can make. Furthermore, if we use a high power laser such as a Pharos, too many repeating at a top of the structure would break the top of the structures.

4.3.2 New scan strategy

We develop a new strategy based on the linear scan in order to solve the above problems. Fig. 4.5 shows the image of new scan strategy named recipe T, and the example of cross section of V groove. Recipe T is processed that the line width decreases by reducing the line space with repeating number without changing the line number. This strategy can focus on the groove fabrication and remain the top of structures, in other words make a structure with $\alpha > 1.0$. Fig. 4.5 the comparison between the old scan strategy and the new scan strategy. Blue one is the old line scan strategy with the parameters of line width ℓ_w = 0.3 mm, line space ℓ_s = 0.015 mm, and repeating number N = 100. Red one is the recipe T with the parameters shown in Tab. 4.3. This result shows the recipe T can make a deeper groove compared with old linear scan strategy in a same time. The shape of the groove also achieved $\alpha > 1.0$. In order to search the best combination of parameter, we can make a bell shape structure.

TABLE 4.3: Example table of recipe T.

Line width [mm]	Line space [mm]	Line number	Repeating number
0.3	0.015	21	10
0.28	0.014	21	10
0.26	0.013	21	10
0.24	0.012	21	10
0.22	0.011	21	10
0.2	0.01	21	10
0.18	0.009	21	10
0.16	0.008	21	10
0.14	0.007	21	10
0.12	0.006	21	10

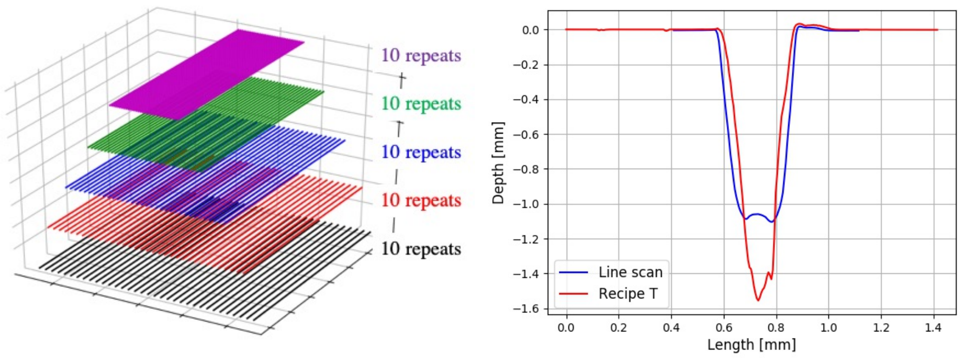

FIGURE 4.5: Brief image of recipe T. Scan processes from black lines to purple lines. The line space decreases with repeating number without changing the line number.

4.3.3 Scan parameters for structure fabrication

We introduce the processing parameters of 5 samples named Minimaster 8 and 9, Takaku3 test4, and Pharos8 and 9. Minimaster 8 and 9 are made by old spiral scan strategy with Minimaster. Takaku3 test4 is made by recipe T with Minimaster. And Pharos 8 and 9 are made by recipe T with Pharos.

We have done a hundred of trials to find the parameter combination which can make the allowable structures. What we show here is one of the example settings to make over 2 mm structures but not the optimal recipe. Tab. 4.4 shows the parameter settings except the scanning parameters for each sample. The value of focus position means the position from the sample surface, thus we set the focus position inside a material. The fabricated area for Minimaster 8 and 9 is over a diameter of 21 mm, which is the minimum size for transmittance measurement. We only make 3 by 3 structures in Takaku3 test4 because this sample is only for the shape demonstration. We can set the scan speed of 300 mm/s for Pharos8 and 9 compared with Minimaster samples due to large repetition rate. The jump speed is the speed during no fabrication, thus we fix it as 2000 mm/s. The scanning parameters for each sample is shown in Tab. 4.5.

TABLE 4.4: Parameter settings for each sample fabrication.

Sample name	Minimaster 8 and 9	Takaku3 test4	Pharos 8 and 9
Focus position	-0.75 mm	-0.75 mm	-0.75 mm
Fabricated area	in ϕ = 21 mm	3×3 structures	in ϕ = 34.5 mm
Used laser name	Minimaster	Minimaster	Pharos
Averaged power	3 W	3 W	15 W
Repetition rate	20 kHz	20 kHz	75 kHz
Scan speed	20 mm/s	20 mm/s	300 mm/s
Jump speed	2000 mm/s	2000 mm/s	2000 mm/s

TABLE 4.5: Scanning parameters for each sample

Minimaster 8 and 9 geometrical parameters	
Outer radius	0.32
Inner radius	0.08
Starting and ending pitch	0.009
Targeted structure pitch	0.4
Repeating number	17

Takaku3 test4 geometrical parameters			
Line width [mm]	Line space [mm]	Line number	Repeating number
0.306	0.009	34	5
0.272	0.008	34	5
0.238	0.007	34	10
0.204	0.006	34	10
0.17	0.005	34	10
0.144	0.004	34	10
0.102	0.003	34	20

Pharos 8 and 9 geometrical parameters			
Line width [mm]	Line space [mm]	Line number	Repeating number
0.468	0.009	53	6
0.416	0.008	53	10
0.364	0.007	53	10
0.312	0.006	53	10
0.26	0.005	53	10
0.208	0.004	53	10
0.156	0.003	53	5

The scanning process of Minimaster 8 and 9 is as follow;

1. scan a spiral with clockwise-outwards direction
2. scan a spiral with counter clockwise-inwards direction.

3. scan a spiral with counter clockwise-inwards direction.
4. scan a spiral with clockwise-outwards direction.
5. machine 5×5 structures by the scan No.1$\sim$4.
6. Repeats a series of scanning in 17 times, called as a unit.
7. Tile this unit in a diameter of 21 mm.

Minimaster 8 and 9, and Takaku3 test4 targeted the structure with the pitch of 0.4 mm, while Pharos 8 and 9 with 0.54 mm. In the fist 10 repeating for Takaku 3 test 4 is to make the targeted bell shape. There is similar reason for Pharos 8 and 9, and we also avoid to break the top of structures due to the excessive scanning. In Tab. 4.5, the repeating number for the first scanning in the table of Pharos8 and 9 on the top is set as 6, which comes from the possibility of cracks with more repeating number and wider line width. This parameter set is the upper limit. We also stop the last repeating number as 5 for Pharos 8 and 9 as the structure will be completely broken due to the excessive scanning.

4.4 Fabricated samples

Fig. 4.6 shows the pictures of all fabricated samples. Upper light picture is ELAS sapphire 3 made by ELAS company. There are hundred of structures within the white colored area. Pharos 8 and 9 on the right two picture also shows same white color. While Minimaster 8, 9 and Takaku4 test4 has brown color. We shall discuss about that color in Chapter 6. Takaku3 test4 has only 3 by 3 structures, and we point it by red arrow. The structure image is taken by laser con-focal microscope VK4 (Keyence) as shown in Fig. 4.7. The shape of minimaster 8 and 9 is conical, while other samples has the pyramidal shape because of the type of scan strategies. The geometrical parameters of these samples are summarized in Tab. 4.6. Basically we measure the top width w_0, height h, and pitch p in x and y direction. The curvature α is the fitting results by the Bräuer 2nd ordered EMT. We measure 3 by 3 structure in 5 different locations except takaku3 test4; center north, south, east, and west side locations, and take the average and standard deviation of measured parameters. It is difficult to measure the top width w_0 because the fabricated shape has not critical edge which divide the top by slope, thus we define the top width as 98% of h_x and h_y. The targeted pitch of ELAS sapphire 3, Minimaster 8, and Minimaster 9 is 0.4 mm, and measured pitch of them is close to 0.4 mm. Also the targeted pitch of Pharos 8 and Pharos 9 is 0.54 mm which measurement are good agreement with the design. The total height of all samples is over 2.0 mm, which is taller than our design. The top width is a little smaller than our design, however it is difficult to make wider structure with deep height structure. The curvature α made by old line, and spiral sample is smaller than 1.0, while our new scan strategy has over 1.0. Fig. 4.8 shows the effective refractive index profile as a function of a depth for each samples. These curve is calculated by the 2nd ordered EMT. The black curve shows the klopfenstein index profile as a reference with $A = 3.45$. The profile of Takaku3 test4 and Pharos8, 9 can approach the Klopfenstein index profile well.

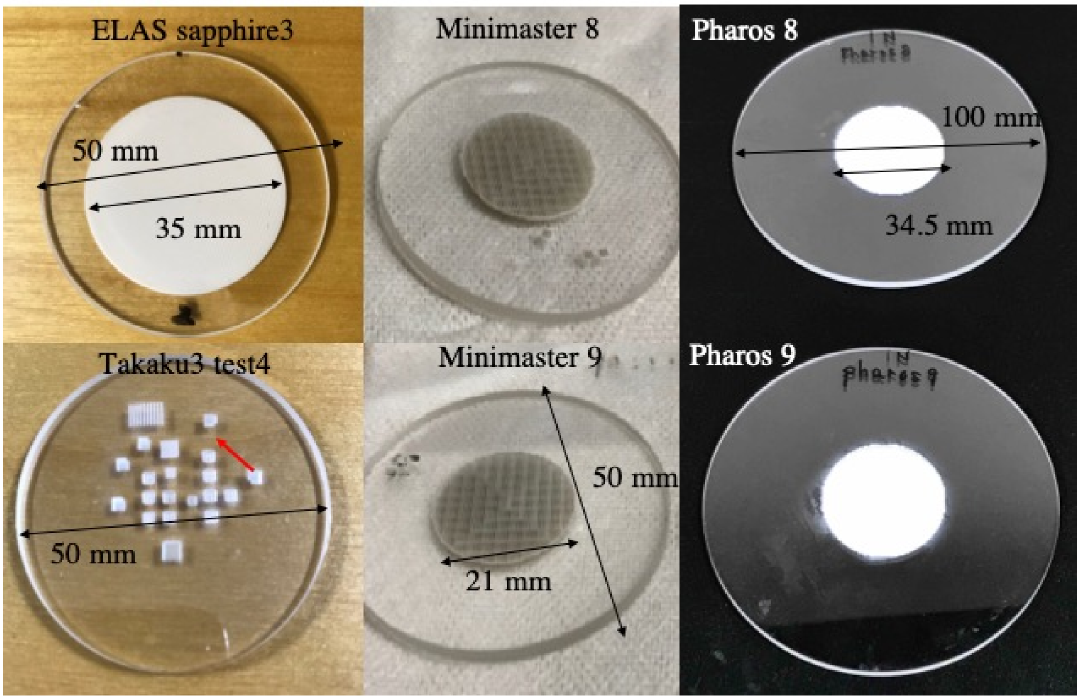

FIGURE 4.6: Pictures of all fabricated samples.

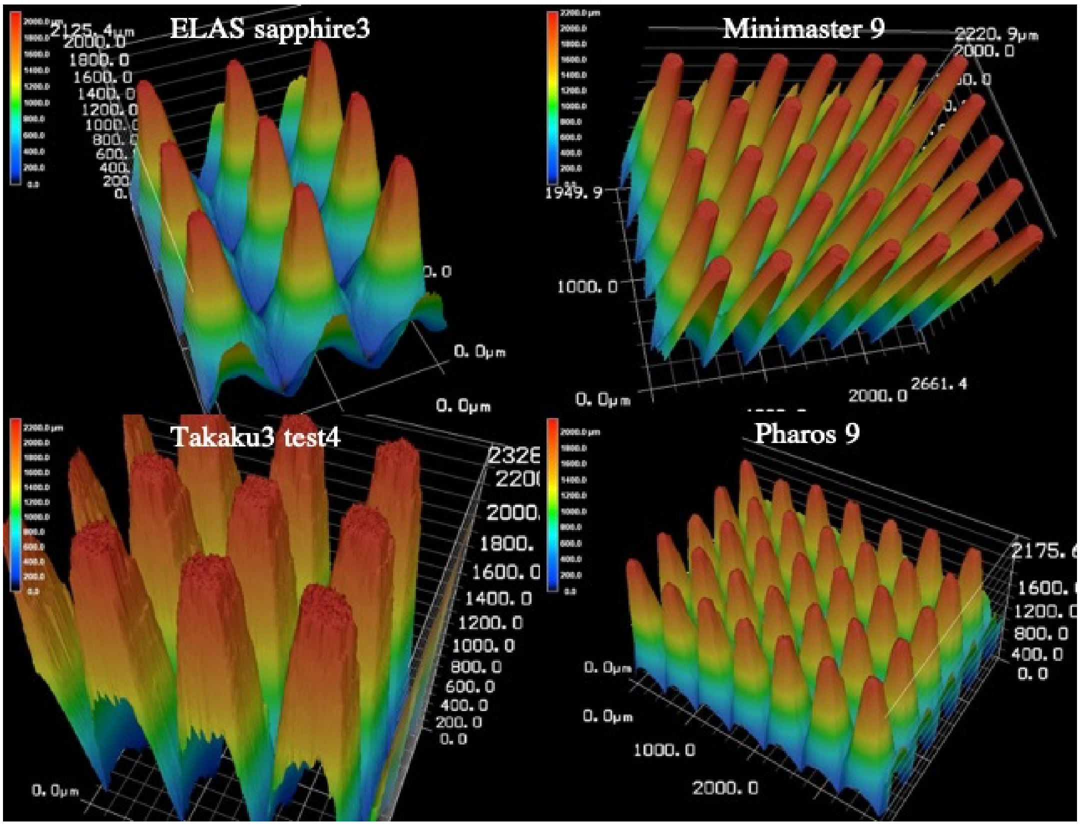

FIGURE 4.7: 3D image of each sample taken by laser con-focal microscope.

TABLE 4.6: measured geometrical parameters for each fabricated samples. α is come form the fitting with 2nd ordered EMT.

Sample name	Top width (w_0) [mm]	Height (h) [mm]	Pitch (p) [mm]	curvature (α)
ELAS sapphire3	$w_{0x} = 0.060 \pm 0.006$ $w_{0y} = 0.066 \pm 0.003$	$h_x = 1.62 \pm 0.018$ $h_y = 1.63 \pm 0.02$ $h_t = 2.11 \pm 0.014$	$p_x = 0.400 \pm 0.002$ $p_y = 0.400 \pm 0.002$	$\alpha_x = 0.88 \pm 0.007$ $\alpha_y = 0.88 \pm 0.008$
Minimaster 8	$w_{0x} = 0.120 \pm 0.019$ $w_{0y} = 0.146 \pm 0.013$	$h_x = 2.01 \pm 0.07$ $h_y = 1.62 \pm 0.08$ $h_t = 2.26 \pm 0.16$	$p_x = 0.401 \pm 0.006$ $p_y = 0.401 \pm 0.006$	$\alpha_y = 0.75 \pm 0.08$ $\alpha_x = 0.90 \pm 0.08$
Minimaster 9	$w_{0x} = 0.121 \pm 0.021$ $w_{0y} = 0.123 \pm 0.017$	$h_x = 2.05 \pm 0.06$ $h_y = 1.71 \pm 0.11$ $h_t = 2.37 \pm 0.14$	$p_x = 0.400 \pm 0.006$ $p_y = 0.398 \pm 0.004$	$\alpha_x = 0.78 \pm 0.04$ $\alpha_y = 0.92 \pm 0.07$
Takaku3 test4	$w_{0x} = 0.140 \pm 0.011$ $w_{0y} = 0.139 \pm 0.007$	$h_x = 1.96 \pm 0.02$ $h_y = 1.56 \pm 0.03$ $h_t = 2.29 \pm 0.03$	$p_x = 0.398 \pm 0.002$ $p_y = 0.400 \pm 0.005$	$\alpha_x = 1.02 \pm 0.013$ $\alpha_y = 1.41 \pm 0.041$
Pharos 8	$w_{0x} = 0.115 \pm 0.024$ $w_{0y} = 0.119 \pm 0.017$	$h_x = 1.59 \pm 0.03$ $h_y = 1.76 \pm 0.02$ $h_t = 2.13 \pm 0.03$	$p_x = 0.540 \pm 0.008$ $p_y = 0.536 \pm 0.005$	$\alpha_x = 1.49 \pm 0.02$ $\alpha_y = 1.35 \pm 0.02$
Pharos 9	$w_{0x} = 0.117 \pm 0.024$ $w_{0y} = 0.110 \pm 0.02$	$h_x = 1.58 \pm 0.03$ $h_y = 1.74 \pm 0.02$ $h_t = 2.13 \pm 0.04$	$p_x = 0.536 \pm 0.005$ $p_y = 0.537 \pm 0.004$	$\alpha_x = 1.50 \pm 0.03$ $\alpha_y = 1.36 \pm 0.03$

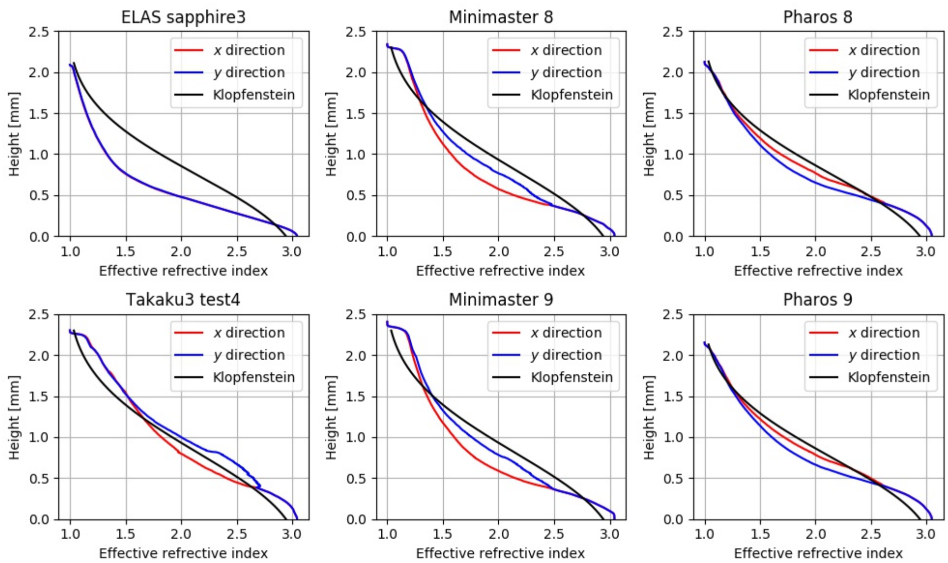

FIGURE 4.8: The effective refractive index profile as a function of the depth. The index profile of the sample is calculated by 2nd ordered EMT. Black curve shows the Klopfenstein index profile as a reference with $A = 3.45$ and the height corresponds to each sample height.

4.5 Prospective processing time for large area fabrication

The fabricated samples described in the previous section have geometrical parameters close to our design. However there are still other problems, the processing time. For the LiteBIRD, we have to cover over a diameter of 450 mm. As a reference, expected processing time is calculated as

$$\text{Expected processing time} = \frac{\pi(450/2)^2}{\text{Fabricated area}} \times \text{Processing time.} \tag{4.4}$$

TABLE 4.7: Summary of expected processing time for each sample.

Sample name	Fabricated area	Processing time	Processing time over $\phi = 450$ mm
Minimaster 8, 9	over ϕ = 21 mm	72 hours	3.77 years
Takaku3 test4	1.6 mm $\times$ 1.6 mm	0.5 hours	3.54 years
Pharos8, 9	over ϕ = 34.5 mm	10.5 hours	0.2 years

We have the processing time except ELAS sapphire 3 and summarized as shown in Tab. 4.7 The processing time of Minimaster 8, 9, and Takaku3 test4 have much longer time because the Minimaster has very low averaged power 3W and longer pulse duration thus low peak power and low ablation rate. The prospective time over a few years is impractical for any projects. While in the case of Pharos 8, 9, which are made by 15 W femto-sec. pulsed laser, it takes 2.5 month to cover over a diameter of 450 mm. We can drastically reduce the processing time compared with Minimaster. Although there is not a strict goal of fabrication time over a diameter of 450 mm area, we would like to reduce it by within 1 month. For reducing the processing time more and more, we need to optimize the hundred combination of scan parameters, and also much higher power laser machine. The future work for high power laser machining is discussed in Chapter 7.

Chapter 5

Optical transmission

5.1 Measurement system

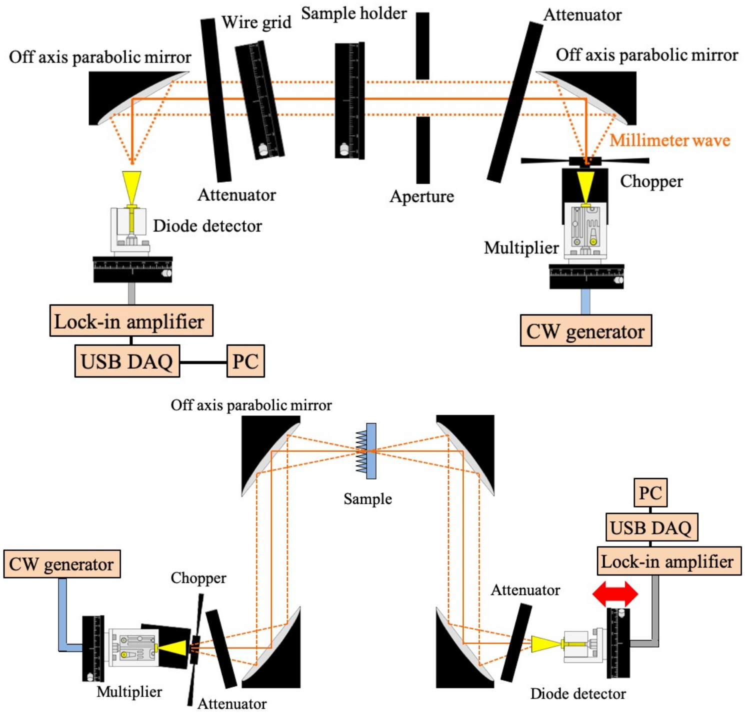

FIGURE 5.1: Sketch of the planed(upper) and focused(Bottom) transmittance measurement setup

Fig. 5.1 is the schematic view of the two types of transmittance measurement systems at Kavli IPMU. On the upper sketch of Fig.5.1, we generate the continuous wave using the synthesizer between 8 GHz and 15 GHz. Then, the incident wave from the synthesizer is multiplied by using a multiplier. We use 5 types of multipliers (Q band:$\times$ 4, 33-50 GHz, V band:$\times$ 4, 50-75 GHz, W band:$\times$ 6, 75-110 GHz, F band:$\times$ 8, 90-140 GHz, G band:$\times$ 12, 150-190(220) GHz). We place a chopper of which frequency is at 30 Hz in front of the multiplier to modulate the signal. The modulated signal is reflected at the first mirror to make a parallel wave to the sample holder. The sample holder has the aperture of 30 mm, which is set due to the fabricated SWS diameter of 34.5 mm. Then, the transmitted signal is reflected at the second mirror and detected by a diode detector at the focus position. We measure the transmittance by taking the ratio between the measured power with and without a sample. In order to delete the effect of the standing wave, we take the average of the two measured outputs at the two positions along the optical path where are separated by $\lambda/4$.

The other measurement system depicted in the bottom sketch of Fig. 5.1 is similar to pnale wave setup, the difference is that we focus the signal by adding more 2 mirrors. We put the sample at the focused position, and thus we can measure the transmittance even if the fabricated area is small. It is useful in particular for the Minimaster samples because it takes over a few days to machine over a diameter of 21 mm. At the gaussian waist, the spot diameter in the measurement bandwidth ranges from 2 mm to 15 mm. The Rayleigh length ranges from 20 mm to 158 mm, which is longer than the sample thickness of about 3 mm. The sample is tilted in the y-z plane by 5 degrees in order to minimize the standing wave along the chief ray. We also inserted attenuators to minimize this effect in the optical path. By using this system, we measure the transmittance of simple flat sapphire sample to show that the result by this system is consistent with the prediction. We fit the data at each bands and calculate RMS of data - fit to estimate the systematic errors for the measurement data.

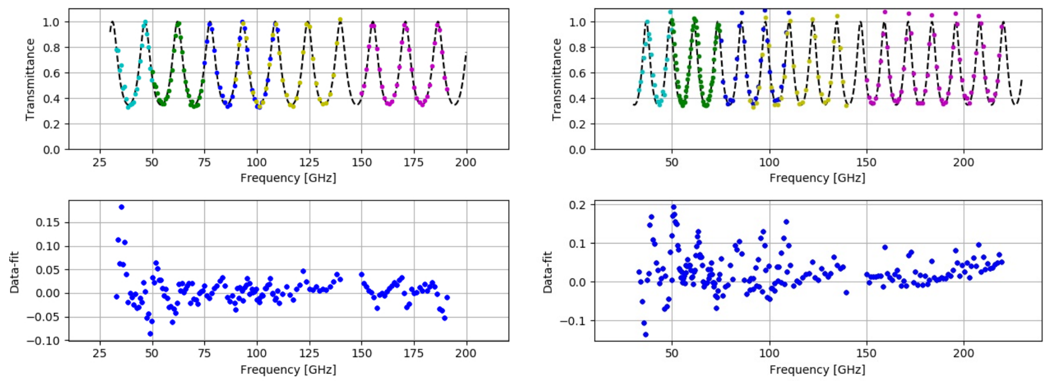

FIGURE 5.2: Transmittance measurement of not fabricated C-cut sapphire as a reference. Left panel is the result by plane wave setup, and Right panel is the result by focused wave setup. Dashed line is the fitting for data. Fitted parameter $n = 3.059$, and loss tangent $\tan\delta = 1.14 \times 10^{-8}$, RMS = 0.031 for pnale wave setup while $n = 3.06$, and loss tangent $\tan\delta = 3.12 \times 10^{-8}$, RMS = 0.057.

Fig. 5.2 shows the transmittance measurement of a flat C-cut sapphire plate and the difference between data and fitting for two different measurement systems. The fit parameter of the refractive index $n = 3.059$, and loss tangent $\tan\delta = 1.14 \times 10^{-8}$ for the plane wave setup, and $n = 3.06$, and loss tangent $\tan\delta = 3.12 \times 10^{-8}$ for the focused wave setup are consistent with Lamb[25]. However, RMS are 0.031 and 0.057 for plane wave setup and focused wave setup respectively. Thus there is a few percent of error for the measurement, basically which is caused from the alignment of the multiplier and detector, and how to measure the transmittance. We use the RMS for each band as a systematic error for the measurement of the fabricated samples as a worst case. We measure the transmittance of ELAS sapphire3, minimaster 8 and 9 by focused wave setup, and of Pharos8 and 9 by plane wave setup. Also we measure the transmittance of the Pharos 8 and 9 stacked back-to-back to evaluate the sample with SWS on both sides. Then we do not glue these samples but fix them by the ring.

5.2 Optical performance

The optical performance of ELAS sapphire 3 is shown in left panel of Fig. 5.3. The data oscillates around 0.74, which caused it is fabricated only on one side. This means if the AR on one side is perfect, we can assume that the reflection can be written as single boundary condition at non-fabricated surface,

$$R = \left| \frac{n_s - n_i}{n_s - n_i} \right|^2 \tag{5.1}$$

where n_s, n_i is the refractive index of material, air respectively. The refractive index of C-cut sapphire n_s is 3.06, and $n_i = 1.0$, therefore R = 0.26. Blue curve is the RCWA calculation based on measured shape. The measurement is consistent with the calculation even though the calculation is not a fit. However if we calculate the prospective performance for a stacking 5-layer AHWP with measured shape on both sides, the result becomes the right side figure on Fig. 5.3. Due to the lower curvature than 1.0, the transmittance at 50 GHz is below to 90%. As a result, although the fabricated shape is good agreement with calculation, there is room for improvement to increase the transmittance at the lowest frequency band by making the structure with the curvature of over 1.0. This result is published by T. Matsumura et al.[40]

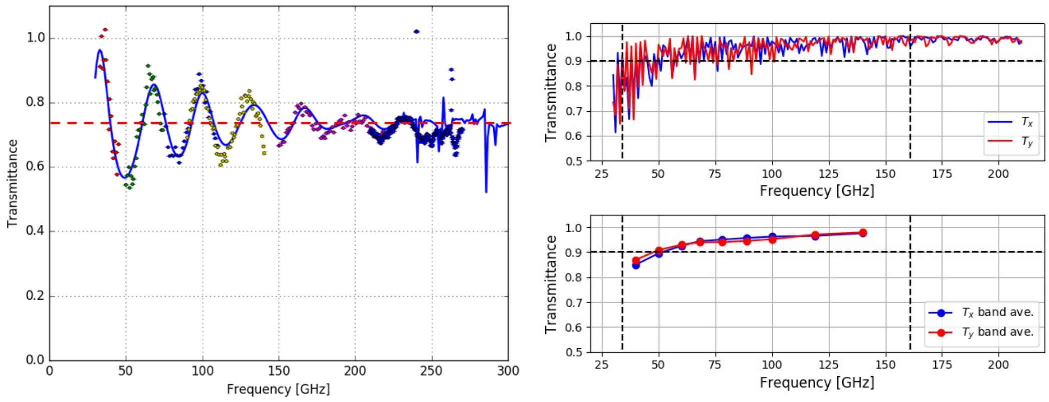

FIGURE 5.3: Transmittance measurement of ELAS sample. Dots are the measurement, and Blue curve shows the RCWA calculation based on measured shape. Red line is the center of oscillation of the transmittance, 0.74. Top panel shows the RCWA calculation of transmittance for 5-layer AHWP with measured shape on both sides. Bottom panel shows its band average in LiteBIRD LFT bands.

Fig. 5.4 shows the measured transmittance of Minimaster 8 and 9 as a function of frequency. We measured the transmittance at two incident direction of polarization, 0 and 90 degrees. Black curve shows the expected value calculated by the RCWA method with the use of measured SWS shape. The measurements drop down smoothly and there is discrepancy between measurements and calculation. We consider that this is come from the absorption effect of the sapphire. There is the possibility that the material on the surface of fabricated structures is changed because of the interaction between the laser and the material. Though we do not have any evidence of reason for this change, at least we can say Minimaster 8 and 9 have a different color compaerd with ELAS sapphire 3. Minimaster 8 and 9 have a brown color, while ELAS sample is white color. Therefore, we tried to clean the surface of two samples by some cleaning methods. We describe this result in Chapter 6.

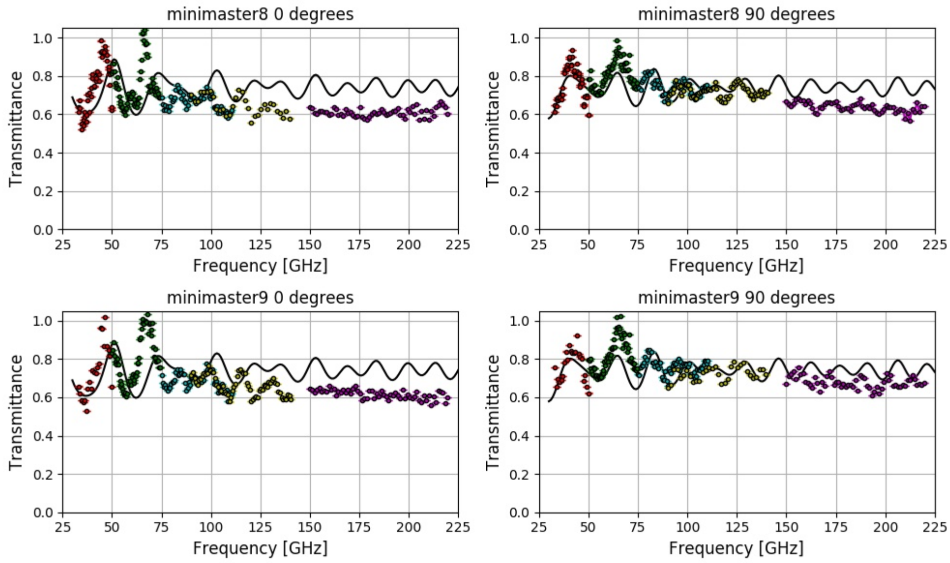

FIGURE 5.4: Transmittance measurement of Minimaster 8 and 9. Top two panels are the results of Minimaster 8, and center two panels show the results of Minimaster 9. We take the transmittance at two directions of the polarization, 0 and 90 degrees. Colored dots are measured data at each bands described in Chapter 4 and black line is the predicted calculation based on measured shape by laser con-focal microscope.

Although we cannot measure the transmittance of Takaku3 test4 due to the small fabrication area, we can estimate the transmittance if we have such a structure in large area as shown Fig. 5.5. This sample is the deepest structure with α is larger than 1.0, thus the calculation shows that all of frequency bands are larger than 0.9. This sample is the best shape in all sample, however it may have larger absorption effect in the measurement because it has the brown color, and also we have to wait a few years to cover this over a diameter of 450 mm.

Fig. 5.6 shows the measured transmittance of Pharos 8 and 9 as a function of frequency. We measured the transmittance at two incident direction of polarization, 0 and 90 degrees as same as Minimaster 8 and 9. The incident angle is fixed as 0 degrees. The top 4 panel shows the transmittance of each single samples. At bottom two panels, we stack 2 samples as if both sides of surface are SWS and measure the transmittance. Colored dots are measurements, and each color corresponds to use the same multiplier. Black curve shows the expected value calculated by the RCWA method with the use of measured SWS shape. We set the refractive index of the sapphire as 3.06 at the room temperature [25]. In the measurement of each samples, the shape of the SWS is asymmetry with 0 and 90 degrees, thus the data has the different phase between 0 degrees and 90 degrees. In the measurement of stacked samples, the transmittance approaches to 1.0 between 40 and 140 GHz. However at higher frequencies, the transmittance drops down smoothly even though the effect is smaller than the result of Minimaster 8 and 9. If we include the loss term $\tan\delta = 7.2 \times 10^{-4}$ into the calculation, the calculation is matched with the measured data. This value is consistent with Lamb [25]. In the measurement of both sides of AR, there is the upper offset at 50 and 120 GHz because we measure the transmittance by taking the ratio the intensity with or without the sample. As a conclusion, we show the transmittance is above 90% between 40 GHz and 181 GHz by using SWS.

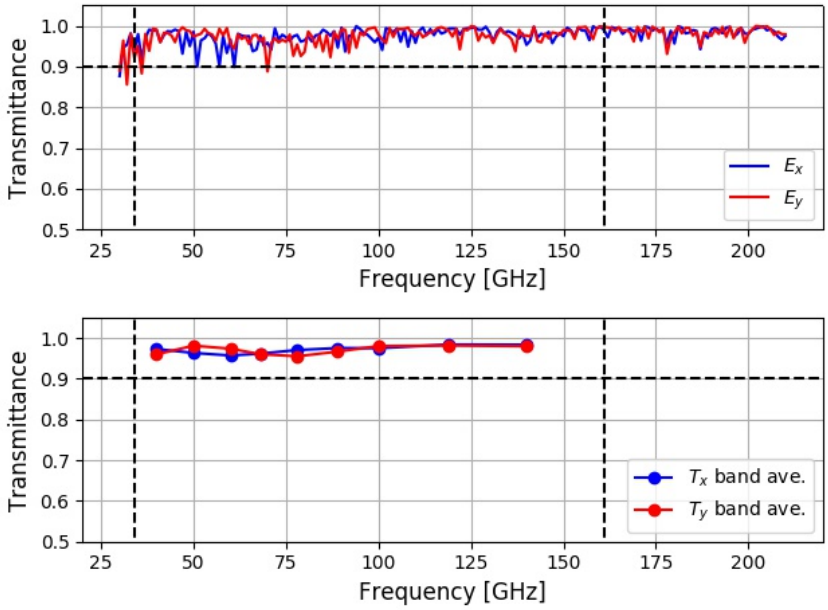

FIGURE 5.5: Transmittance calculation for 5-layer HWP with the structure of Takaku3 test4 on both sides.

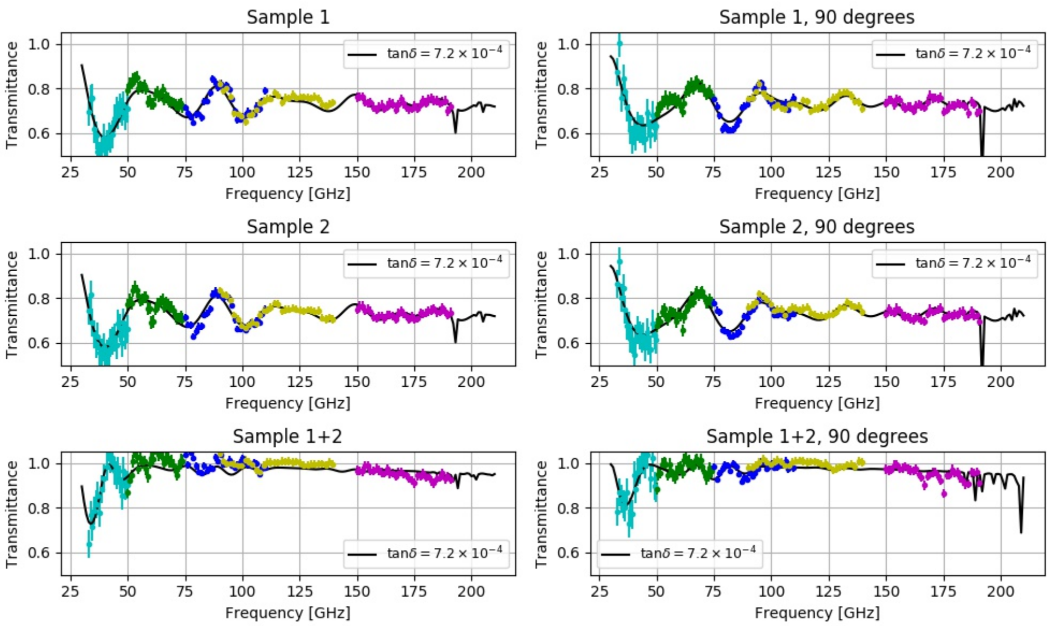

FIGURE 5.6: The transmittance measurement of each samples. Top two panels are the results of sample 1, and center two panels show the results of sample 2. Bottom two panels show the measurement of stacked sample 1 and 2 as if the stacked sample has the SWSs on both sides of the surface. We take the transmittance at two directions of the polarization, 0 and 90 degrees. Colored dots are measured data at each bands and black line is the predicted calculation based on measured shape by laser con-focal microscope with taking the loss term $\tan\delta = 7.2 \times 10^{-4}$. The data errors come from the RMS of (fit - data) by measuring the simple flat sapphire sample to estimate the systematic errors.

Chapter 6

Discussion

In this chapter, we discuss a few topics about the fabricated samples for LiteBIRD project. Our sample has extra loss tangent in particular to miniamster 8 and 9 and we try to improve this effect which is described in Sec. 6.1. The fabricated samples also have the anisotropy between x and y cross section. This causes the different refractive index profile and acts as a birefringent material. We discuss this effect in Sec. 6.2. We apply the SWS for the multi-ayer AHWP for broadband modulator. We can estimate the modulation efficiency about the multi-layer achromatic HWP with measured SWS by RCWA method which is described in Sec. 6.3. The material we used is only C-cut sapphire which is not a birefringent material. We apply our development it on the A-cut sapphire and to be identical material in a part of HWP and SWS. This is important to reduce the multiple reflection due to the different refractive index of C-cut sapphire and A-cut sapphire, and also to reduce the weight. We describe the difference about the machining between C-cut and A-cut sapphire, and development for the A-cut sapphire fabrication in Sec. 6.4. We also describe how to cover the large area in Sec. 6.5.

6.1 Discrepancy between measurement and prediction

The measurement of Minimaster 8 and 9 have the discrepancy with RCWA calculation even though we can measure the transmittance of ELAS sapphire 3. The reason of discrepancy may be the different color between ELAS sapphire 3 and Minimaster 8 and 9. We do not have the clear conclusion why Minimaster 8 and 9 have the brown color, there is something different material due to the interaction between laser and a material. Thus we tried cleaning the surface of the Minimaster 8. First, we put Minimaster 8 into the acethone, and did the ultrasonic cleaning in 1 hour and confirm what is the color and optical performance. Next we put Minimaster 8 into the hydrofluoric acid in 20 minutes two times. Then we also see the color and measure the transmittance. The measurement is only in G band because it is significant to see the improvement of the absorption effect to measure at only higher frequency band. The results are given in Fig. 6.1. The color by acethone ultrasonic cleaning sample does not change, and by hydrofuoric achid cleaning sample becomes a little darker. There is still discrepancy between measurements and calculation even if we clean the sample by not only acethone ultrasonic cleaning but also hydrofluoric acid cleaning. We cannot change the color from brown to white and also improve the optical performance. Next try is Annealing Minimaster 8 in 1500 degrees for 30 minutes in order to delete the lattice defect. Then the sample color becomes black. And there is no method to grind the surface directly because the groove width is under 0.3 mm. Our direction is that first we try to see the component analysis for the SWS surface and not colored surface, and to be clear the difference between two surface. Then we try to find the method to clean the particular component which affects the transmittance. Generally it is difficult to measure the component for tilted surface. To simply, thus we have made the ablated sample in order to be flat. However, the color of the surface is white. and not confirm the fignificant absorption effect. Therefore, we conclude that the extra absorption effect comes from the brown color and it changes during the SWS fabrication. Basically we cannot use the Minimaster laser machine for the large area sample, though it is the interesting study from the point of condensed matter physics and it is under investigation.

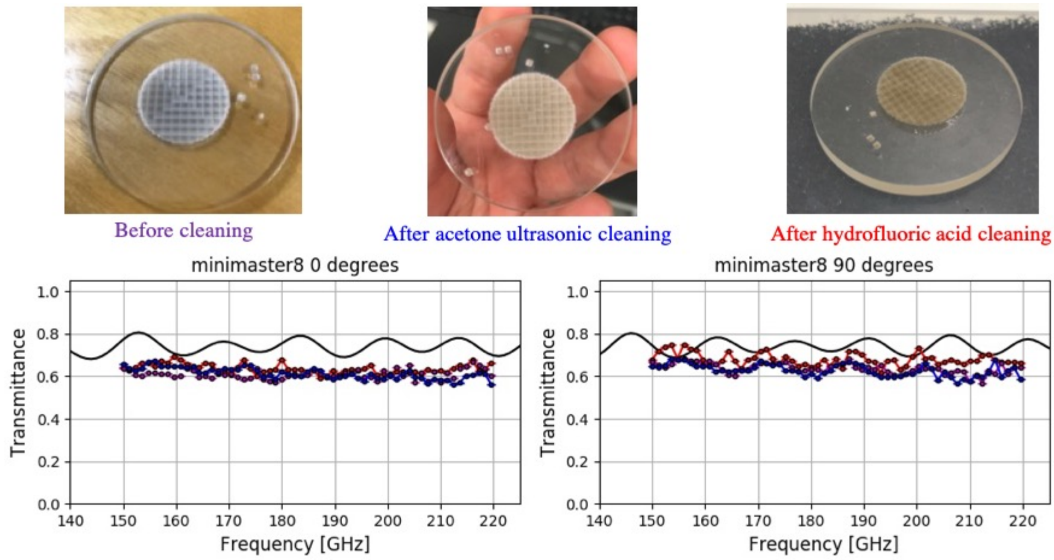

FIGURE 6.1: Transmittance measurement of Minimaster 8 with pictures of each process of cleaning. Magenta color shows the transmittance before cleaning, blue color shows the transmittance after athetone ultrasonic cleaning, and red color shows the transmittance after hydrofluoric acid cleaning. Black line shows the predicted value calculated by RCWA method.

6.2 Anisotropy of structure

Fig. 6.2 shows the instrumental polarization of Pharos 8 and 9 which is defined as

$$IP = \frac{T_x - T_y}{T_x + T_y}. \tag{6.1}$$

It characterizes the polarization properties of the samples and represents the level of conversion of unpolarized to polarized light by an instrument or one of its components [34]. Blue dots are come from the measurements, and red curve shows the calculation based on measured shape with $\tan\delta = 7.2 \times 10^{-4}$. In the bottom panel of Fig. 6.2, IP reaches 10% at 39 GHz. Basically the IP becomes 0 for the symmetric structure.

However Pharos 8 and 9 have different taper in x and y directions, which results different n_{eff} profile between x and y as shown in Fig. 4.8. This difference causes the instrumental polarization as shown in Fig. 6.2 and affects CMB polarization observation adversely as a 2f effect. We use rotational Achromatic HWP to modulate CMB, which signal is modulated to 4f, where f is the rotational frequency. The source of 2f in the time domain might be atmosphere in ground telescope, and CMB itself in balloon and space telescopes. Then, 2f peak leaks to 4f as a multiple frequency.

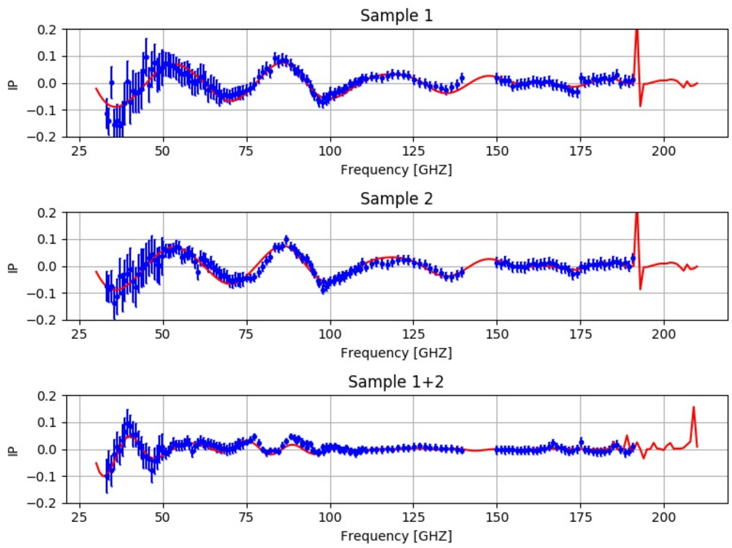

FIGURE 6.2: IP for each sample and stacked sample. Red line is the calculation based on measured shape with $\tan\delta = 7.2 \times 10^{-4}$.

Moreover, even if $2f$ might be able to filter out by demodulation, it can excite the detector too high and it runs to the non-linear regime. We should avoid this effect as much as possible. Fig. 6.3 shows the transmittance measurement of the stacking sample at 90 GHz with rotating the stacking sample. There are 2 cases; the result for stacking two samples parallel to their x axis at left panel while perpendicular to their x at right panel. The transmittance for left panel oscillates between 0.83 and 1.0 in one rotation, while such oscillation is vanished in the test 2. Fig. 6.4 also shows the Fourier transform of sample data for test 1 and 2. Clearly multiple frequency of test 2 is smaller than test1. This is the significant reduction of IP in CMB polarization experiments.

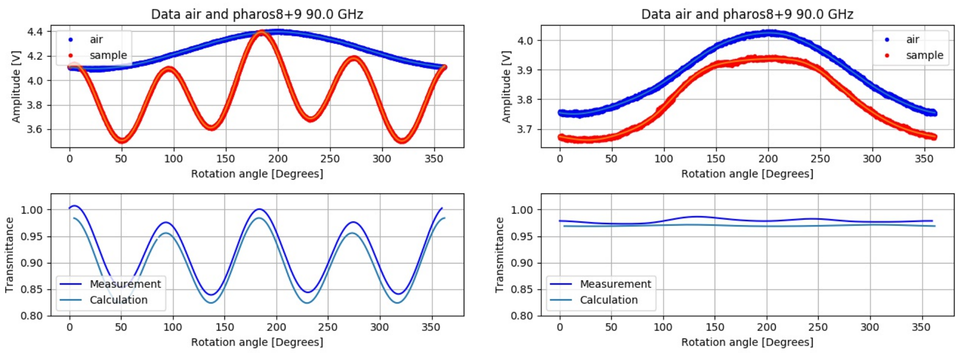

FIGURE 6.3: Transmittance of stacking sample as a function of the rotation angle at 90 GHz with parallel to their x axis at left panel while perpendicular to their x at right panel. The transmittance is calculated by taking the ratio of fittings for the amplitude of air and sample. The reason we have to fit them is that the rotation angle is a little different between air and sample.

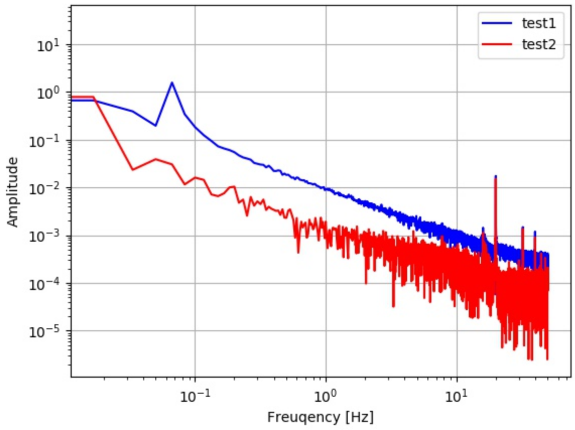

FIGURE 6.4: Fourier transform of sample data for test 1 and 2. The rotational frequency in these measurements is 1/60 Hz, the highest peak of blue spectrum is the signal of $4f$.

6.3 Modulation efficiency

6.3.1 Single and multi-layer AHWP with SWS

Several CMB polarization experiments use the rotational AHWP at a cryogenic temperature in order to reduce the systematic noise. If we take the fabricated SWS on both sides of AHWP, we can achieve high transmittance with high modulation efficiency at broadband frequency. Figure 6.5 shows the transmittance and modulation efficiency for 1, 3 and 5 layer AHWP calculated by RCWA method. The detail calculation for this plot is shown in Appendix. Each HWP has the thickness of 4.75 mm, which is to fix the center frequency of 100 GHz from $\nu = c/(2d|n_o - n_e|)$. The optic axis of center HWP in 3 layers is 50.6 degrees relative to other HWPs. The refractive index of material is set as $(n_o, n_e) = (n_x, n_y) = (3.047, 3.361)$, and $\tan\delta = 5.0 \times 10^{-5}$, which is the value at the cryogenic temperature. The optic axis of HWPs in 5 layers is shown in Tab. 6.1. The transmittance is similar in 1, 3 and 5 layers, while there is the multiple reflection at the stacking layers about 3 and 5 layers. With respect to the modulation efficiency, it rapidly drops down from the center frequency about 1 layer, while we can achieve high modulation efficiency at broadband frequency by 3 and 5 layer AHWP.

TABLE 6.1: The angle of optic axis and the thickness of each HWP.

Layer number	Optic Axis [Degrees]
1	157.339
2	47.09
3	0
4	-47.09
5	-157.339

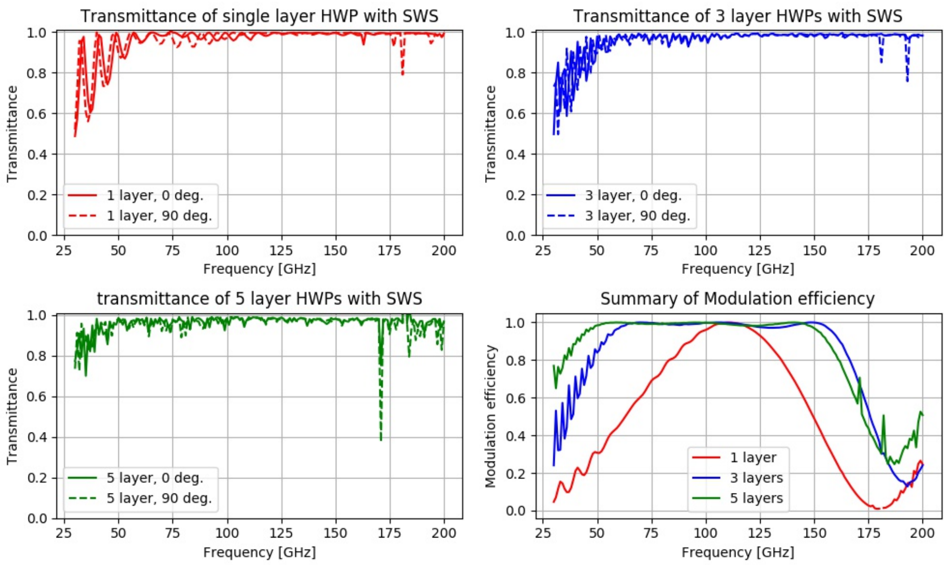

FIGURE 6.5: Transmittance and modulation efficiency calculation for 1, 3 and 5 layer AHWP with the shape of Pharos 9 on both sides. The thickness of AHWP is set as 4.75 mm. The refractive index of material is set as $(n_o, n_e) = (n_x, n_y) = (3.047, 3.361)$, and $\tan\delta = 5.0 \times 10^{-5}$.

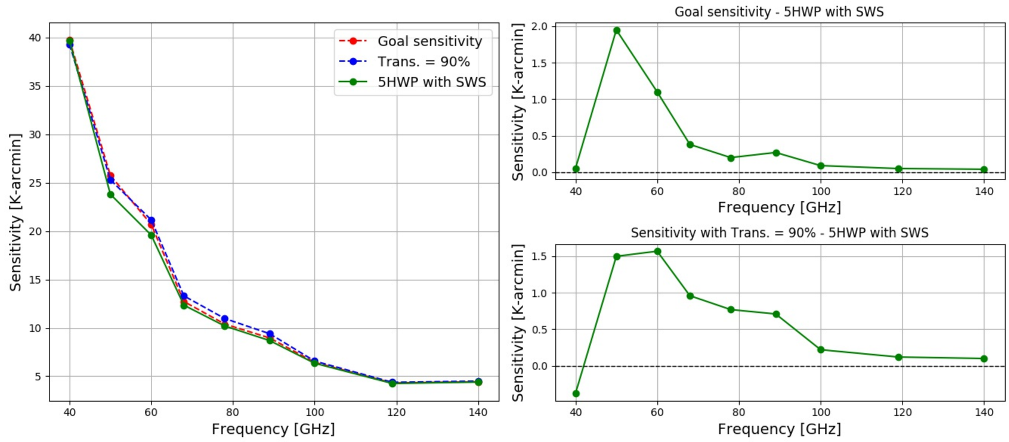

FIGURE 6.6: Left panel includes the tentative goal sensitivity (a), sensitivity calculated with transmittance of 90% in all frequency bands (b), and the sensitivity calculated for 5 layer AHWP with the shape of Pharos 9 on both sides (c). Upper right panel shows the difference between (a) and (c), and bottom right panel shows the difference between (b) and (c).

6.3.2 Sensitivity calculation for 5 layer HWP

Fig. 6.6 shows the sensitivity calculation for 5 layer AHWP with the shape of Pharos 9 on both sides [27]. We compare the calculation with the goal sensitivity [6] and the sensitivity with transmittance of 90% in all frequency bands, which is the boarder line in this thesis. The comparison with the sensitivity with transmittance of 90% shows that we can achieve higher sensitivity than one with transmittance of 90% except the lowest frequency band. The comparison with the reference [6] shows that we achieve the higher transmittance than the reference in all frequency bands. Since this is the prospective performance at the cryogenic temperature, we have to test the transmittance and modulation efficiency by our experiments.

6.4 A cut sapphire fabrication

6.4.1 The dependence of optic axis

We apply our development it on the A-cut sapphire and to be identical material in a part of HWP and SWS. This is important to reduce the multiple reflection due to the different refractive index of C-cut sapphire and A-cut sapphire, and also to reduce the weight. In the case of A-cut sapphire, we have to consider the dependence of the ablation rate on the optic axis. The machining parameter is fixed for each 13 grooves, however the groove depth becomes small around 90 degrees. One of the reason is that there is large difference of refractive index between ordinary and extra ordinary ray, thus the absorption rate at ordinary is larger than one at the extra ordinary. We have to consider that dependence for the fabrication. Fig. 6.7 shows the cross section of 1 dimension averaged groove and its depth as a function of the optic axis.

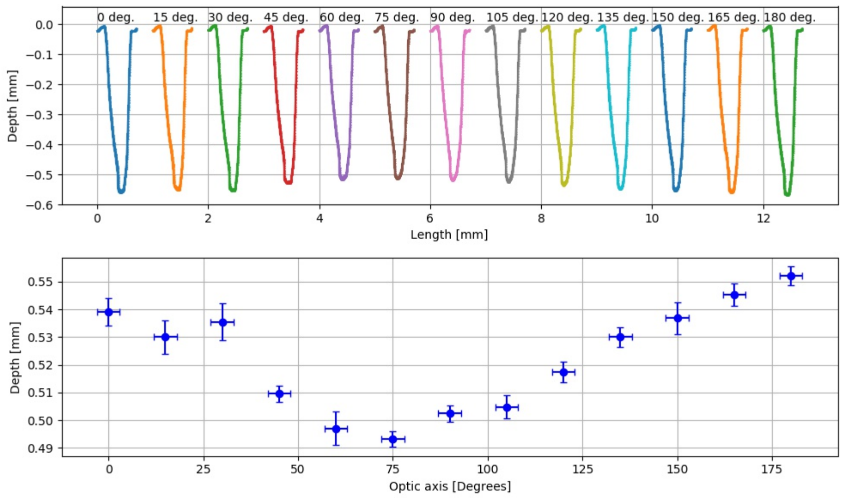

FIGURE 6.7: Cross section of 1 dimension V groove and the depth as a function of the optic axis.

6.4.2 Structure fabrication on A cut sapphire

The other things of the difficulty to machine SWS on A-cu sapphire is that A-cut sapphire is very fragile compared with C-cut sapphire. Fig. 6.8 shows the fabricated sample on A cut sapphire here in after called Pharos 11 by using the scan strategy as same as one for Pharos8 and 9. It can be expected to fabricate over 2 mm structures, however the measured height does not reach the 2.0 mm. The top of almost all of structures in the diameter of 34.5 mm may be broken at the first a few repeating number, thus the measured height decreases to 1.89 mm. Roughly, 20% of structures are broken from the middle, thus the fitting parameter σ becomes larger than Pharos8 and 9. A few percent of structures are completely broken, which number is 19. Although there are many cracks on Pharos 11, we can measure the transmittance because the fabricated area is 34.5 mm which is enough to measure. Fig. 6.9 shows the transmittance measurement of Pharos 11 at F band and the calculation based on RCWA. The measurement is generally agreement with the calculation. The discrepancy around 120 GHz with the polarization of 90 degrees can be the non-uniformity of the structure.

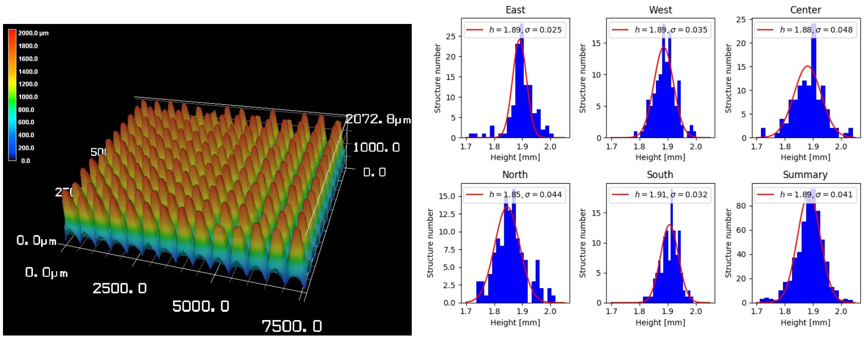

FIGURE 6.8: Image of the fabricated structures on an A cut sapphire and the histogram of its height taken in 5 location. The red curve in right panel shows the fitting by Gauss function. Bottom right panel in the subplots shows the result with summarizing the height at all location and its Gaussian fitting.

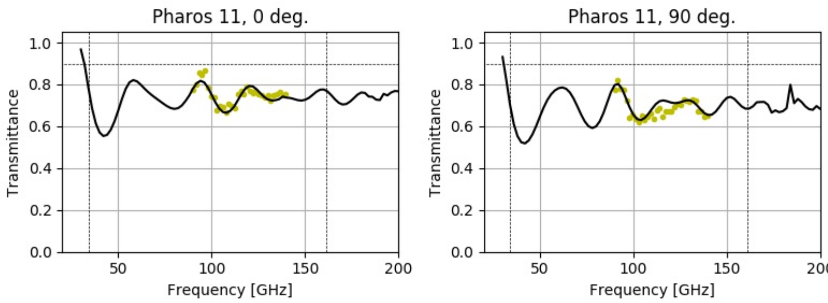

FIGURE 6.9: The transmittance measurement of Pharos 11 and prediction by RCWA.

6.4.3 Scan strategy for A cut sapphire

We have to avoid the crack issue in particular for the A cut sapphire as much as possible. Then we have developed the new scan strategy which is useful for this problem. The outline of the new scan strategy is depicted in Fig. 6.10. Basically we use line scan strategy, and the difference is the scan direction in the Line width ℓ_w. In order to make a vertical groove, we scan the laser along the horizontal short lines. While to make a horizontal groove, we scan the laser along the vertical short lines. Then the inter space between horizontal lines or vertical lines are moving the laser position with the power off. There is the laser on/ off delay of 50¯s and the averaged power at the edge becomes lower than that at the center of groove. Thus, We can avoid the crack issue and make the structure as shown the right side of Fig. 6.10.

6.5 Stitching

There are two ways to scan the laser, to move the sample itself by using xy stage, and to change laser orbit by galvano mirrors with $f\theta$ lens. The first way enable us to scan large area in once limited by the range the xy stage itself. However it is much slower scanning of $1 \sim 100$ mm/s, it is low ablation rate. Furthermore, We have to move very heavy sample, the accuracy of position should be unstable. The galvano mirror scanning with $f\theta$ lens can move laser orbit very faster than xy stage, 12 m/s. However it restricts the working range at once by the size of $f\theta$ lens in 70

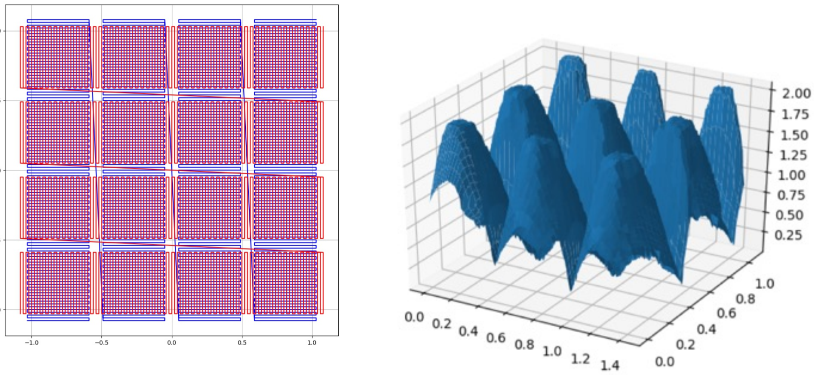

FIGURE 6.10: The outline of the new scan strategy for A cut sapphire fabrication for solving crack issue.

mm diameter. Thus we combine both way in order to cover the large area over a diameter of 450 mm. We define one unit which range is within the size of $f\theta$ lens, and complete the fabrication in one unit. Then we move the sample to the next position by xy-stage, and repeat the machining. Fig. 6.11 shows the alumina sample fabricated in the 47.5 mm diameter. The height of this sample is under 1.0 mm with the pitch of 0.33 mm. It is tiled one unit of 2.64 mm $\times$ 2.64 mm and there are walls between units. This is called as stitching line, and it affects the periodical diffraction for the transmittance measurement.

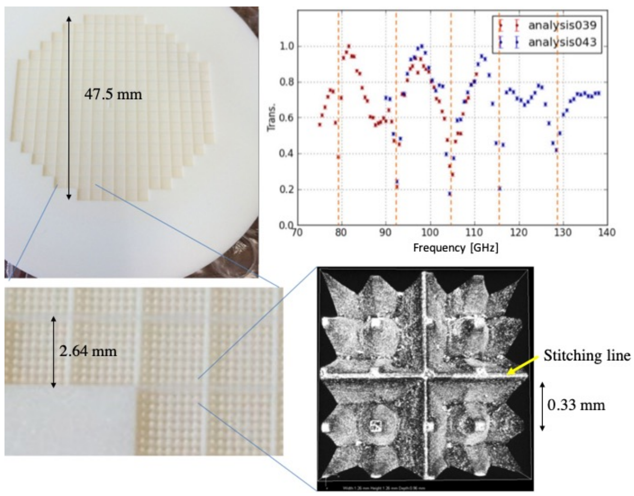

FIGURE 6.11: The large area fabrication sample on Alumina with the height of under 1.0 mm and the pitch of 0.33 mm. One unit is 2.64 mm $\times$ 2.64 mm and tile it Octagon with in the 47.5 mm. Upper right panel shows the transmittance measurement of this sample.

Upper right panel in Fig. 6.11 shows the transmittance measurement of the sample. Orange dashed line shows the location where the data has the lower spikes. This is caused by the diffraction that assume the unit as a periodical structure. Therefore, we have to delete this stitching line in order to delete such a stitching line. We have develop the method to delete the stitching line completely, and here we introduce how to delete it.

We define the extra parameter stitching line width (ℓ_{SL}) as shown in Fig. 6.12. The stitching line length ℓ_{SL} is the extra length for one unit. By overlapping this area next to the unit, we can delete the stitching line. Then the line length ℓ_l should be fixed as follow: Tab. 6.2 shows the parameters settings for a stitching sample. The initial stitching line length is set as 0.072 mm, which corresponds to the initial opt width w_0. After repeating 5 numbers, we reduce the line space without changing the line number, which is as same as our new line scan strategy. With reducing the line width, the stitching line length should increase in order to keep the same line length.

$$\ell_l = \ell_w \times (\text{Structure number} + 1) + \text{Structure number} + \ell_{SL} \times 2. \tag{6.2}$$

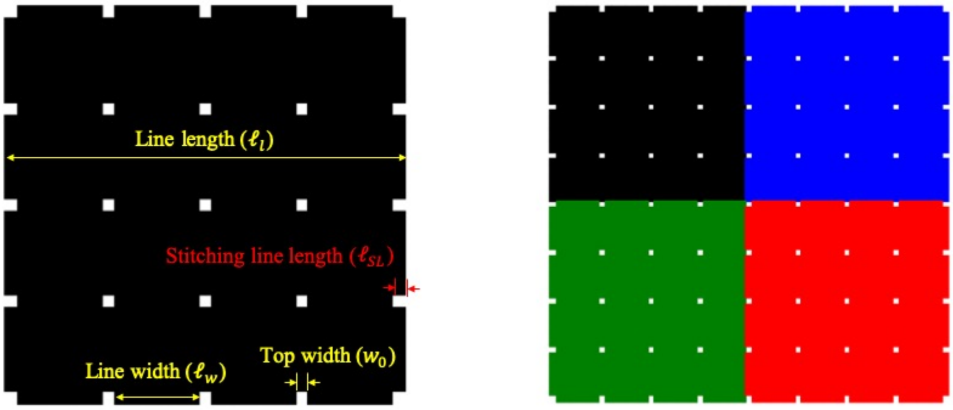

FIGURE 6.12: Definition of Stitching line length and outline of the stitching method.

Number	ℓ_s [mm]	ℓ_w [mm]	w_0 [mm]	Stitching line length ℓ_{SL} [mm]
5	0.009	0.468	0.072	0.072
10	0.008	0.416	0.124	0.098
10	0.007	0.364	0.176	0.124
10	0.006	0.312	0.228	0.15
10	0.005	0.26	0.28	0.176
10	0.004	0.208	0.332	0.202
10	0.003	0.156	0.384	0.228

TABLE 6.2: Parameter settings for a stitching.

This is only the parameters to fabricate in the unit, then we describe two stitching method. One is that we finish 65 repeating in one unit, then we move the sample by xy stage. And we continue to finish the next unit 65 times. The other is that if we finish one parameter set in case of the first time that is 5 times, then we move the sample by xy stage, and repeat the same time. When we finish all machined area in a 5 times, we return the first fabricated unit position, and then continue the next parameter set in all area. The difference between the two methods is whether to finish the processing in one unit first, or to process the whole little by little. Fig. 6.13 shows the image of crossed stitching line compared by two stitching method. The left panel is the first method, and right panel is the later method. The result in the first method cannot delete the stitching line, while the later method vanishes the stitching line completely. The reason why there is still the stitching line in the first method is that if we finish the scanning in the unit first, there is the large taper along the side of the unit which length is beyond the overlapping. As a result, We can delete the stitching line completely by using the later stitching method.

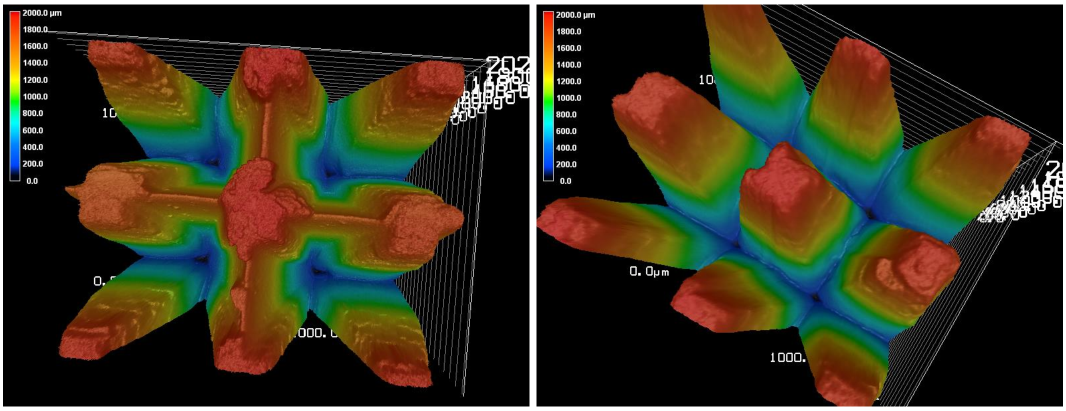

FIGURE 6.13: 3D image at the stitching point. left panel shows the first method, and right panel shows the later method.

Chapter 7

Future works

In this chapter, we describe the next progress for this study. We update the laser machining system for large area fabrication in more practical time. This is for LiteBIRD breadboad model (BBM) which is the model to confirm the feasibility of the design in development with new technology elements. The recent laser machining setup is described in Sec. 7.1, and the results of the fabricated samples are summarized in Sec. 7.2.

7.1 Large area laser machining

7.1.1 Design of sample holder

We have developed the strategy to make over 2 mm structure with the practical time, and to cover large area with deleting the stitching line. For the future works, we design the sample holder as shown in Fig. 7.1. Since we have 2 linear stages (OSMS33-500(X), Sigma) and the z stage (ZA-16A-32F, Kohzu), we stack them like a tower. Then what we have to consider is a parallelism, a repeatability, and a load capacity. These specifications are summarized in Tab. 7.1.

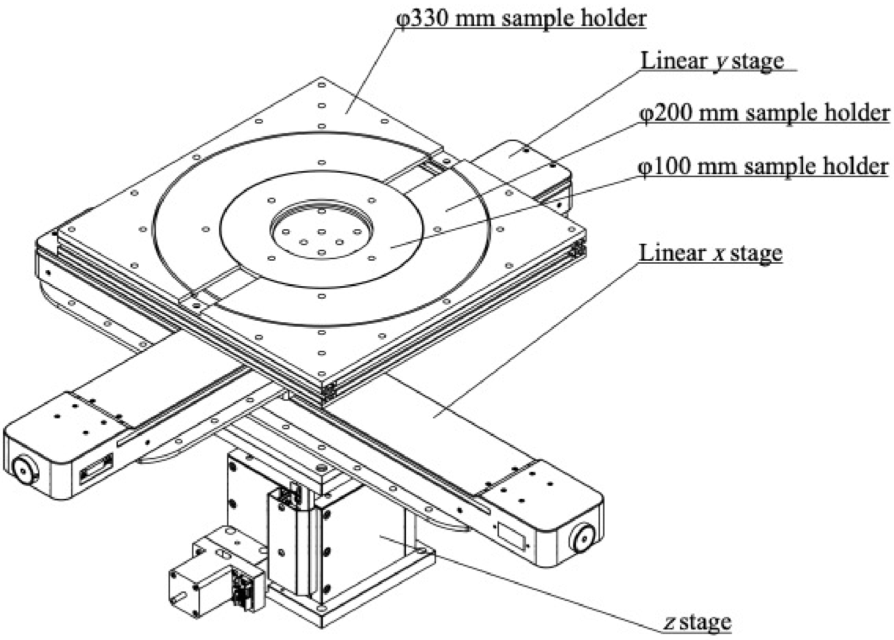

FIGURE 7.1: The design of sample holder with 2 linear stages and z stage.

TABLE 7.1: Specification of each component

		z stage	x stage	y stage	Sample holder	Sapphire
Weight [kg]	a	14.5	8.6	8.6	3.97	2.38
Parallelism [μm]	b	8	50	50		
Repeatability [μm]	c	≤ 0.5	6	6		
Load capacity [kg]	d	50	20	20		
Weight above device [kg]	d	23.55	14.95	6.35	2.38	
d - e	f	26.45	5.05	13.65		

The mass of sapphire with a diameter of 330 mm and the thickness of 7.0 mm is 2.38 kg, which is calculated with the density of 3.97 g/cm^3 [41]. In Tab. 7.1, the load capacity for each stage is larger than the accumulated weight above each device. The parallelism is important to fabricate a large area, and the height of SWS does not change so much in 100 μm. The repeatability is the order of 1 μm, and we will test that this number is dominant for large area fabrication. The xy-stage can move 500 mm and cover a diameter of 330 mm which is the diameter of sapphire HWP in BBM. We also prepare the sample holder with a diameter of 100 mm and 200 mm as we are planning to make a sample fabricated in small area to test the laser system.

7.1.2 Specification of large area fabrication setup

We combine the sample holder with the new high pwoer laser to make laser machining setup. The assembled picture is shown in Fig. 7.2. We use higher power than Pharos, named Carbide, which specification is shown in Tab. 7.2. The averaged power reaches to 40W and we can change the pulse duration fom 4 ps to 307 fs. The repetition rate is 100 kHz, which is 1.3 times larger than Pharos. We use the galvano mirror which was used with Pharos and put it at top of the setup. For the safety we surround the machining stage by Anodized aluminium plate. In order to see the inside of the box, we put the inside camera and inside light and thus we can check the location of the machining and monitor the machining process.

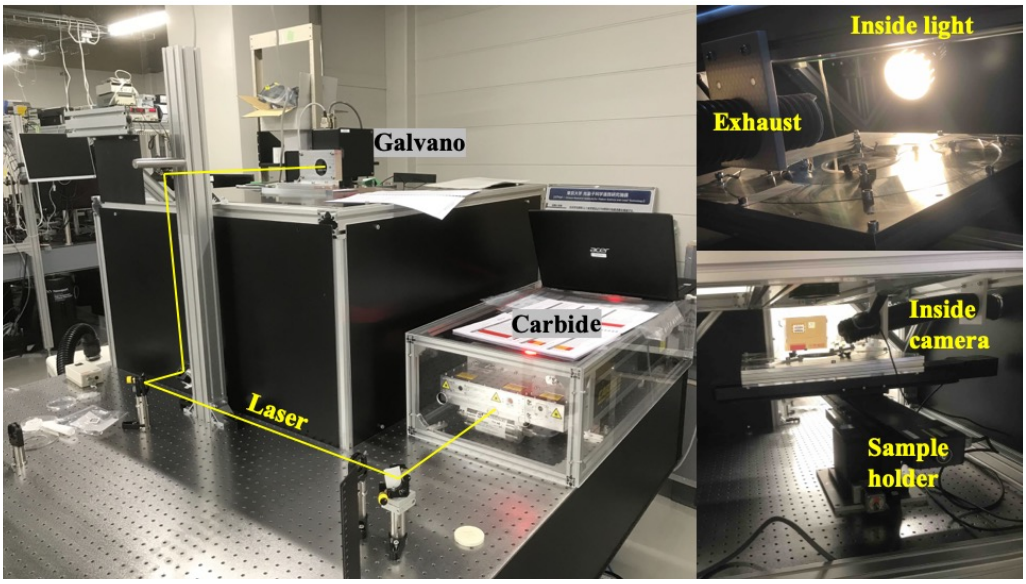

FIGURE 7.2: Picture of the recent machining setup for large area fabrication.

Parameters	value
Wavelength	1028 nm
Pulse duration	307 fs $\sim$ 4 ps
Averaged power	40 W
Repetition rate	100 kHz
Pulse energy	400 μJ
Peak power	1.3 GW
Spot size	38.4 μm
Rayleigh length	4.63 mm
$f\theta$ lens working range	d = 70 mm
xy stage range	500 mm

TABLE 7.2: Specification of Carbide laser fabrication system.

7.2 Results from Carbide system

Fig. 7.3 shows the SWS sample on C-cut sapphire and A-cut sapphire by Carbide system. The fabricated diameter is 70 mm. Each sample is named as Carbide 3 (A-cut) and Carbide 4 (C-cut). Since they are made by the same scan strategy, the fabricated results should be similar even if there is the difference about the axis cut. Fig. 7.4 shows the histogram of measured height at 5 locations as same as pharos 11 and Gaussian fitting. The measured height of Carbide 3 and 4 has the averaged height of 1.88 ± 0.027mm and 1.91 ± 0.013mm respectively. The targeted height of them is 1.9 mm, thus we can make the designed shape. However, we find that there are broken structure at the tops, and 17 completely broken structures on Carbide 4, which is A cut sapphire. Thus there is larger σ in A cut result compared with C-cut. Fig. 7.5 shows the transmittance measurement of Carbide 3 and 4. The measurement is in good agreement with the calculation. The large area fabricated sample has similar optical performace as Pharos 8 and 9. Fig. 7.6 shows the summary of the prospective processing time which is calculated by Eq. 4.4. The fabricated time for Carbide 3 and 4 is 13.49 hours, thus the prospective processing time becomes 23 days. This is 1.9 mm structure which is under our designed structure height. If we repeats the scan number more time, we can make deeper structure than 2.0 mm, nevertheless the prospective processing time is under 1 month. We continue to optimize the scan parameter and make the sample with over the diameter of 450 mm.

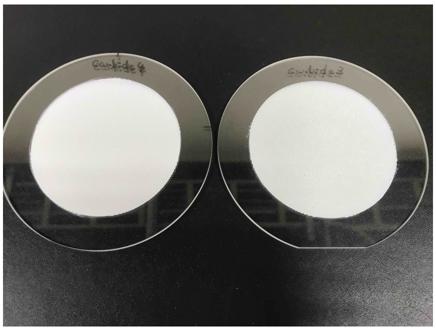

FIGURE 7.3: The image of two fabricated samples made by Carbide system. Right sample is C-cut sapphire (Carbide 3) while left sample is A-cut sapphire (Carbide 4). These sample are fabricated by same scan strategy.

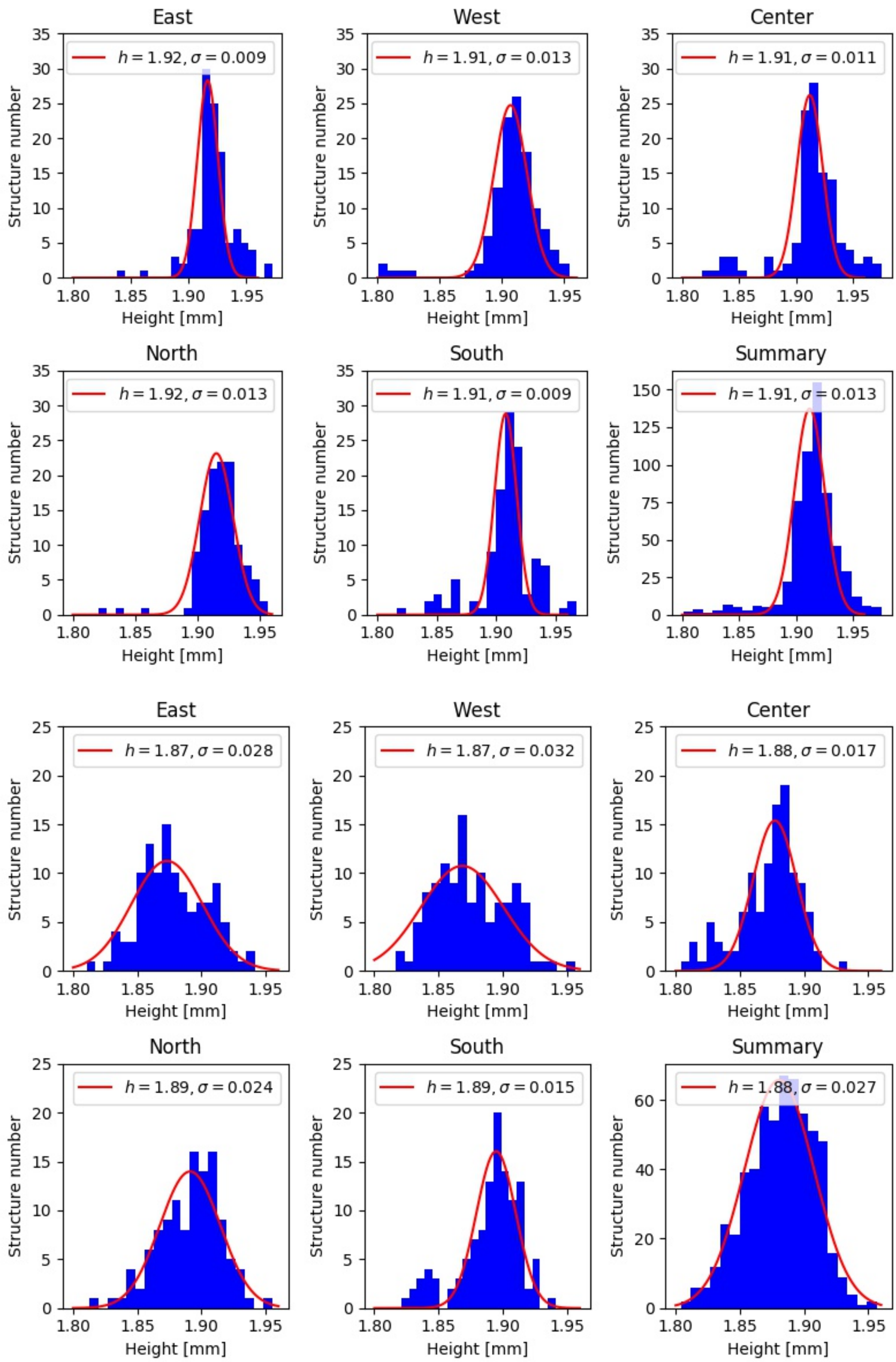

FIGURE 7.4: The histogram of measured height for Carbide 3 (Upper 6 panels) and Carbide 4 (Bottom 6 panels).

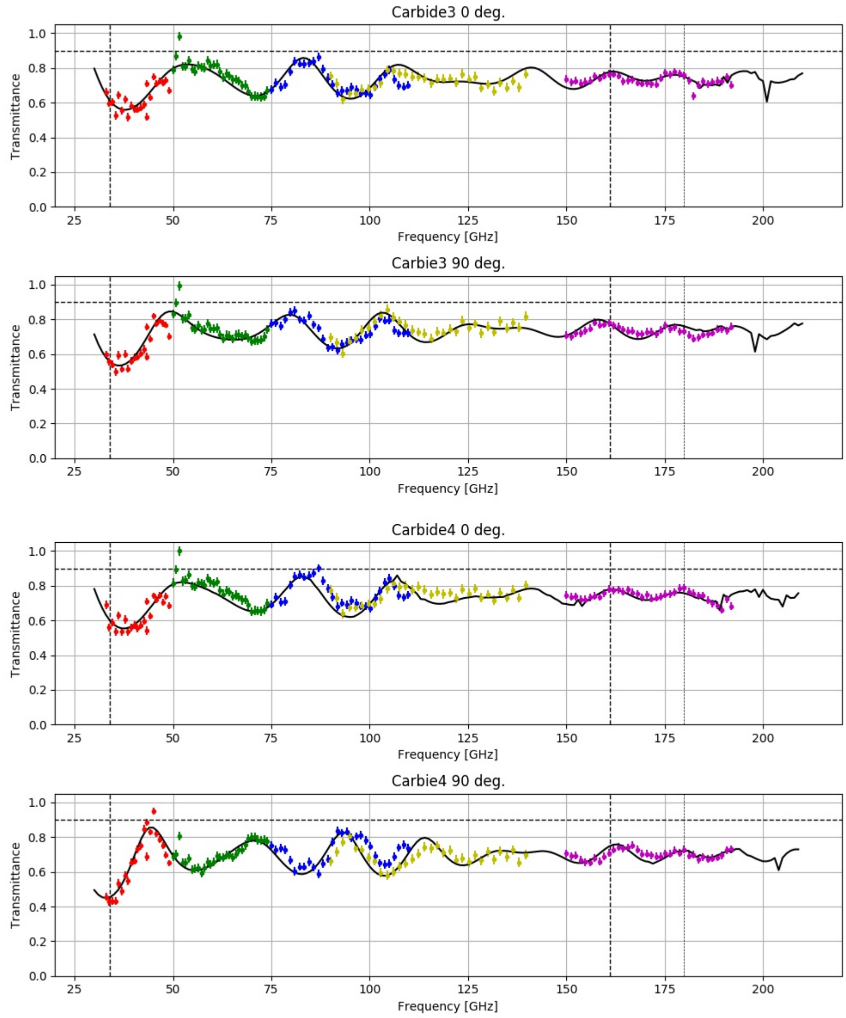

FIGURE 7.5: Transmittance measurement of Carbide 3 and 4.

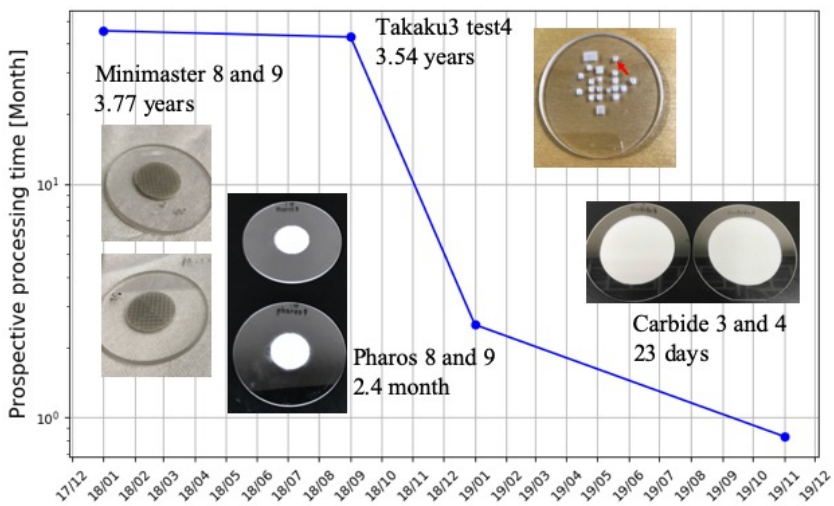

FIGURE 7.6: Summary of the prospective processing time calculated by Eq. 4.4.

Chapter 8

Conclusion

8.1 Design of SWS

We use Regorous coupled wave analysis(RCWA) to calculate the transmittance about the various pyramidal structure array for low frequency telescope(LFT) in LiteBIRD. We add the curvature α to optimize the structure as a broadband AR and discover the shape is important for wider coverage. The curvature α larger than 1.0 is better than under 1.0.

We study the optimal shape of wub-wavelength structures (SWS) as a broadband anti-reflection for LiteBIRD LFT by regorous couple wave analysis. We add the parameter of SWS named curvature α, and discover that the bell shape which means $\alpha > 1.0$ can cover the broader frequency bands.

8.2 Fabrication of SWS

We used 3W nano-second pulsed UV laser for testing the possibility to fabricate the structure with the height of 2.0 mm. Then we had a few problems that the previous scan strategy cannot make the structure with α > 1.0, the fabricated sample has the extra absorption by measuring the transmittance, and the prospective processing time is about 4 years to cover over a diameter of 450 mm. We update the laser machine to 15 W femto-second pulsed IR laser, and improve the scan strategy in order to make the structure with α > 1.0 with shorter processing time. The new scan strategy also enables us to avoid the crack issue which is caused by the high power pulse. The fabricated sample has the curvature with $\alpha \simeq 1.5$ and the processing time of 10.5 hours to cover over a diameter of 34.5 mm, which expects that it takes 2.4 month to cover over a diamter of 450 mm. This drastically reduces the processing time.

8.3 Optical performance of fabricated SWS

The fabricated sample by 15W femto-second pulsed IR laser has the transmittance over 90% between 40 and 161 GHz and which is almost consistent with the calculation based on RCWA method. Even though we do not understand completely the extra absorption effect for the samples, we achieve to make the sample which can cover the LFT band.

8.4 Discussions

The samples made by Minimaster has the higher extra absorption effect than the samples made by Pharos at higher frequency. Even though we tried cleaning the surface of SWS by acetone ultra-sonic cleaning and hdrofluoric acid cleaning, the transmittance did not improve. This reason is under investigating.

We have developed the scan strategy for A-cut sapphire, which is more fragile than C-cut sapphire. We have also developed the method to stitch the fabrication unit without any walls between units. Currently we fabricated SWS using stitching method in a small area, we can extend a large area with xy linear stages. Therefore, we have updated the laser (Carbide) and the sample stage for the large area fabrication with more practical time. We will make the SWS sample on A-cut sapphire over a diameter of 330 mm as a BBM for the next step.

8.5 Summary

We have been developing the broadband anti-reflective SWS on sapphire to cover the frequency band between 34 and 161 GHz for LFT in LiteBIRD. We have discovered by the simulation based on RCWA method that the bell shape can cover the broader frequency band compared with pyramidal and Mt. Fuji shape. We have also developed the method to make such a bell shape on sapphire by using ultra-short laser ablation. The new method with ultra-short pulsed laser ablation enable us to fabricate SWS in a practical time, 11.5 hours over a diameter of 34.5 mm. We can expect that it will take about 2.5 months to cover over a diameter of 450 mm. The transmittance measurement of fabricated sample made by ultra-short pulsed laser machining is in good agreement with the prediction based on RCWA method. For the next step, we will try to make the SWS sample on A-cut sapphire over a diameter of 330 mm as a BBM by the Carbide system.

Bibliography

[1] M Kawasaki. Lecture note: Cosmology ii, 2018. http://www.icrr.u-tokyo.ac.jp/th/kawasaki/ICRR/Lecture_files/cosmology20180521.pdf.

[2] http://www.astro.ucla.edu/~wright/cosmo_01.htm.

[3] https://lambda.gsfc.nasa.gov/product/cobe/.

[4] Planck Collaboration and Y. Akrami et al. Planck 2018 results. i. overview and the cosmological legacy of planck, 2018.

[5] E. Komatsu. *Cosmic Microwave Background radiation*. Nippon Hyoron sha co.,Ltd, 9 2019.

[6] H. Sugai et al. Updated design of the cmb polarization experiment satellite litebird. *Journal of Low Temperature Physics, in press.*

[7] H. Imada et al. The optical design and physical optics analysis of a cross-dragonian telescope for litebird. In Giovanni G. Fazio, Howard A. MacEwen, and Makenzie Lystrup, editors, *Space Telescopes and Instrumentation 2018*, volume 10698. SPIE, 1 2018.

[8] Y. Sakurai et al. Design and development of a polarization modulator unit based on a continuous rotating half-wave plate for LiteBIRD. In Jonas Zmuidzinas and Jian-Rong Gao, editors, *Millimeter, Submillimeter, and Far-Infrared Detectors and Instrumentation for Astronomy IX*, volume 10708, pages 28 – 39. International Society for Optics and Photonics, SPIE, 2018.

[9] S. A. Boden et al. *Moth-Eye Antireflective Structures*, pages 1467–1477. Springer Netherlands, Dordrecht, 2012.

[10] S. Dodelson and Academic Press (Londyn ; 1941-1969). *Modern Cosmology*. Elsevier Science, 2003.

[11] C. L. Bennett et al. NINE-YEARWILKINSON MICROWAVE ANISOTROPY PROBE(WMAP) OBSERVATIONS: FINAL MAPS AND RESULTS. *The Astrophysical Journal Supplement Series*, 208(2):20, sep 2013.

[12] A. Guth. Inflationary universe: A possible solution to the horizon and flatness problems. *Phys. Rev. D*, 23:347–356, Jan 1981.

[13] K. Sato. First-order phase transition of a vacuum and the expansion of the Universe. *Monthly Notices of the Royal Astronomical Society*, 195(3):467–479, 07 1981.

[14] M. Hazumi et al. Litebird: A satellite for the studies of b-mode polarization and inflation from cosmic background radiation detection. *Journal of Low Temperature Physics*, 194(5):443–452, Mar 2019.

[15] K. Ichiki. CMB foreground: A concise review. *Progress of Theoretical and Experimental Physics*, 2014(6), 06 2014. 06B109.

[16] Y. Sekimoto et al. Concept design of the LiteBIRD satellite for CMB B-mode polarization. In Makenzie Lystrup, Howard A. MacEwen, Giovanni G. Fazio, Natalie Batalha, Nicholas Siegler, and Edward C. Tong, editors, *Space Telescopes and Instrumentation 2018: Optical, Infrared, and Millimeter Wave*, volume 10698, pages 613 – 629. International Society for Optics and Photonics, SPIE, 2018.

[17] S. Kashima et al. Wide field-of-view crossed dragone optical system using anamorphic aspherical surfaces. *Appl. Opt.*, 57(15):4171–4179, May 2018.

[18] A. Kusaka et al. Modulation of cosmic microwave background polarization with a warm rapidly rotating half-wave plate on the atacama b-mode search instrument. *Review of Scientific Instruments*, 85(2):024501, 2014.

[19] S. Pancharatnam. Achromatic combinations of birefringent plates part i. an achromatic circular polarizer. *Indian Academy of Sciences*, 41:130–136, 1995.

[20] G. Savini et al. Achromatic half-wave plate for submillimeter instruments in cosmic microwave background astronomy: modeling and simulation. *Appl. Opt.*, 45(35):8907–8915, Dec 2006.

[21] S. Hanany et al. Millimeter-wave achromatic half-wave plate. *Appl. Opt.*, 44(22):4666–4670, Aug 2005.

[22] T. Essinger. Transfer matrix for treating stratified media including birefringent crystals: erratum. *Appl. Opt.*, 53(19):4264–4265, Jul 2014.

[23] K. Komatsu et al. Demonstration of the broadband half-wave plate using the nine-layer sapphire for the cosmic microwave background polarization experiment. *Journal of Astronomical Telescopes, Instruments, and Systems*, 5(4):1 – 14, 2019.

[24] B. R. Johnson. Maxipol: A bolometric, balloon-borne experiment for measuring the polarization anisotropy of the cosmic microwave background radiation. *a Thesis Submitted to the Faculty of the Graduate School of the University of Minnesota*, 2004.

[25] J. W. Lamb. Miscellaneous data on materials for millimetre and submillimetre optics. *International Journal of Infrared and Millimeter Waves*, 12 1996.

[26] https://trc.nist.gov/cryogenics/materials/materialproperties.htm.

[27] T. Hasebe. https://github.com/TakashiHasebe/LB_SensitivityCalculation/tree/master/SensitivityCalculationV28.0.

[28] http://www.keins.city.kawasaki.jp/content/ksw/4/5_film.pdf.

[29] https://www.enri.go.jp/research/sisetu/s_den.htm.

[30] H. Sakurai et al. Terahertz broadband anti-reflection moth-eye structures fabricated by femtosecond laser processing. *OSA Continuum*, 2(9):2764–2772, Sep 2019.

[31] R. Datta et al. Large-aperture wide-bandwidth antireflection-coated silicon lenses for millimeter wavelengths. *Appl. Opt.*, 52(36):8747–8758, Dec 2013.

[32] T. Wada et al. Mono-material multilayer interference optical filter with sub-wavelength structure for infrared and terahertz optics. *Applied Physics Express*, 3(10):102503, oct 2010.

[33] V. Schütz. Laser processing of sub-wavelength structures on sapphire and alumina for millimeter wavelength broadband anti-reflection coatings. 11:204–209, 01 2016.

[34] K. Young et al. Broadband millimeter-wave anti-reflection coatings on silicon using pyramidal sub-wavelength structures. *Journal of Applied Physics*, 121(21), 6 2017.

[35] T. Matsumura et al. Millimeter-wave broadband antireflection coatings using laser ablation of subwavelength structures. *Appl. Opt.*, 55(13):3502–3509, May 2016.

[36] R. W. Klopfenstein. A transmission line taper of improved design. *Proceedings of the IRE*, 44(1):31–35, Jan 1956.

[37] R. Bräuer et al. Design of antireflection gratings with approximate and rigorous methods. *Appl. Opt.*, 33(34):7875–7882, Dec 1994.

[38] M. G. moharam et al. Formulation for stable and efficient implementation of the rigorous coupled-wave analysis of binary gratings. *J. Opt. Soc. Am. A*, 12(5):1068–1076, May 1995.

[39] Rsoft. *DiffractMOD user guide*. Synopsys, Ossining NY 10562 USA, 2018.

[40] T. Matsumura et al. Millimeter-wave broadband antireflection coatings using laser ablation of subwavelength structures. *Appl. Opt.*, 55(13):3502–3509, May 2016.

[41] https://global.kyocera.com/prdct/fc/product/pdf/material.pdf.

Appendix A

Multi-layer thin thick coating

we can calculate the transmittance and reflection for the multi-layered thin thick coating by the boundary condition of the Maxwell's equation. Fig.3.1 shows the definition of the parameters. We define the vector of wave number parallel to xz-plane. There are N-layer thin thick coating of permittivitive material in $Z > 0$. We define the i-th thickness and index as d_i, n_i.

We can calculate the i-th angle by Snell's law,

$$n_i \sin\theta_i = n_{i+1} \sin\theta_{i+1} \tag{A.1}$$

There are two types of polarization, s-polarization and p-polarization.

In case of s-polarization, we can write the electric field as

$$E_{iy}(\mathbf{r}) = E_+ \mathrm{e}^{i\mathbf{k}_+\cdot\mathbf{r}} + E_- \mathrm{e}^{i\mathbf{k}_-\cdot\mathbf{r}} \tag{A.2}$$

where

$$\mathbf{k_{i+}} = (k_x, 0, k_{iz}) \tag{A.3}$$
$$\mathbf{k_{i-}} = (k_x, 0, -k_{iz}) \tag{A.4}$$
$$k_x = n_0 k_0 \cos\theta_0 \tag{A.5}$$
$$k_{iz} = n_i k_0 \cos\theta_i \tag{A.6}$$
$$\mathbf{r} = (x, y, z - L_i) \tag{A.7}$$
$$L_i = \sum_{j=1}^{i-1} d_j \tag{A.8}$$

The first term of Eq. A.2 is the incident wave and second term is the relected wave. By the Maxwell's law

$$\nabla \times \mathbf{E} = -\mu \frac{\partial}{\partial t}\mathbf{H} \tag{A.9}$$

the x direction of magnetic wave in i-th layer is

$$H_{ix}(z) = \Gamma_i \left\{ -E_+ \mathrm{e}^{ik_{iz}(z_{Li})} + E_- \mathrm{e}^{ik_{iz}(z_{Li})} \right\} \mathrm{e}^{ik_x x} \tag{A.10}$$

where

$$\Gamma_i = \frac{k_{iz}}{\omega\mu_0} = \frac{n_i k_0 \cos\theta_i}{c k_0 \mu_0} = n_i \cos\theta_i \sqrt{\frac{\epsilon_0}{\mu_0}} \tag{A.11}$$

We substrate $z = L_i$ into Eq. A.2-A.10, they become

$$E_{iy}(0) = (E_+ + E_-)^{ik_x x} \tag{A.12}$$

$$H_{ix}(0) = -\Gamma_i(-E_+ + E_-)^{ik_x x} \tag{A.13}$$

From Eq. A.12-A.13, the keisuu E_+ and E_- become

$$E_+^{ik_x x} = \frac{1}{2}\left(E_{iy}(0) - \frac{1}{\Gamma_i}H_{ix}\right) \tag{A.14}$$

$$E_-^{ik_x x} = \frac{1}{2}\left(E_{iy}(0) + \frac{1}{\Gamma_i}H_{ix}\right) \tag{A.15}$$

We substrate Eq. A.15 into Eq. A.2 and A.10 and describe by the matrix,

$$\begin{pmatrix} E_{iy}(z) \\ H_{ix}(z) \end{pmatrix} = M_i' \begin{pmatrix} E_{iy}(0) \\ H_{ix}(0) \end{pmatrix} \tag{A.16}$$

where

$$M_i' = \begin{pmatrix} \frac{1}{2}(e^{ik_{iz}z} + e^{-ik_{iz}z}) & -\frac{i}{2\Gamma_i}(e^{ik_{iz}z} - e^{-ik_{iz}z}) \\ -\frac{\Gamma_i}{2}(e^{ik_{iz}z} - e^{-ik_{iz}z}) & \frac{1}{2}(e^{ik_{iz}z} + e^{-ik_{iz}z}). \end{pmatrix} \tag{A.17}$$

M_i' is called transfer matrix. When there is no absorption in the material, k_{iz} should be realistic number, then Eq. A.17 becomes

$$M_i' = \begin{pmatrix} \cos k_{iz}z & -\frac{i}{\Gamma_i}\sin k_{iz}z \\ -i\Gamma_i \sin k_{iz}z & \cos k_{iz}z \end{pmatrix} \tag{A.18}$$

The inverse matrix of M_i' is written as

$$M_i'^{-1} = M_i = \begin{pmatrix} \cos k_{iz}z & \frac{i}{\Gamma_i}\sin k_{iz}z \\ i\Gamma_i \sin k_{iz}z & \cos k_{iz}z \end{pmatrix} \tag{A.19}$$

then Eq. A.16 becomes

$$\begin{pmatrix} E_{iy}(0) \\ H_{ix}(0) \end{pmatrix} = M_i \begin{pmatrix} E_{sy}(z) \\ H_{sx}(z). \end{pmatrix} \tag{A.20}$$

In the boundary at each layer, the component of Eq. A.20 is conserved. Thus, the electromagnetic wave which propagates the multi-layer coatings is described as

$$\begin{pmatrix} E_{iy}(0) \\ H_{ix}(0) \end{pmatrix} = M \begin{pmatrix} E_{iy}(L) \\ H_{ix}(L) \end{pmatrix} \tag{A.21}$$

$$M = M_1 M_2 M_3 \ldots M_N = \prod_{i=0}^{N} M_i \tag{A.22}$$

From these equations, we can obtain the coefficient of reflectance r and transmittance t. The incident wave and the transmitted wave is written as

$$E_{0y}(z) = \left(e^{ik_{0z}z} + re^{-ik_{0z}z}\right) e^{k_{0z}x} \tag{A.23}$$

$$E_{sy}(z) = te^{ik_{0z}(z-L)} e^{ik_{0z}x} \tag{A.24}$$

By using Eq. A.9,

$$H_{0x}(z) = -\Gamma_0 \left(e^{ik_{0z}z} - re^{-ik_{0z}z}\right) e^{ik_{0z}x} \tag{A.25}$$

$$H_{sx}(z) = \Gamma_s te^{ik_{0z}(z-L)} e^{ik_{0z}x} \tag{A.26}$$

and

$$E_{0y}(0) = (1+r)e^{ik_{0z}x} \tag{A.27}$$

$$H_{0x}(0) = -\Gamma_0(1-r)e^{ik_{0z}x} \tag{A.28}$$

$$E_{sy}(L) = te^{ik_{0z}x} \tag{A.29}$$

$$E_{sx}(L) = -\Gamma_s te^{ik_{0z}x}. \tag{A.30}$$

Thus, Eq. A.22 becomes

$$\begin{pmatrix} 1 & -(M_{11} - \Gamma_s M_{12}) \\ \Gamma_0 & -(M_{21} - \Gamma_s M_{22}) \end{pmatrix} \begin{pmatrix} r \\ t \end{pmatrix} = \begin{pmatrix} -1 \\ \Gamma_0 \end{pmatrix} \tag{A.31}$$

If we assume

$$A = \begin{pmatrix} 1 & -(M_{11} - \Gamma_s M_{12}) \\ \Gamma_0 & -(M_{21} - \Gamma_s M_{22}), \end{pmatrix} \tag{A.32}$$

then we can obtain

$$A^{-1} = \frac{1}{B} \begin{pmatrix} -(M_{21} - \Gamma_s M_{22}) & (M_{11} - \Gamma_s M_{12}) \\ -\Gamma_0 & 1 \end{pmatrix} \tag{A.33}$$

$$B = \Gamma_0 M_{11} - \Gamma_0 \Gamma_s M_{12} - M_{21} + \Gamma s M_{22} \tag{A.34}$$

Thus, the coefficient of reflectance r and transmittance t is written as

$$r = \frac{\Gamma_0 M_{11} - \Gamma_0 \Gamma_s M_{12} + M_{21} - \Gamma s M_{22}}{\Gamma_0 M_{11} - \Gamma_0 \Gamma_s M_{12} - M_{21} + \Gamma s M_{22}} \tag{A.35}$$

$$t = \frac{2\Gamma_0}{\Gamma_0 M_{11} - \Gamma_0 \Gamma_s M_{12} - M_{21} + \Gamma s M_{22}} \tag{A.36}$$

The average in the time of z component of the poynting vector $\mathbf{S}$ is

$$S_z = E_x H_y^* - E_y H_x^* \tag{A.37}$$

For the s-polarization, $E_x = 0$. Thus, The incident , reflected and transmitted poynting vector is

$$S_{0z} = n_0 \cos\theta_0 \sqrt{\frac{\epsilon_0}{\mu_0}} \tag{A.38}$$

$$S_{rz} = -|r|^2 n_0 \cos\theta_0 \sqrt{\frac{\epsilon_0}{\mu_0}} \tag{A.39}$$

$$S_{tz} = |t|^2 n_s \cos\theta_s \sqrt{\frac{\epsilon_0}{\mu_0}} \tag{A.40}$$

and reflectance and transmittance becomes

$$R = \frac{|S_{rz}|}{S_{0z}} = |r|^2 \tag{A.41}$$

$$T = \frac{S_{tz}}{S_{0z}} = |t|^2 \frac{n_s \cos\theta_s}{n_0 \cos\theta_0} \tag{A.42}$$

In the case of p-polarization, the magnetic wave in i-th layer is written as

$$H_{iy}(\mathbf{r}) = H_+ \mathrm{e}^{i\mathbf{k}_+\cdot\mathbf{r}} + H_- \mathrm{e}^{i\mathbf{k}_-\cdot\mathbf{r}}. \tag{A.43}$$

By the Maxwell's equation

$$\nabla \times \mathbf{H} = \epsilon \frac{\partial}{\partial t}\mathbf{E}, \tag{A.44}$$

The x component of electric wave in i-th layer is

$$\Gamma_i E_{ix}(z) = \left(H_+ \mathrm{e}^{ik_{iz}z} - H_- \mathrm{e}^{ik_{iz}z}\right) \mathrm{e}^{ik_x x} \tag{A.45}$$

where

$$\Gamma = \frac{\omega\epsilon\epsilon_0}{k_{iz}} = \frac{ck_0 n_i^2 \epsilon_0}{n_i k_0 \cos\theta_i} = \frac{n_i}{\cos\theta_i}\sqrt{\frac{\epsilon_0}{\mu_0}}. \tag{A.46}$$

By substituting $z = L_i$ into Eq. A.43, A.46,

$$H_{iy}(0) = (H_+ + H_-)\mathrm{e}^{ik_x x} \tag{A.47}$$

$$\Gamma_i E_{ix}(0) = (H_+ - H_-)\mathrm{e}^{ik_x x} \tag{A.48}$$

From Eq. A.48, the coefficient of H_+ and H_- becomes

$$H_+ \mathrm{e}^{ik_x x} = \frac{1}{2}(H_{iy}(0) - \Gamma_i E_{ix}(0)) \tag{A.49}$$

$$H_- \mathrm{e}^{ik_x x} = \frac{1}{2}(H_{iy}(0) + \Gamma_i E_{ix}(0)) \tag{A.50}$$

When we substrate EqA.50 into Eq. A.2, Eq. A.10,

$$\begin{pmatrix} E_{ix}(z) \\ H_{iy}(z) \end{pmatrix} = M_i' \begin{pmatrix} E_{ix}(0) \\ H_{iy}(0) \end{pmatrix} \tag{A.51}$$

where

$$M_i' = \begin{pmatrix} \frac{1}{2}e^{ik_{iz}z} + e^{-ik_{iz}z} & \frac{1}{2\Gamma}e^{ik_{iz}z} - e^{-ik_{iz}z} \\ -\frac{\Gamma}{2}e^{ik_{iz}z} - e^{-ik_{iz}z} & \frac{1}{2}e^{ik_{iz}z} + e^{-ik_{iz}z} \end{pmatrix} \tag{A.52}$$

When there is no absorption in the material, k_{iz} should be realistic number, then Eq. A.52 becomes

$$M_i' = \begin{pmatrix} \cos k_{iz}z & \frac{i}{\Gamma_i}\sin k_{iz}z \\ i\Gamma_i \sin k_{iz}z & \cos k_{iz}z \end{pmatrix} \tag{A.53}$$

The inverse matrix of M_i' is written as

$$M_i'^{-1} = M_i = \begin{pmatrix} \cos k_{iz}z & -\frac{i}{\Gamma_i}\sin k_{iz}z \\ -i\Gamma_i \sin k_{iz}z & \cos k_{iz}z \end{pmatrix} \tag{A.54}$$

then Eq. **??** becomes

$$\begin{pmatrix} E_{iy}(0) \\ H_{ix}(0) \end{pmatrix} = M_i \begin{pmatrix} E_{iy}(z) \\ H_{ix}(z) \end{pmatrix} \tag{A.55}$$

In the boundary at each layer, the component of Eq. A.55 is conserved. Thus, the electromagnetic wave which propagates the multi-layer coatings is described as

$$\begin{pmatrix} E_{iy}(0) \\ H_{ix}(0) \end{pmatrix} = M \begin{pmatrix} E_{sy}(L) \\ H_{sx}(L) \end{pmatrix} \tag{A.56}$$

$$M = M_1 M_2 M_3 \ldots M_N = \prod_{i=0}^{N} M_i \tag{A.57}$$

From these equations, we obtain the coefficient of reflectance r and transmittance t. The incident wave and the transmitted wave is written as

$$H_{0y}(z) = \left(e^{ik_{0z}z} + re^{-ik_{0z}z}\right) e^{k_{0z}x} \tag{A.58}$$

$$H_{sy}(z) = te^{ik_{0z}(z-L)}e^{ik_{0z}x} \tag{A.59}$$

By using Eq. A.45, we obtain

$$\Gamma_0 E_{0x}(z) = -\Gamma_0 \left(e^{ik_{0z}z} - re^{-ik_{0z}z}\right) e^{ik_{0z}x} \tag{A.60}$$

$$\Gamma_s E_{sx}(z) = \Gamma_s te^{ik_{0z}(z-L)}e^{ik_{0z}x} \tag{A.61}$$

and

$$H_{0y}(0) = (1+r)e^{ik_{0z}x} \tag{A.62}$$

$$\Gamma_0 E_{0x}(0) = -\Gamma_0(1-r)e^{ik_{0z}x} \tag{A.63}$$

$$H_{sy}(L) = te^{ik_{0z}x} \tag{A.64}$$

$$\Gamma_s E_{sx}(L) = -\Gamma_s te^{ik_{0z}x}. \tag{A.65}$$

Thus, Eq. A.57 becomes

$$\begin{pmatrix} \frac{1}{\Gamma_0} & \frac{1}{\Gamma_s}M_{11}+M_{12} \\ -1 & \frac{1}{\Gamma_s}M_{21}+M_{22} \end{pmatrix} \begin{pmatrix} r \\ t \end{pmatrix} = \begin{pmatrix} \frac{1}{\Gamma_0} \\ 1 \end{pmatrix}. \tag{A.66}$$

If we assume A as

$$A = \begin{pmatrix} \frac{1}{\Gamma_0}1 & \frac{1}{\Gamma_s}M_{11}+M_{12} \\ -1 & \frac{1}{\Gamma_s}M_{21}+M_{22} \end{pmatrix}, \tag{A.67}$$

we obtain

$$A^{-1} = \frac{1}{B}\begin{pmatrix} -(\frac{1}{\Gamma_s}M_{21}-M_{22}) & -\frac{1}{\Gamma_s}M_{11}-M_{12}) \\ 1 & \frac{1}{\Gamma_0} \end{pmatrix} \tag{A.68}$$

$$B = \frac{1}{\Gamma_0\Gamma_s}(\Gamma_0 M_{11} - \Gamma_0\Gamma_s M_{12} - M_{21} + \Gamma s M_{22}). \tag{A.69}$$

Thus, the coefficient of reflectance r and transmittance t is written as

$$r = \frac{-\Gamma_0 M_{11} - \Gamma_0\Gamma_s M_{12} + M_{21} + \Gamma s M_{22}}{\Gamma_0 M_{11} + \Gamma_0\Gamma_s M_{12} - M_{21} + \Gamma s M_{22}} \tag{A.70}$$

$$t = \frac{2\Gamma_s}{\Gamma_0 M_{11} + \Gamma_0\Gamma_s M_{12} + M_{21} + \Gamma s M_{22}}. \tag{A.71}$$

For the p-polarization, $E_y = 0$. Thus, The incident , reflected and transmitted poynting vector is

$$S_{0z} = \frac{n_0}{\cos\theta_0}\sqrt{\frac{\epsilon_0}{\mu_0}} \tag{A.72}$$

$$S_{rz} = -|r|^2\frac{n_0}{\cos\theta_0}\sqrt{\frac{\epsilon_0}{\mu_0}} \tag{A.73}$$

$$S_{tz} = |t|^2\frac{n_s}{\cos\theta_s}\sqrt{\frac{\epsilon_0}{\mu_0}}, \tag{A.74}$$

and reflectance and transmittance becomes

$$R = \frac{|S_{rz}|}{S_{0z}} = |r|^2 \tag{A.75}$$

$$T = \frac{S_{tz}}{S_{0z}} = |t|^2\frac{n_0\cos\theta_s}{n_s\cos\theta_0}. \tag{A.76}$$

Appendix B

Modulation efficiency from RCWA based simulation

In this section, we introduce how to obtain each value of the modulation efficiency from the outputs of the RCWA simulation. The outputs of RCWA simulation are Jones matrices $J^{(\nu)}$ for each frequency ν as

$$J^{(\nu)} = \begin{pmatrix} J_{11}^{(\nu)} & J_{12}^{(\nu)} \\ J_{21}^{(\nu)} & J_{22}^{(\nu)} \end{pmatrix}. \tag{B.1}$$

Here in after we omit the frequency (ν).

B.1 Calculation of transmittance

From Eq. B.1, two transmittance, T_x and T_y, are obtained. The definition of them is follwing:

- T_x: the transmittance when the polarization angle of the incident light is parallel to the optic axis of the first layer of the AHWP.
- T_y: the transmittance when the polarization angle of the incident light is perpendicular to the optic axis of the first layer of the AHWP.

Using the elements of Eq. B.1, T_x and T_y are expressed as

$$\begin{aligned} T_x &= |J_{11}|^2 + |J_{21}|^2 \\ T_y &= |J_{12}|^2 + |J_{22}|^2. \end{aligned} \tag{B.2}$$

B.2 Conversion Jones matrix to Mueller

We convert the jones matrix to mueller matrix by

$$M_{ij} = \frac{1}{2}\mathrm{Tr}(\sigma_i J \sigma_j J^{\dagger}), \tag{B.3}$$

where σ_i (i=1.2,3,4) is Pauli matrices which is written as

$$\sigma_1 = \begin{pmatrix} 1 & 0 \\ 0 & 1 \end{pmatrix}, \ \sigma_2 = \begin{pmatrix} 1 & 0 \\ 0 & -1 \end{pmatrix}, \ \sigma_3 = \begin{pmatrix} 0 & 1 \\ 1 & 0 \end{pmatrix}, \ \sigma_4 = \begin{pmatrix} 0 & -i \\ i & 0 \end{pmatrix}. \tag{B.4}$$

Specifically the form of each element is following:

$$\begin{aligned}
M_{11} &= \frac{1}{2}(J_{11}J_{11}^* + J_{21}J_{21}^* + J_{12}J_{12}^* + J_{22}J_{22}^*) \\
M_{12} &= \frac{-1}{2}(J_{22}J_{22}^* - J_{21}J_{21}^* + J_{12}J_{12}^* - J_{11}J_{11}^*) \\
M_{13} &= \frac{1}{2}(J_{21}J_{22}^* + J_{22}J_{21}^* + J_{11}J_{12}^* + J_{12}J_{11}^*) \\
M_{14} &= \frac{-i}{2}(J_{21}J_{22}^* - J_{22}J_{21}^* + J_{11}J_{12}^* - J_{11}J_{12}^*)
\end{aligned}$$

$$\begin{aligned}
M_{21} &= \frac{-1}{2}(J_{22}J_{22}^* + J_{21}J_{21}^* - J_{12}J_{12}^* - J_{22}J_{22}^*) \\
M_{22} &= \frac{1}{2}(J_{22}J_{22}^* - J_{21}J_{21}^* - J_{12}J_{12}^* + J_{11}J_{11}^*) \\
M_{23} &= \frac{-1}{2}(J_{12}J_{22}^* + J_{22}J_{12}^* - J_{11}J_{12}^* - J_{12}J_{11}^*) \\
M_{24} &= \frac{i}{2}(J_{21}J_{22}^* - J_{22}J_{21}^* - J_{11}J_{12}^* + J_{21}J_{11}^*)
\end{aligned}$$

$$\begin{aligned}
M_{31} &= \frac{1}{2}(J_{12}J_{22}^* + J_{22}J_{12}^* + J_{11}J_{21}^* + J_{21}J_{11}^*) \\
M_{32} &= \frac{-1}{2}(J_{12}J_{22}^* + J_{22}J_{12}^* - J_{11}J_{21}^* - J_{21}J_{11}^*) \\
M_{33} &= \frac{1}{2}(J_{11}J_{22}^* + J_{22}J_{11}^* + J_{12}J_{21}^* + J_{21}J_{12}^*) \\
M_{34} &= \frac{-i}{2}(J_{11}J_{22}^* - J_{22}J_{11}^* - J_{12}J_{21}^* + J_{21}J_{12}^*)
\end{aligned}$$

$$\begin{aligned}
M_{41} &= \frac{i}{2}(J_{12}J_{22}^* - J_{22}J_{12}^* + J_{11}J_{21}^* - J_{21}J_{11}^*) \\
M_{42} &= \frac{-i}{2}(J_{12}J_{22}^* - J_{22}J_{12}^* - J_{11}J_{21}^* + J_{21}J_{11}^*) \\
M_{43} &= \frac{i}{2}(J_{11}J_{22}^* - J_{22}J_{11}^* + J_{12}J_{21}^* - J_{21}J_{12}^*) \\
M_{44} &= \frac{1}{2}(J_{11}J_{22}^* + J_{22}J_{11}^* - J_{12}J_{21}^* - J_{21}J_{12}^*)
\end{aligned}$$

In the following, we express the elements of M using Stokes parameters as

$$M = \begin{pmatrix} M_{11} & M_{12} & M_{13} & M_{14} \\ M_{21} & M_{22} & M_{23} & M_{24} \\ M_{31} & M_{32} & M_{33} & M_{34} \\ M_{41} & M_{42} & M_{43} & M_{44} \end{pmatrix} = \begin{pmatrix} M_{\mathrm{II}} & M_{\mathrm{IQ}} & M_{\mathrm{IU}} & M_{\mathrm{IV}} \\ M_{\mathrm{QI}} & M_{\mathrm{QQ}} & M_{\mathrm{QU}} & M_{\mathrm{QV}} \\ M_{\mathrm{UI}} & M_{\mathrm{UQ}} & M_{\mathrm{UU}} & M_{\mathrm{UV}} \\ M_{\mathrm{VI}} & M_{\mathrm{VQ}} & M_{\mathrm{VU}} & M_{\mathrm{VV}} \end{pmatrix}. \tag{B.5}$$

B.3 Calculation of modulation efficiency

Using Eq. B.5, we calculate the Stokes vector, $S_{\mathrm{out}} = (I_{\mathrm{out}}, Q_{\mathrm{out}}, U_{\mathrm{out}}, V_{\mathrm{out}})$, after passing a continuous rotating AHWP as

$$S_{\mathrm{out}} = GR(-\omega_{\mathrm{hwp}}t)MR(\omega_{\mathrm{hwp}}t)S_{\mathrm{in}}, \tag{B.6}$$

where $S_{\rm in} = (I_{\rm in}, Q_{\rm in}, U_{\rm in}, V_{\rm in})$ is the initial Stokes vector, $\omega_{\rm hwp}t$ is the rotation angle of AHWP, R is rotation matrix, G is Mueller matrix of a polarizer along x-axis which is corresponding to the single polarization sensitive detector. The detail of G and R is written as

$$R(\rho) = \begin{pmatrix} 1 & 0 & 0 & 0 \\ 0 & \cos 2\rho & -\sin 2\rho & 0 \\ 0 & \sin 2\rho & \cos 2\rho & 0 \\ 0 & 0 & 0 & 1 \end{pmatrix}, \quad G = \frac{1}{2}\begin{pmatrix} 1 & 1 & 0 & 0 \\ 1 & 1 & 0 & 0 \\ 0 & 0 & 0 & 0 \\ 0 & 0 & 0 & 0 \end{pmatrix} \tag{B.7}$$

where ρ is the rotation angle. From Eq. B.6, we obtain

$$\begin{aligned} I_{\rm out}(t) =& D_{0\rm I} I_{\rm in} + D_{0\rm Q} Q_{\rm in} + D_{0\rm U} U_{\rm in} \\ &+ D_{2\rm I} I_{\rm in} \cos(2\omega_{\rm hwp}t - 2\phi_0) + D_2\sqrt{Q_{\rm in}^2 + U_{\rm in}^2}\cos(2\omega_{\rm hwp}t - 2\phi_2 - \arctan\frac{U_{\rm in}}{Q_{\rm in}}) \\ &+ D_4\sqrt{Q_{\rm in}^2 + U_{\rm in}^2}\cos(4\omega_{\rm hwp}t - 4\phi_4 - \arctan\frac{U_{\rm in}}{Q_{\rm in}}). \end{aligned} \tag{B.8}$$

Eq. B.8 shows $I_{\rm out}$ which is written using coefficients D and ϕ as a function of time t. The mode of $4\omega_{\rm hwp}t$ is the modulation signal. Each coefficient is written using the elements of M as

$$\begin{aligned} D_{0\rm I} &= \frac{1}{2} M_{\rm II} \\ D_{0\rm Q} &= \frac{1}{4}(M_{\rm QQ} + M_{\rm UU}) \\ D_{0\rm U} &= \frac{1}{4}(M_{\rm QU} - M_{\rm UQ}) \\ D_{2\rm I} &= \frac{1}{2}\sqrt{M_{\rm UI}^2 + M_{\rm QI}^2} \\ \phi_0 &= \frac{1}{2}\arctan\frac{M_{\rm UI}}{M_{\rm QI}} \\ D_2 &= \frac{1}{2}\sqrt{M_{\rm IQ}^2 + M_{\rm IU}^2} \\ \phi_2 &= \frac{1}{2}\arctan\frac{M_{\rm IU}}{M_{\rm IQ}} \\ D_4 &= \frac{1}{4}\sqrt{(M_{\rm QQ} - M_{\rm UU})^2 + (M_{\rm QU} + M_{\rm UQ})^2} \\ \phi_4 &= \frac{1}{4}\arctan\frac{M_{\rm QU} + M_{\rm UQ}}{M_{\rm QQ} - M_{\rm UU}}. \end{aligned}$$

We define the modulation efficiency ϵ as

$$\epsilon = 2D_4. \tag{B.9}$$

Here, the ignoring of the effect of the reflection is reasonable so we can replace M' by M. Where, χ_i is the optic axis angle for each plate, $\delta = 2\pi\nu d|n_e - n_o|/c$ is retardance between the optic axes, n_o and n_e is refractive indices for the ordinary and extraordinary rays, d is the thickness of each plate that constitute AHWP.

$$M' = \prod_{n=1}^{N} R(-\chi_i)\Gamma R(\chi_i) \tag{B.10}$$

$$\Gamma = \begin{pmatrix} 1 & 0 & 0 & 0 \\ 0 & 1 & 0 & 0 \\ 0 & 0 & \cos\delta & -\sin\delta \\ 0 & 0 & \sin\delta & \cos\delta \end{pmatrix}.$$

B.4 Calculation of band averaged modulation efficiency

To obtain the band averaged modulation efficiency, we integrate the modulated part of I_{out} with the weight function w as

$$\begin{aligned} Sum^{(4f)} =& \sqrt{Q_{\text{in}}^2 + U_{\text{in}}^2} \sum_{n=1}^{N} w_n D_4^{(n)} \cos(4\omega_{\text{hwp}}t - 4\phi_4^{(n)} - \arctan\frac{U_{\text{in}}}{Q_{\text{in}}}) \\ =& \sqrt{Q_{\text{in}}^2 + U_{\text{in}}^2} [\{w_1 D_4^{(1)} \cos(4\phi_4^{(1)}) + w_2 D_4^{(2)} \cos(4\phi_4^{(2)})\} \cos(4\omega_{\text{hwp}}t - \arctan\frac{U_{\text{in}}}{Q_{\text{in}}}) \\ &+ \{w_1 D_4^{(1)} \sin(4\phi_4^{(1)}) + w_2 D_4^{(2)} \sin(4\phi_4^{(2)})\} \sin(4\omega_{\text{hwp}}t - \arctan\frac{U_{\text{in}}}{Q_{\text{in}}}) \\ &+ ... + w_N D_4^{(N)} \cos(4\omega_{\text{hwp}}t - 4\phi_4^{(N)} - \arctan\frac{U_{\text{in}}}{Q_{\text{in}}})] \\ =& D_4^{(1,2)} \cos(4\omega_{\text{hwp}}t - 4\phi_4^{(1,2)} - \arctan\frac{U_{\text{in}}}{Q_{\text{in}}}) + ... + w_N D_4^{(N)} \cos(4\omega_{\text{hwp}}t - 4\phi_4^{(N)} - \arctan\frac{U_{\text{in}}}{Q_{\text{in}}})] \\ =& \sqrt{Q_{\text{in}}^2 + U_{\text{in}}^2} D_4^{(1,2,...,n)} \cos(4\omega_{\text{hwp}}t - 4\phi_4^{(1,2,...,n)} - \arctan\frac{U_{\text{in}}}{Q_{\text{in}}})]. \end{aligned} \tag{B.11}$$

In this thesis, the weight function is unity. And define the band averaged modulation efficiency ϵ_{band} as

$$\epsilon_{band} = \frac{2D_4^{(1,2,.....,N)}}{N}. \tag{B.12}$$

B.5 Relationship with sensitivity calculation

We can only pick up the DC term and the $4\omega_{\text{hwp}}t$ term of Eq. B.8 and write for simplicity as

$$I_{out}(t) = D_{01} I_{in} + D_4 I_p \cos\Phi_4, \tag{B.13}$$

where

$$I_p = \sqrt{Q_{in}^2 + U_{in}^2} \tag{B.14}$$

$$\Phi_4 = 4\omega_{hwp}t - 4\phi_4 - \arctan\frac{Q_{in}}{U_{in}}. \tag{B.15}$$

We can rearrange Eq B.18 further

$$I_{out}(t) = \frac{1}{2} I_{in} \left[M_{11} + 2D_4 P \cos \Phi_4\right] \tag{B.16}$$

$$= \frac{1}{2} I_{in} \left[M_{11} + \epsilon P \cos \Phi_4\right] \tag{B.17}$$

$$= \frac{1}{2} I_{in} M_{11} \left[1 + \frac{\epsilon}{M_{11}} P \cos \Phi_4\right]. \tag{B.18}$$